



## An X-ray Spectral Survey of Radio-Loud AGN With ASCA

Rita M. Sambruna<sup>1</sup>, Michael Eracleous<sup>1</sup>, & Richard F. Mushotzky<sup>2</sup>

To appear in the *Astrophysical Journal*

### ABSTRACT

We present a uniform and systematic analysis of the 0.6–10 keV X-ray spectra of radio-loud active galactic nuclei (AGN) observed by *ASCA*. The sample, which is not statistically complete, includes 10 Broad Line Radio Galaxies (BLRGs), 5 radio-loud Quasars (QSRs), 9 Narrow Line Radio Galaxies (NLRGs), and 10 Radio Galaxies (RGs) of mixed FR I and FR II types. For several sources the *ASCA* data are presented here for the first time. The exposure times of the observations and the fluxes of the objects vary over a wide range; as a result, so does the signal-to-noise ratio of the individual X-ray spectra. At soft X-rays, about 50% of NLRGs and 100% of RGs exhibit a thermal plasma emission component, with a bimodal distribution of temperatures and luminosities. This indicates that the emission arises in hot gas either in a surrounding cluster or loose group or in a hot corona, consistent with previous *ROSAT* and optical results. At energies above 2 keV, a hard power-law component (photon index,  $\Gamma \sim 1.7 - 1.8$ ) is detected in 90% of cases. The power-law photon indices and luminosities in BLRGs, QSRs, and NLRGs are similar. This is consistent with simple orientation-based unification schemes for lobe-dominated radio-loud sources in which BLRGs, QSRs, and NLRGs harbor the same type of central engine. Moreover, excess cold absorption in the range  $10^{21} - 10^{24} \text{ cm}^{-2}$  is detected in most (but not all) NLRGs, consistent with absorption by an obscuring torus, as postulated by unification scenarios. The *ASCA* data provide initial evidence that the immediate gaseous environment of the X-ray source of BLRGs may be different than in Seyfert 1s: absorption edges of ionized oxygen, common in the latter, are detected in only one BLRG. Instead we detect large columns of *cold* gas in

---

<sup>1</sup>Department of Astronomy and Astrophysics, The Pennsylvania State University, 525 Davey Lab, State College, PA 16802, e-mail: rms@astro.psu.edu, mce@astro.psu.edu.

<sup>2</sup>NASA/GSFC, Code 662, Greenbelt, MD 20771, e-mail: mushotzky@1heavx.gsfc.nasa.gov.

a fraction ( $\sim 44\text{--}60\%$ ) of BLRGs and QSRs, comparable to the columns detected in NLRGs, which is puzzling. This difference hints at different physical and/or geometrical properties of the medium around the X-ray source in radio-loud AGN compared to their radio-quiet counterparts, that can be explored further with future X-ray observations. For the full sample, the nuclear X-ray luminosity is correlated with the luminosity of the [O III] emission line, the FIR emission at  $12\ \mu\text{m}$ , and the lobe radio power at 5 GHz. The Fe K $\alpha$  line is detected in 50% of BLRGs and in one QSR, with a large range of intrinsic widths and equivalent widths. In the handful of NLRGs where it is detected, the line is generally unresolved. Comparing the average power-law photon indices of the various classes of radio-loud AGN to their radio-quiet counterparts from the literature, we find only a weak indication that the *ASCA* 2–10 keV spectra of BLRGs are flatter than those of Seyfert 1s of comparable X-ray luminosity. This result is at odds with evidence from samples studied by other authors suggesting that radio-loud AGN have flatter spectra than radio-quiet ones. Rather, it supports the idea that a beamed synchrotron self-Compton component related to the radio source (jet) is responsible for the flatter slopes in those radio-loud AGN. We argue that because of the way those samples were constructed, beamed X-ray emission from the radio jets probably contributed to the observed X-ray spectra.

The sample studied here includes 6 Weak Line Radio Galaxies (WLRGs), powerful radio galaxies characterized by [O III]  $\lambda\lambda 4569, 5007$  lines of unusually low luminosity and by unusually high [O II]/[O III] line ratios. The *ASCA* spectra of WLRGs can be generally decomposed into a soft thermal component with  $kT \sim 1$  keV, plus a hard component, described either by a flat ( $\langle\Gamma\rangle = 1.5$ ) absorbed power law, or a very hot ( $kT \sim 100$  keV) thermal bremsstrahlung model. Their intrinsic luminosities are in the range  $L_{2-10\ \text{keV}} \sim 10^{40}\text{--}10^{42}$  erg s $^{-1}$ , two orders of magnitude lower than in other sources in our sample. If the hard X-ray emission is attributed to a low-luminosity AGN, an interesting possibility is that WLRGs represent an extreme population of radio galaxies in which the central black hole is accreting at a rate well below the Eddington rate.

*Subject Headings:* Galaxies:active – X-rays:galaxies – Radiation mechanisms:non-thermal – Radio galaxies:individual.

## 1. Introduction

The X-ray spectra of Active Galactic Nuclei (AGN) are a diagnostic of the structure of their accretion flows. Recent studies of X-ray-bright Seyfert galaxies with *ROSAT*, *GINGA*, and *ASCA* have shown their 0.1–100 keV spectra to be complex. The intrinsic X-ray continuum is typically described by a power law model with a mean photon index of  $\langle\Gamma\rangle \approx 1.9$ , albeit with an appreciable dispersion around this value. A soft excess is sometimes detected below 1 keV and modelled as

thermal emission from an accretion disk. At higher energies, an Fe  $K\alpha$  emission line is detected between rest-frame energies of 6 and 7 keV in several sources (Nandra & Pounds 1994; Mushotzky et al. 1995; Nandra et al. 1997a). The line is strong ( $EW \sim 250$  eV) and broad, with a tail extending to the red (Tanaka et al. 1995; Nandra et al. 1997a). The line profile is consistent with gravitational and Doppler broadening in a black hole accretion disk (Fabian et al. 1989), although other explanations could be possible (e.g., Weaver & Yaqoob 1998). At higher energies, *GINGA* observations have shown that many Seyferts exhibit a Compton reflection bump peaking around 20–30 keV (Nandra & Pounds 1994), now confirmed by *RXTE* observations (Lee et al. 1998; Weaver, Krolik, & Pier 1998). This spectral feature has been interpreted as the result of reprocessing of the primary continuum by cold matter around the X-ray source, presumably the accretion disk (Lightman & White 1988; Guilbert & Rees 1988; George & Fabian 1991). The X-rays also probe the immediate environment around the X-ray source of an AGN. At low energies, absorption features from ionized gas are detected with *ASCA* in about 50% of Seyfert 1s (Reynolds 1997; George et al. 1998). The inferred column densities of this “warm absorber” are in the range  $N_W \sim 10^{21}–10^{24}$  cm $^{-2}$ .

In contrast to Seyferts and other radio-quiet AGN, the hard X-ray spectra of radio-loud AGN are not known in much detail. Pre-*ASCA* studies of heterogeneous samples of radio-loud AGN with *EXOSAT*, *Einstein*, and *GINGA* have shown that these objects are systematically more X-ray luminous than their radio-quiet counterparts of similar optical luminosity. In addition, they have flatter continua than Seyferts with photon indices differing by  $\Delta\Gamma \sim 0.5$  (Wilkes & Elvis 1987; Lawson et al. 1992; Shastri et al. 1993; Lawson & Turner 1997). However, these studies were plagued by the low sensitivity of the instruments, especially at low energies where the diffuse thermal emission from the host galaxy or cluster can make a substantial contribution (Worrall et al. 1994). Observations with high spectral resolution and sensitivity over a wide energy band are the key to disentangling the various spectral features and measuring the intrinsic X-ray properties of radio-loud AGN more reliably.

The high spectral resolution of the *ASCA* SIS at both low and high X-ray energies, combined with its broad-band (0.6–10 keV) sensitivity, are well suited to studying the X-ray properties of radio-loud AGN. Indeed, results for a few individual bright sources, mainly broad-line radio galaxies, show that some of these objects have complex spectra, with a broad Fe line and intrinsic power-law photon indices of  $\Gamma \sim 1.7 – 2.0$  (Eracleous, Halpern, & Livio 1996; Grandi et al. 1997; Sambruna et al. 1998), although others do not (Eracleous & Halpern 1998; Reynolds et al. 1998). The hard spectral response of *ASCA* is essential for separating spectrally the soft thermal component from the hard nuclear power law component and better studying the latter.

In order to characterize the X-ray properties of radio-loud AGNs we have carried out a systematic analysis of archival *ASCA* data for a sample of such objects. For several of these objects for which the data analysis is presented here for the first time. Other goals of this work include testing unified schemes and exploring the origin of the radio-loud/radio-quiet AGN dichotomy. The sample is made up of various classes of radio-loud AGN, which can mainly be

divided into “type 1” objects (those with both broad and narrow optical emission lines) and “type 2” (those with only narrow optical lines). According to the simple orientation-based unification schemes, type 1 and type 2 sources contain similar active nuclei seen at different angles with respect to the axis of a thick, obscuring torus (e.g., Urry & Padovani 1995). The X-ray properties provide a test of these ideas: because of the high penetrating power of the hard X-rays, it is possible to measure the intrinsic luminosity and spectral shape of the central engine in type 2 objects up to line-of-sight column densities of  $\approx 10^{24} \text{ cm}^{-2}$ . In principle, a test of the models should also be provided by the Fe line, which is expected to have higher Equivalent Widths (EWs) in type 2 AGN.

Another use of the X-ray observations is to constrain ideas for the origin of the radio-loud/radio-quiet AGN dichotomy. Indeed, different X-ray properties between the two classes are predicted in the context of models which attribute the dichotomy to a different structure of the accretion disk or to the intrinsic properties of the black hole. We thus compare the average X-ray spectral properties of our sample of radio-loud AGN with those of samples of radio-quiet AGN available in the literature. Such a comparison, carried out by Woźniak et al. (1998) using *ASCA* as well as other, non-simultaneous data, has already yielded interesting results. These authors found that Broad Line Radio Galaxies, the alleged radio-loud counterparts of Seyfert 1s, have systematically flatter slopes, narrower and weaker Fe  $K\alpha$  lines, and weak or absent Compton reflection components at  $\gtrsim 10 \text{ keV}$ .

In addition, we use the spectroscopic capabilities of *ASCA* to characterize the medium surrounding radio galaxies. Recent results *ROSAT* observations (e.g., Worrall & Birkinshaw 1994; Crawford et al. 1999) established that most radio sources are embedded in diffuse, hot haloes with core radii up to several hundreds of kpc. The *ASCA* sensitivity allows us to detect the thermal component and measure with accuracy its spectral parameters, complementing *ROSAT*.

The paper is organized as follows. The sample selection criteria and definitions are given in §2, together with a description of the *ASCA* observations. Data analysis and results of the spectral fits are reported in §3 and §4, respectively. In §5 we present the average nuclear properties of the various subclasses, while in §6 we examine correlations of the nuclear X-ray luminosity with the luminosity at other wavelengths. The summary and discussion of the results are given in §7 and §8, with the conclusions following in §9. The Appendix provides a full discussion of the results for the individual sources, with particular emphasis on the sources for which the *ASCA* data are presented here for the first time. Throughout this paper we assume a Hubble constant of  $H_0 = 75 \text{ km s}^{-1} \text{ Mpc}^{-1}$  and a deceleration parameter of  $q_0 = 0.5$ .

## 2. The Sample and the Data

Our sample includes all the radio-loud AGN observed by *ASCA* for which data were available in the public archive up to 1998 September. We adopted the quantitative criteria for radio-loudness

of Kellermann et al. (1989, 1994), namely objects with either a 5 GHz radio power of  $P_{5\text{GHz}} > 10^{25} \text{ W Hz}^{-1}$  or with rest-frame 5 GHz-to-4400 Å flux-density ratios of  $\mathcal{R}_{\text{ro}} > 10$ . In addition, we included an analysis of the *ASCA* data of the high-redshift radio galaxy 4C +41.17 and the low-power radio galaxy IC 310, whose X-ray observations have never been published. The former object is a star-forming radio galaxy at  $z = 3.798$  (see Dey et al. 1997 and references therein); its *ASCA* data are affected by abnormally large positional uncertainties (see Appendix). IC 310 is a “head-tail” radio source, which does not satisfy either of the strict criteria listed above ( $P_{5\text{GHz}} = 1.5 \times 10^{23} \text{ W Hz}^{-1}$ ,  $\mathcal{R}_{\text{ro}} > 4$ ), although it is traditionally regarded as a radio galaxy (Simon 1979; Miley 1980; Owen, Ledlow, & Keel 1996). Neither of these objects is included in the statistical tests that we carry out in later sections of the paper; their properties are discussed in the Appendix. Blazars and high-redshift ( $z > 1$ ) radio-loud quasars were excluded from the sample since their observed X-ray emission is affected by beaming. For a review of their *ASCA* data, see Cappi et al. (1997), Reeves et al. (1997), Kubo et al. (1998), Vignali et al. (1999). Our selection criteria gave a total of 39 objects (including IC 310 and 4C +41.17), which are listed in Table 1.

The objects in the final sample were divided into four subclasses according to their optical spectroscopic properties, such as the presence of broad, permitted lines in their optical spectra and the luminosity of the [O III]  $\lambda 5007$  line. Objects with broad, permitted optical emission lines (typically Balmer and/or Mg II  $\lambda 2800$  lines) were classified either as Quasars or Broad Line Radio Galaxies (hereafter QSRs and BLRGs, respectively). Objects without broad emission lines were classified as Narrow Line Radio Galaxies or Radio Galaxies (hereafter NLRGs and RGs, respectively). The distinction between QSRs and BLRGs was based on the [O III] luminosity, by adopting  $L_{[\text{O III}]} > 10^{43.5} \text{ erg s}^{-1}$  as the condition for classifying an object as a QSR. Similarly NLRGs were separated from RGs by requiring that the former subclass have  $L_{[\text{O III}]} > 10^{41} \text{ erg s}^{-1}$ . The [O III] luminosity criteria we have adopted are admittedly arbitrary. However, they ensure that objects traditionally regarded as QSRs fall in the appropriate category, and similarly for RGs. The giant double-lobed radio source 4C +74.26 was tentatively classified as a QSR based on its optical luminosity and the equivalent width of its [O III] line (Brinkmann et al. 1998). This turned out to be a reasonable classification *a posteriori* when we found the X-ray luminosity of this object to be comparable to that of QSRs. Similarly, PKS 2251+11 (also known as PG 2251+11) was classified as a BLRG based on its [O III] luminosity, a classification which is consistent with its X-ray properties as described in later sections. This classification scheme gives 10 BLRGs, 12 NLRGs, 6 QSRs, and 11 RGs. The sample is by no means statistically complete or unbiased; indeed, since the targets were originally selected as part of independent programs by different observers, they may reflect a bias toward the brightest sources of each type.

All the BLRGs, NLRGs, and QSRs of Table 1 turn out to be powerful radio sources that satisfy both of the above criteria for radio loudness. This is not the case for the RGs, however. Although all of the RGs have  $\mathcal{R}_{\text{ro}} > 10$ , only three of them have  $P_{5\text{GHz}} > 10^{25} \text{ W Hz}^{-1}$ : 3C 28, PKS 0625–53, and 3C 353. Most of the other objects are intermediate-power FR I radio galaxies (Fanaroff & Riley 1974) with  $10^{25} \text{ W Hz}^{-1} > P_{5\text{GHz}} > 10^{22} \text{ W Hz}^{-1}$ . Included among the RGs are 6 Weak-Line

Radio Galaxies (WLRGs; identified as such in Tables 1–4), of either FR I or FR II morphology. These were recently identified in sensitive spectroscopic surveys in optical as moderately-powerful radio galaxies with low ionization state of their narrow-line gas, which manifests itself as a high value of the [O II]/[O III] emission-line ratio, in the range of 1–10 (Tadhunter et al. 1998). WLRGs have [O III] luminosities an order of magnitude or more lower than those of other radio galaxies of similar radio power (Tadhunter et al. 1998; Laing et al. 1994). These sources are thus characterized by small ratios of the [O III] to radio power.

In Table 1 we list the basic properties of each object: redshift (column 2), coordinates (column 3), other common names (column 4), Galactic column density from H I 21 cm maps (column 5), ratio of the core radio power to the lobe radio power  $R$  (column 6), and luminosities at other wavelengths (columns 7–10) with relevant references (column 11). The Galactic column densities were taken from Elvis, Lockman, & Wilkes (1989), Murphy et al. (1996), and Stark et al. (1992), and have a formal 90% uncertainty of  $\pm 1 \times 10^{20} \text{ cm}^{-2}$  or better. The luminosities given are the rest-frame monochromatic luminosities ( $\nu L_\nu$ ) at 5 GHz and in the IRAS 12  $\mu\text{m}$  and 60  $\mu\text{m}$  bands, and the integrated [O III]  $\lambda 5007$  emission-line luminosity. The [O III] luminosity was corrected for foreground absorption in the Galaxy<sup>3</sup> and in the case of Centaurus A we also adopted the correction for extinction in the host galaxy (Storchi-Bergmann et al. 1997). The monochromatic luminosities were transformed to the rest frame of the source using the measured spectral index (the 5-to-2.7 GHz or 5-to-1.4 GHz spectral index for the radio band, the 12-to-25  $\mu\text{m}$  spectral index for the 12  $\mu\text{m}$  band and the 25-to-60  $\mu\text{m}$  spectral index for the 60  $\mu\text{m}$  band).

Table 2 summarizes the *ASCA* observations, with the observation date (column 2), the image designation number in the *ASCA* archive (column 3), the effective exposure time after data screening (column 4), and the net source count rate recorded by the SIS0 (0.6–10 keV) and GIS2 (0.7–10 keV) detectors, or the corresponding  $3\sigma$  upper limit (columns 5 and 6). As Table 2 shows, 100% of the BLRGs, 75% of the NLRGs, 83% of the QSRs, and 100% of the RGs were detected. The signal-to-noise ratio in the SIS spans a broad range of 3–300. A few sources, including 3C 303, 3C 390.3, 3C 219, and Cygnus A, were observed repeatedly by *ASCA*. Observations of the same target at different epochs are indicated with sequential numbers in Table 2 and in all tables thereafter. In the case of 3C 303, which was observed at two epochs about 8 months apart, no flux variations were found between the two datasets, which were thus coadded for spectral analysis. The data for several of these sources were published by other authors, as described in the Appendix. To ensure uniformity in the spectral analysis we re-analyzed the data according to our own data screening criteria.

---

<sup>3</sup>The correction was computed according to the Seaton (1979) law, using the Galactic H I column density listed in Table 1 and  $N_{\text{H}}/E(B - V) = 5 \times 10^{21} \text{ cm}^{-2} \text{ mag}^{-1}$  (Savage & Mathis 1979).

### 3. Data Screening and Analysis

The sources listed in Table 1 were observed by *ASCA* (Tanaka, Inoue, & Holt 1994) in a variety of SIS modes, including **FAINT**, **BRIGHT**, and **BRIGHT2**. In order to apply standard data analysis methods, the **FAINT** mode was converted into **BRIGHT2**, applying the corrections for echo effect and dark frame error which takes into account a more precise calibration at the lower energies. If the SIS data were taken in mixed **FAINT** and **BRIGHT** mode, they were converted to **BRIGHT** mode in order to have a better signal-to-noise ratio, except for the brighter cases, where the **BRIGHT2** mode was used instead for a more detailed spectral analysis. The GIS data were all taken in PH mode. The SIS data were taken in 1CCD mode, except for Cyg A and IC 310 (4CCD), Fornax A, Centaurus A, and 4C +41.17 (2CCD).

In order to perform a systematic analysis it is important that the extraction criteria are as uniform as possible, so that the systematic uncertainties are uniform as well. The screening criteria for both SIS and GIS included the rejection of data taken during passages over the South Atlantic Anomaly and with geomagnetic cutoff rigidity lower than 6 GeV/c. We retained data accumulated for Bright Earth angles greater than  $20^\circ$  and Elevation Angles greater than  $10^\circ$  for the SIS and  $5^\circ$  for the GIS. Only data corresponding to SIS grades 0, 2, 3, and 4 were retained in the spectral analysis (in general, inclusion of grade 6 did not improve the quality of the data at the higher energies). We checked each data set individually to ensure that the above data selection criteria gave the best signal-to-noise ratio. These criteria are similar to those used by most authors when analyzing *ASCA* observations of Seyfert galaxies and radio-quiet quasars. As a result we can readily compare our results with theirs.

Source spectra and light curves were extracted from circular regions centered on the source position with a radius of  $4'$  in the case of the SIS and  $6'$  in the case of the GIS, which has a larger intrinsic point spread function. In the case of the GIS we evaluated the background in circular regions of radius  $4'$ , each located about  $12'$  away from the target where the source counts are negligible, and avoiding other sources in the field. In a few radio galaxies the *ASCA* data are dominated by the diffuse emission on a cluster scale (Table 3); in these cases we used a larger extraction cell ( $\sim 8'$  at  $z = 0.05$ ) in order to collect most of the flux. In the case of the SIS, the background was measured in a circular region of radius  $2'$  located  $6'$  away from the target on the same chip, or from blank-sky observations, when needed. For the fainter sources in Table 2, we checked that our results did not depend on the background by measuring the latter at different locations on the detector field of view, when possible. The light curves were visually inspected to search for intervals of data dropout, which were eliminated from the final analysis, and for source variability (see §3.1). Since, in general, no temporal variations were detected (see §3.1), in all cases spectra were produced by accumulating photons over the entire duration of the observation. We extracted SIS and GIS spectra only when 100 or more counts were detected (Table 2), a condition met by 34 sources (10 BLRGs, 9 NLRGs, 5 QSRs, and 10 RGs).

The *ASCA* spectra were fitted using the *XSPEC* (v.10) software package. The spectra were

rebinned so that each bin included at least 20 counts in order for the  $\chi^2$  test to be safely valid. Joint fits to the data from the 4 detectors were performed in each case, leaving the normalizations as independent parameters to account for uncalibrated differences between the effective areas. The GIS response matrices from the latest release of 1995 March were used for the GIS spectra, while for the SIS spectra we used the response matrices generated by the `sisrmg` program (v.1.1, 1997 April), including the latest calibration files. The `ascaarf` program (v.2.72, 1997 Mar 14) was used to generate the ancillary response functions (a convolution of the telescope effective area curve, the source point-spread function, and the detector transmission function). The SIS and GIS spectra were fitted in the energy ranges 0.6–10 keV and 0.7–10 keV, respectively, where the spectral response for each instrument is best known.

### 3.1. Timing Analysis

The SIS and GIS light curves were visually inspected for time variability on timescales up to the length of the observation. In practice, this analysis was limited to type 1 AGN (BLRGs and QSRs), whose light curves have the highest signal-to-noise ratio (Table 2). In the case of NLRGs and RGs, an additional complication is the difficulty in separating the nuclear emission from the thermal emission of the host galaxy or cluster.

No significant short-term flux variability was present in the data, with the exception of 3C 120, where flux changes with amplitude  $\sim 20\%$  are present toward the end of the *ASCA* observation (Grandi et al. 1997), as confirmed by a  $\chi^2$  test. In the remaining BLRGs and QSRs there is no evidence for significant flux variability on the short timescales of the *ASCA* observations ( $< 10$  hours). For 3C 382, there is an indication of variability ( $P_{\chi^2} \sim 0.002$ ) when the SIS light curves are finely binned (bin size 128 s), which is not confirmed, however, when the same light curves are binned more coarsely. The lack of flux variability of BLRGs on shorter timescales is in contrast to the large-amplitude variations observed in Seyfert 1s with *ASCA* on timescales as short as a few hours (Nandra et al. 1997b).

## 4. Model Fits to the X-Ray Spectra

### 4.1. Methodology

The goal of our spectral analysis is to find models that provide a good description of the 0.6–10 keV spectra of all the sources in our sample. This includes models for a possible Fe line around 6–7 keV, which is present in most Seyferts (Nandra et al. 1997a; Turner et al. 1997a) and in several BLRGs (Eracleous et al. 1995; Grandi et al. 1997; Sambruna et al. 1998). The properties of the line profile are important diagnostics of the physical conditions at the heart of the emission region. In practice, however, because of the limited *ASCA* pass-band and possible continuum spectral



complexity, the line profile depends sensitively on the determination of the underlying continuum shape. Conversely, the determination of the continuum shape can be affected by the presence of an Fe line. We thus adopted the following fitting procedure. To search for the spectral model which best fits the continuum, we first examined the data from the four detectors jointly in the energy range 0.6–10 keV excluding the rest-frame energies 5–7 keV, a procedure which is now common (e.g., Nandra et al. 1997a). Once the best-fit continuum model was found, we included the 5–7 keV energy range, added a Gaussian emission line to the model, and fitted it to the data to determine the parameters of both the continuum and the line. We attempted fits with several continuum models, as described below. To decide whether the addition of one or more free parameters improves the fit significantly (and thus discriminate among continuum models), the F-test was used, adopting as a minimum threshold for improvement a probability of  $P_F \gtrsim 95\%$ . To assess the significance of the detection of an Fe line we conservatively assumed that it contributed three free parameters to the model even when the line energy and/or the width were kept fixed in the fit (since an *a priori* choice was made for this parameter).

The best-fitting models and their parameters are reported in Tables 3 and 4. Table 3 gives the continuum parameters and Table 4 gives the Fe line parameters; they both refer to the same best-fitting models. All the quoted uncertainties correspond to the 90% ( $1.6\sigma$ ) confidence level for one parameter of interest ( $\chi^2 = \chi_{\min}^2 + 2.7$ ). Figure 1 shows the best-fitting *continuum* models (upper panels) and the corresponding post-fit residuals (lower panels), expressed as the ratio of the model to the data. In the cases where an Fe line was required to fit the spectrum, the line profile model was excluded from the model plotted in Figure 1 to make the line appear in the ratio spectrum. A variety of models are needed to explain the *ASCA* continua of radio galaxies. It is apparent from Figure 1 that the Fe line is present in several sources.

#### 4.2. Suite of Models for the X-Ray Continuum and Synopsis of Results

Here we describe the spectral models which were fitted to the *ASCA* continua according to the procedure outlined above. In all cases, a column density fixed to the Galactic value was included, affecting all spectral components. The photoelectric absorption cross sections were taken from Morrison & McCammon (1983). In all models, the normalization factor(s) of the model were treated as free parameters. The continuum fit results are reported in Table 3 where we list the best-fit model and corresponding parameters (column 2), the reduced  $\chi_r^2$  and degrees of freedom (column 3), the observed X-ray flux integrated in 0.5–2 keV for the spectral component at low energies (column 4) and in 2–10 keV (column 5) for the component at high energies. The corresponding intrinsic (absorption-corrected and in the source rest-frame) luminosities are listed in columns 6 and 7, respectively.

1) *Absorbed Power Law*. Parameters: photon index  $\Gamma$  and column density  $N_H$  ( $\text{cm}^{-2}$ ). The latter was first fixed to the Galactic value from Table 1, and then left free to vary to search for possible excess absorption.

2) *Power Law + Absorption Edge.* Power law parameters: photon index  $\Gamma$ , column density  $N_{\text{H}}$  ( $\text{cm}^{-2}$ ). Edge parameters: energy  $E_e$  (keV), optical depth  $\tau_e$ . An absorption edge is detected only in 1/34 of the sources, namely in the longest of the three observations of 3C 390.3. For the remaining BLRGs and QSRs, we report the 90% upper limits to the optical depth of the O VII (0.739 keV) K-edge in the Appendix in all cases where the latter is redshifted within the SIS sensitivity range.

3) *Raymond-Smith Thermal Plasma.* Thermal emission from a hot, diffuse gas, including emission lines of several elements. Parameters: temperature  $kT$  (keV), elemental abundance  $Y$ . This model is an adequate representation of the X-ray spectra of 3/34 of the sources, yielding temperatures and metallicities typical of clusters of galaxies.

4) *Absorbed Power Law + Raymond-Smith Plasma.* Power law parameters: photon index  $\Gamma$ , column density  $N_{\text{H}}$  ( $\text{cm}^{-2}$ ). Raymond-Smith component parameters: temperature  $kT$  (keV), elemental abundance  $Y$ . This model is an adequate representation of the data for 14/34 of the sources. For the RG 3C 28, the detection of the power-law component is ambiguous (see Appendix) and this source was not included in the statistical tests.

5) *Partial Covering/Scattering.* The partial covering model parametrizes the physical situation of a “patchy” absorber, where the nuclear emission leaks through an absorbing medium covering only a fraction of the source (e.g., Holt et al. 1980). It can also describe the case of radiation scattered into the line of sight by a uniformly covering medium. Parameters: photon index  $\Gamma$ , column density  $N_{\text{H}}$  ( $\text{cm}^{-2}$ ), covering fraction  $f_c$  (the fraction of the source which is covered by the medium, or the fraction of the primary continuum flux scattered into the line of sight). This model provides a good fit to the data of 3/34 of the sources.

6) *Dual Absorber.* This model represents the physical situation of a nuclear power-law continuum which is seen through two different layers of gas, one uniformly covering the source and one partially covering the source. Parameters: photon index  $\Gamma$ , uniform column density  $N_{\text{H},1}$  ( $\text{cm}^{-2}$ ), partially covering column density  $N_{\text{H},2}$  ( $\text{cm}^{-2}$ ) and corresponding covering fraction  $f_{c,2}$ . The spectrum of only 1/34 of the sources, the BLRG 3C 445, requires such a description.

7) *Power Law + Thermal Bremsstrahlung.* The model consists of a power law of photon index  $\Gamma$  plus a thermal bremsstrahlung of temperature  $kT$  (keV), parameterizing excess flux at the soft energies in one BLRG (3C 382). This model also provides an acceptable (and equivalent to the power law) fit to the hard X-ray continuum of WLRGs, with temperatures  $kT \sim 100$  keV.

8) *Double Power Law (sum of two power law models).* This model parameterizes a curved (upward or downward) continuum. The parameters are the power-law photon indices,  $\Gamma_1$  and  $\Gamma_2$  for the lower- and higher-energy components, respectively, and the column density  $N_{\text{H}}$  ( $\text{cm}^{-2}$ ), acting on both power laws. This model describes the *ASCA* spectrum of the QSR, 4C +74.26, with an upward curved continuum.

9) *Power Law + Reflection.* This model parameterizes Compton scattering of the primary continuum by cold, dense matter in the immediate vicinity of the X-ray source (Lightman & White

1988; Guilbert & Rees 1988). We used the model `pexrav` (Magzdiarz & Zdziarski 1995) in `XSPEC` to parameterize reflection for the BLRGs and NLRGs for which a significant Fe line was detected (Table 4). The free parameters are as follows: photon index of the primary power law  $\Gamma$ , power law normalization  $N$ , reflected component normalization  $A$ . In Table 3 we give the reflection normalization  $A$  ( $A=1$  for an isotropic illuminating source). The inclination angle was fixed to the value from independent measurements from the literature, when available (see, for example, the compilation of Eracleous & Halpern 1998), or fixed at  $30^\circ$  (nearly face-on) for BLRGs, and  $90^\circ$  (edge-on) for NLRGs. The power law plus reflection model gives an acceptable (both from a statistical and physical point of view) fit to the data of a single BLRG, 3C 390.3, during the longest of the three observations.

### 4.3. Models for the Fe Line

Having determined the model that best-fits the continuum, we next attempted spectral fits to the full 0.6–10 keV datasets adding back the data at 5–7 keV rest-frame energies and including a Gaussian component to parameterize the Fe  $K\alpha$  line. As illustrated in Figure 1, evidence for an Fe line around 6 keV is present in several sources.

We first fitted the data with an unresolved-line model, fixing the Gaussian energy dispersion to  $\sigma = 0.05$  keV. This is comparable to the SIS resolution during the first few years of the *ASCA* mission; however, the SIS resolution has been degrading with time, reaching  $\sigma = 0.2$  keV during AO3. In the cases of spectra with low signal-to-noise ratio, the line energy was also fixed at the rest-frame energy of the Fe  $K\alpha$  emission line, 6.4 keV. The addition of the Gaussian component led to an improved fit at the  $P_F \gtrsim 95\%$  confidence level in 6 BLRGs, 1 QSR, 3 NLRGs, and 1 RG (with a marginal detection at a  $P_F \gtrsim 90\%$  confidence level in 3 additional RGs). Next, the fit was repeated allowing the line to be resolved. This gave an improved fit in all BLRGs and the QSR where the line was detected, with inferred FWHM  $\gtrsim 20,000$  km s $^{-1}$ , but not in the NLRGs and the RGs, where the line is unresolved. The results of the narrow- and broad-line fits are reported in Table 4, where we list the fitted line energy (column 2), Gaussian energy dispersion  $\sigma_{\text{rest}}$  (column 3), corresponding FWHM (column 4), and EW (column 5); all quantities have been transformed to the source rest-frame. In the cases where the Fe line is not detected, the 90% upper limit on the EW for a narrow ( $\sigma = 0.05$  keV) line at a rest energy of 6.4 keV is reported.

While the signal-to-noise ratio of the NLRGs and RGs spectra is, in general, relatively low, an additional difficulty in detecting an Fe line in these objects is the presence of a thermal plasma contribution. This component contributes to the Fe line emission, as shown, for example, in the spectra of PKS 2152–69 and Cygnus A in Figure 1. It is worth noting that in several NLRGs and RGs the residuals plotted in Figure 1 (SIS0 and SIS1) do show some excess flux around 6 keV at the  $\sim 1 - 2\sigma$  level which suggests a line. It will be important to observe these weak sources with more sensitive instruments such as *XMM* and *Astro-E* to confirm the Fe line and study its profile.

To refine our analysis of the Fe-line profiles, we fitted the *ASCA* data of the brightest BLRGs and the single QSR exhibiting a broad line with an accretion disk profile (Fabian et al. 1989; `diskline` in `XSPEC`). The model assumes that the line is produced in inner parts of the disk inclined at an angle  $i$ , between the two radii  $R_{\text{in}}$  and  $R_{\text{out}}$  (normalized to the gravitational radius), with an emissivity law  $\epsilon \propto R^{-\beta}$ . Following Nandra et al. (1997a), we fixed  $R_{\text{in}} = 6$  and  $R_{\text{out}} = 1000$  (average parameters for Seyfert 1s). The fits are rather insensitive to the values of the radii. The value of  $\beta$  was allowed to vary while the inclination angle was constrained by independent information on the radio morphology (superluminal speeds set an upper limit while a lower limit is given by the observed size of the large-scale, double-lobed radio source; Eracleous & Halpern 1998; Brinkmann et al. 1998). We find that a disk-like profile model provides a significantly better description only in the case of the long observation of 3C 390.3, where  $\Delta\chi^2=15$  with respect to the simple Gaussian profile (for the same number of degrees of freedom). The model parameters are:  $E_{\text{rest}} = 6.43 \pm 0.06$  keV,  $\text{EW}=132_{-48}^{+40}$  eV,  $i \sim 33^\circ$  (pegged at the upper limit allowed by the radio morphology),  $\chi_r^2 = 1.03$  (for 1158 degrees of freedom). Interestingly, this BLRG is well-known for the double-peaked profile of its Balmer lines, which has also been interpreted as due to emission from an accretion disk (Eracleous & Halpern 1994).

## 5. Distribution of Nuclear X-ray Properties

Figures 2a, 2b, and 2c show the distribution of the intrinsic spectral properties for the various classes of radio-loud AGN in our sample: the 2–10 keV photon index  $\Gamma$ , the 2–10 keV intrinsic (absorption-corrected) luminosity in the source rest-frame, and the excess column density  $N_{\text{H}}$ . The latter is defined as the difference between the fitted X-ray column of the power law component and the Galactic column in the direction to the source. Because of reports that the column densities measured by the *ASCA* SIS are overestimated by as much as  $3 \times 10^{20} \text{ cm}^{-2}$  (Dotani et al. 1996), we corrected the column densities in Figure 2c by subtracting the above amount. Only the sources where excess column densities were measured are plotted in Figure 2c. The average value and standard deviation of each of the quantities plotted in Figure 2 is reported in Table 5. For the photon index the weighted average is also listed for comparison with reports in the literature on other AGN samples. The weighted averages were computed using inverse variance weights; as such they are dominated by the objects with the highest signal-to-noise ratios.

*Photon Index* (Figure 2a): All classes of radio-loud AGN have similar distributions of photon indices in the range 1–2.2, with mean values  $\langle\Gamma\rangle = 1.7 - 1.8$ . When the RG class is divided into WLRGs and remaining sources, the WLRGs have much flatter spectra on average than any of the other classes, with  $\langle\Gamma\rangle = 1.5$ . The distributions and corresponding mean values for the various classes are not formally different according to the Kolmogorov-Smirnov and Student t-tests.

*X-ray Luminosity* (Figure 2b): The distributions of intrinsic X-ray luminosity of BLRGs, QSRs, and NLRGs overlap over the total range  $10^{42.5} - 10^{45.0} \text{ erg s}^{-1}$ . The luminosity distribution of RGs is broad, with most (3/5) of the WLRGs populating the low-luminosity tail at  $\lesssim 10^{41} \text{ erg s}^{-1}$ , more

than two orders of magnitude lower than the other classes. The distributions of BLRGs, QSRs, and NLRGs are only marginally different: a KS test yields a probability that the distributions are different of 94.7% for BLRGs *vs.* QSRs, 79.8% for BLRGs *vs.* NLRGs, and of 96.7% for QSRs *vs.* NLRGs. The distribution of X-ray luminosities of RGs differs from the distributions of all the other classes at  $\gtrsim 99.7\%$  confidence.

*X-ray column density* (Figure 2c): NLRGs and RGs have large intrinsic columns obscuring the source of the power-law component, with  $N_{\text{H}} \sim 10^{21}\text{--}10^{24} \text{ cm}^{-2}$ . A somewhat unexpected result is that similarly high excess columns are also observed in a fraction of BLRGs and QSRs, as apparent from Table 3. Table 5 lists the average column densities of the various classes; for BLRGs and QSRs we listed the mean values with and without 3C 445 and 3C 234, respectively, since in these two sources the absorbing medium appears to have a complex structure (see Table 3). The BLRG 3C 111 is located behind a molecular cloud in the Galaxy (Bania, Marscher, & Barvainis 1991), which could be responsible for the excess X-ray absorption observed (see discussion in Reynolds et al. 1998); this source was thus excluded from Figure 2c and the average column density in Table 5. The fraction of BLRGs and QSRs in Figure 2c where soft X-ray absorption is observed is 6/9, or 67%, and 3/5, or 60%, respectively, for which  $\Delta N_{\text{H}} \gtrsim 1 \times 10^{20} \text{ cm}^{-2}$ . Excess columns larger than  $\Delta N_{\text{H}} \gtrsim 10^{21} \text{ cm}^{-2}$  are observed in 4/9 (44%) BLRGs and in 3/5 (60%) QSRs.

*Trends with X-ray luminosity:* There are no apparent trends when the X-ray photon index and fitted column density of each individual object are plotted against the X-ray luminosity. However, from the *average* values of the photon index (weighted average, dominated by the brightest/best observed sources) and of the 2–10 keV luminosity in Table 5 there is an apparent trend of flattening slope with increasing luminosity going from RGs to QSRs (Fig. 2d). A Kendall non-parametric correlation test gives only a probability of  $\sim 95\%$  that a correlation is present. WLRGs stick out by having lower X-ray luminosities and much flatter spectral slopes than the remaining RGs and all NLRGs.

## 6. Multiwavelength Luminosity Correlations

In this section we investigate correlations between the *intrinsic* nuclear X-ray luminosity  $L_{2\text{--}10 \text{ keV}}$  (corrected for absorption and converted to rest-frame energies; Table 3) and the power at other wavelengths (from Table 1). To estimate the significance of correlations, we used the survival analysis package **ASURV** (Isobe, Feigelson, & Nelson 1986) which allows us to perform correlation analysis with censored data and take proper account of upper limits. We used the Kendall non-parametric test and calculated the correlation coefficient  $\tau_{12}$  and corresponding probability  $P_{\tau}$  that the correlation arises by chance. A small value of  $P_{\tau}$  indicates a significant correlation.

In examining luminosity-luminosity correlations for inhomogeneous samples like ours, it is customary to estimate the correlation probability once the common redshift dependence of both variables has been removed (partial correlation analysis). However, Feigelson & Berg (1984) have

argued that, in the presence of censored data, there is no need to remove the redshift dependence once the non-detections are properly weighted into the correlation test. The reason is that measuring a luminosity  $L_1$  at a wavelength  $\lambda_1$  does not affect *a priori* the distribution of luminosities  $L_2$  at a second wavelength  $\lambda_2$  if  $L_1$  and  $L_2$  are not intrinsically correlated. Moreover, since the fluxes at a given wavelength were generally measured in a uniform way (i.e., same instrument and sensitivity), the addition of upper limits can only weaken any intrinsic correlation between two luminosities. There is, however, the possibility of spurious correlations arising as a result of a common dependence on a third luminosity. To evaluate the correlation between two luminosities removing their common dependence on a third luminosity, we used the partial correlation test for censored data developed by Akritas & Siebert (1996), where upper/lower limits are properly weighted. The software was kindly provided by M. Akritas. From the partial Kendall coefficient,  $\tau_{12,3}$ , and the variance, the probability  $P_{12,3}$  of erroneously rejecting the null hypothesis (i.e., the probability of no correlation) can be estimated (Akritas & Siebert 1996). A small value of  $P_{12,3}$  indicates a significant correlation. The results of the correlation analysis are presented in Table 6. The format of the table is as follows: column 1 gives the total number of datapoints (we combine together the various classes); columns 2 and 3 list the independent variables and number of upper limits, while columns 4 and 5 list the dependent variables and number of upper limits. Columns 6 and 7 list the Kendall correlation coefficient,  $\tau_{12}$ , and corresponding probability,  $P_\tau$ , while columns 8–12 give the results of the partial correlation analysis, namely the third variable and number of corresponding upper limits, the partial Kendall coefficient  $\tau_{12,3}$  and the square root of the variance, and the partial correlation probability  $P_{12,3}$ . We emphasize that the luminosities used to perform the correlation tests in Table 6 are intrinsic, *rest-frame* values. Also, the QSR 3C 234 was excluded from every correlation test, since its true X-ray luminosity is uncertain, and so were 3C 28 and IC 310 (see Appendix).

It has been long known that the extended radio luminosity of radio galaxies is strongly correlated to the luminosity of the narrow emission lines (Rawlings et al. 1989; Rawlings & Saunders 1991). We also find a correlation between the 5 GHz lobe radio power and  $L_{[\text{O III}]}$ , with  $\tau_{12}=0.57$  and  $P_\tau = 1 \times 10^{-4}$ . Thus the lobe radio luminosity was included in the partial correlation analysis.

From Table 6 it is apparent that, after removing the various common dependences on other variables, the nuclear X-ray luminosity is primarily correlated with the [O III] and 12  $\mu\text{m}$  luminosities. These are the two most significant correlations, with a chance probability of  $P_{12,3} \lesssim 0.1\%$ . There is also a weaker correlation between  $L_{2-10 \text{ keV}}$  and the lobe radio power, with  $P_{12,3} \lesssim 3\%$ . These correlations are shown in Figure 3a, 3b, and 3c, respectively. The correlations between  $L_{2-10 \text{ keV}}$  and the core radio and 60  $\mu\text{m}$  luminosities appear to be the results of a common dependence on  $L_{[\text{O III}]}$ . We also verified that these correlations survive when the redshift dependence is removed. Our results hold when the subclass of WLRGs (which appears to have different properties; Tadhunter et al. 1998, Laing et al. 1994) is removed.

We note that the correlation between the X-ray and [O III] luminosities, shown in Figure 3a, holds over several orders of magnitude. The outlier at high [O III] luminosity is the NLRG 3C 321

where a starburst could be present (see Appendix). We performed a linear regression analysis to determine the slope of the correlation between  $L_{[\text{O III}]}$  and  $L_{2-10 \text{ keV}}$ , excluding 3C 321, the upper limits in Figure 3a, and WLRGs. We find  $L_{[\text{O III}]} \propto L_{2-10 \text{ keV}}^{1.2}$  or, more precisely,

$$\log L_{[\text{O III}]} = (1.2 \pm 0.2) \log L_{2-10 \text{ keV}} - (11 \pm 8)$$

when NLRGs and RGs are included, and

$$\log L_{[\text{O III}]} = (1.1 \pm 0.2) \log L_{2-10 \text{ keV}} - (6 \pm 22)$$

when NLRGs and RGs are excluded (i.e., for BLRGs and QSRs only). We also derive an empirical relation between the X-ray and 12  $\mu\text{m}$  luminosities, and between the X-ray and radio lobe luminosities, using only the firm detections and excluding the WLRGs, of the forms:  $L_{12 \mu\text{m}} \propto L_{2-10 \text{ keV}}^{0.8}$  or, more precisely,

$$\log L_{12 \mu\text{m}} = (0.8 \pm 0.1) \log L_{2-10 \text{ keV}} + (8 \pm 5),$$

and  $L_{\text{lobe}} \propto L_{2-10 \text{ keV}}^{0.9}$  or, more precisely,

$$\log L_{\text{lobe}} = (0.9 \pm 0.2) \log L_{2-10 \text{ keV}} + (2 \pm 7).$$

The error bars are based on the dispersion of the data points about the best fit. These relationships are plotted in Figures 3a-c (dotted lines). We conclude that there is a strong link between the nuclear X-ray power and the power of the [O III] emission line, the FIR luminosity at 12  $\mu\text{m}$ , and the lobe radio power for the sample of BLRGs, QSRs, NLRGs, and RGs. This suggests that the same process is ultimately responsible for powering the emission in all of these bands supporting and extending the conclusions of earlier studies (e.g., Rawlings & Saunders 1991). The correlation between the nuclear X-ray luminosity and the lobe radio power is particularly interesting and somewhat difficult to understand. It is unlikely that there is a direct causal connection between the two luminosities because the emitting regions (the AGN and the radio lobes) are separated by distances of order 100 kpc. We therefore take this correlation as an indication that the level of activity has been fairly steady over a time interval corresponding to the light-travel time between the AGN and the radio lobes, which is of order  $10^5$  to  $10^6$  years. WLRGs have underluminous [O III] emission lines (Fig. 3a) while being very powerful in the radio (Fig. 3c), consistent with their defining properties.

The origin of the non-linear relationship between the [O III] and X-ray luminosities is not clear. Wilkes et al. (1994) find a non-linear correlation (slope 1.41) between the optical and X-ray luminosity for a large sample of radio-loud and radio-quiet quasars. We note that, using only the BLRGs and QSRs of our sample (for which the optical luminosity is dominated by the nuclear emission with negligible starlight contamination), we find a correlation with  $L_{\text{opt}} \propto L_{2-10 \text{ keV}}^{1.03}$ . For the same sub-sample,  $L_{[\text{O III}]} \propto L_{2-10 \text{ keV}}^{1.05}$ , and a partial correlation analysis shows the latter is primary, with  $P_{12,3} < 0.04\%$ . Although based on a handful of sources, these results indicate that the [O III] luminosity is linearly and primarily correlated with the nuclear X-ray luminosity in type-1 radio-loud AGN. The addition of NLRGs and RGs results in a steepening of the correlation. This could be due simply to a non-linear response of the gas in the NLRs to the photoionizing continuum.

## 7. Summary of Observational Results

We studied the X-ray spectral characteristics of a sample of radio-loud AGN observed with *ASCA*, including 10 BLRGs, 5 QSRs, 9 NLRGs, and 10 RGs, the latter including 6 WLRGs. The principal observational results are:

- At low X-ray energies, a thermal emission component is present in the spectra of 67% of NLRGs and 100% of RGs, with temperatures in the range 0.7–6 keV. No such thermal component is detected in any of the BLRGs or QSRs.
- A power-law component is detected above 2 keV in 94% sources, including 5/6 WLRGs.
- The intrinsic 2–10 keV luminosity distribution of the power law component is similar in BLRGs, QSRs, and NLRGs in the range  $10^{42}$ – $10^{45}$  erg s<sup>-1</sup>. The distribution for RGs shows a low-luminosity tail, populated by the WLRGs, which have  $L_{2-10 \text{ keV}} \sim 10^{40}$ – $10^{42}$  erg s<sup>-1</sup>.
- The distribution of the 2–10 keV photon index is similar in BLRGs, QSRs, and NLRGs, with an average photon index  $\langle \Gamma \rangle = 1.7 - 1.8$ .
- In WLRGs the hard X-rays can be described equally well by either an absorbed power-law model with  $\langle \Gamma \rangle = 1.5$  (with individual slopes as flat as  $\Gamma = 1.3$ ), or a hot bremsstrahlung model with  $kT \sim 100$  keV.
- Absorption of the hard power-law component by cold matter is detected in 71% of NLRGs and 89% RGs, with  $N_{\text{H}} \sim 10^{21-24}$  cm<sup>-2</sup>. Similar column densities are also measured in 44% of BLRGs and 60% of QSRs.
- No ionized absorption between 0.6–1.0 keV is detected in the BLRGs and QSRs (with the exception of 3C 390.3).
- The Fe K $\alpha$  line is detected in 67% of BLRGs, 20% of QSRs, 33% of NLRGs, and 30% of RGs. In BLRGs and QSRs the line is broad, with FWHM  $\gtrsim 20,000$  km s<sup>-1</sup>. In the BLRG 3C 390.3, the Fe K $\alpha$  line profile is consistent with emission from a disk. In NLRGs and RGs the Fe line is unresolved. Some of these detections should be regarded with caution because of the poor signal-to-noise ratio of the spectra (e.g., 3C 321).
- The nuclear 2–10 keV luminosity is strongly correlated with the luminosity of the [O III] emission line, with a linear trend ( $L_{[\text{O III}]} \propto L_{2-10 \text{ keV}}^{1.05}$ ) for BLRGs and QSRs, and non-linearly ( $L_{[\text{O III}]} \propto L_{2-10 \text{ keV}}^{1.23}$ ) when NLRGs and RGs are added. The nuclear X-ray luminosity is also primarily correlated with the FIR emission at 12  $\mu\text{m}$  ( $L_{12 \mu\text{m}} \propto L_{2-10 \text{ keV}}^{0.83}$ ), and weakly with the lobe radio power ( $L_{\text{lobe}} \propto L_{2-10 \text{ keV}}^{0.92}$ ).



## 8. Discussion

### 8.1. The Soft X-ray Thermal Component

In about 67% of NLRGs and 100% of RGs a thermal component, best described by a Raymond-Smith plasma model, is detected with *ASCA* at low X-ray energies. This confirms previous results from *ROSAT* and *Einstein* that radio galaxies are embedded in a hot, diffuse medium (Fabbiano 1989; Worrall et al. 1994; Trussoni et al. 1997; Crawford et al. 1999), as well as more recent results obtained with *SAX* (Padovani et al. 1999). We detect the thermal emission component over a large range of redshifts ( $z = 0.007 - 0.46$ ) and intrinsic radio powers ( $L_{\text{lobe}} = 10^{40.8} - 10^{44.5}$  erg s $^{-1}$ ). While *ASCA* does not have a high enough angular resolution to study the morphology of the thermal component in detail, its high sensitivity allows us to determine its spectral properties.

The temperatures and luminosities determined from the *ASCA* spectra have a bimodal distribution. This is best illustrated in Figure 4, where the measured temperature is plotted against the X-ray luminosity. For comparison with published values for “normal” clusters (see below), we plot the intrinsic 0.1–2.4 keV luminosity of the thermal components. In four objects (PKS 0131–36, Centaurus A, Fornax A, and 3C 321), it is possible that the thermal component is related to a starburst or is of nuclear origin (see below and Appendix). These objects are marked with different symbols (stars) in Figure 4. It is apparent from Figure 4 that the sources make up two different groups in the  $L - kT$  plane. Several sources are grouped into a region of low luminosity and temperature ( $L_{0.1-2.4 \text{ keV}} \sim 10^{40-43}$  erg s $^{-1}$ ,  $kT \sim 1$  keV), close to the values measured in poor groups (Mulchaey & Zabludoff 1998) and/or in the hot coronae of elliptical galaxies (e.g., Fabbiano 1989). The remaining sources (4C +55.16, 3C 295, Cygnus A, 3C 28, IC 310, and PKS 0625–53) have higher temperatures and luminosities,  $L_{0.1-2.4 \text{ keV}} \gtrsim 10^{43}$  erg s $^{-1}$  and temperatures  $kT \sim 3 - 6$  keV, suggestive of larger-scale emission such as from the intergalactic gas in clusters of galaxies. Indeed, for these sources (except for PKS 0625–53) there is independent evidence from optical data for cluster associations (see Appendix). In general, our results support the findings of Zirbel (1997) that radio galaxies on average inhabit regions of moderate to low galaxy density. Unfortunately, our sample is insufficient to test the conclusion of Zirbel (1997) that FR I radio galaxies are in richer environments than FR IIs.

It is interesting to compare the X-ray spectral properties of the clusters hosting radio sources to those of clusters without radio sources. The latter are known to exhibit a tight correlation in the  $L - kT$  plane which evolves slowly with redshift (Mushotzky & Scharf 1997). Recently, Markevitch (1998) parametrized the relation between the temperature and luminosity of a number of clusters at  $z \sim 0.05$ , both with and without the cooling flow region. We show the resulting relations in Figure 4 in the form of dashed and dotted lines respectively, and compare it to our measured values for the sources in the upper-right diagrams which are known to reside in optical galaxy dense environments. Although the number of objects in our plot is small, it is apparent that on average the host clusters of radio sources do not differ significantly from normal clusters with or without cooling flows. The main outlier is PKS 0625 – 53, which appears to be underluminous for

its temperature [we double-checked the *ASCA* flux of the cluster with that measured by *ROSAT* in a similar energy range (Brinkmann, Siebert, & Boller 1994), and found good agreement]. Moreover, the metallicities of the host clusters inferred from the X-ray spectra are very similar to those of “normal” clusters, with an average value  $\langle Y \rangle = 0.48$  and dispersion 0.20. These results suggest that the presence of the radio source does not affect the large-scale properties of its environment, a conclusion reached independently by Zirbel (1997).

The role of the diffuse hot gas in confining the radio lobes and jets has been long discussed in the literature (Birkinshaw & Worrall 1992; Worrall, Birkinshaw, & Cameron 1995). For example, Morganti et al. (1988) studied a sample of radio galaxies in the radio and X-rays with the *Einstein* HRI and found a correlation between the radio size and the cluster deprojected central density, with smaller sources inhabiting denser environments. They also find a general balance between the thermal gas pressure and the radio lobe pressure, indicating that the gas is responsible for confining the lobes. These results confirmed the earlier claims of Feigelson & Berg (1985), who found a tight correlation between the radio lobe power and the 0.3–4.5 keV luminosities and concluded that the radio emission is enhanced in denser (and thus more luminous) clusters due to inhibited adiabatic expansion losses. However, Miller et al. (1985), examining a sample of radio galaxies in radio and X-rays, reached opposite conclusions. These authors showed that the external medium does not have enough pressure to confine the radio lobes which are continuously expanding into the gas. It has also been suggested that the external medium is fueling the central active nucleus through a cooling flow, and that the core radio emission depends on the amount of gas (and thus X-ray emission) in the vicinity of the AGN (Fabbiano, Gioia, & Trinchieri 1989). Indeed, evidence for a cooling flow has been claimed for at least three radio galaxies in our sample, 3C 270 (Worrall & Birkinshaw 1994), NGC 6251 (Birkinshaw & Worrall 1992), and 4C +55.16 (Iwasawa et al. 1999a) on the basis of *ROSAT* and *ASCA* data. In the case of the first two radio galaxies, Worrall & Birkinshaw (1994) and Birkinshaw & Worrall (1992) suggest specifically that the gas in the cooling flow is feeding the active nucleus.

If the amount of gas around the AGN is directly related to the activity in the lobes and/or in the core of the radio galaxy, one would naively expect to find a correlation between the gas X-ray luminosity and the radio lobe and core luminosities. We thus looked for possible correlations between these quantities in those radio galaxies in which thermal-plasma emission was detected with *ASCA*. We found only weak correlations between the X-ray luminosity of the thermal components,  $L_{X,\text{th}}$  (Table 3) and the radio luminosities of both the lobes ( $L_{r,\text{lobe}}$ ) and the cores ( $L_{r,\text{core}}$ ): the Kendall correlation coefficient and corresponding chance probability are  $\tau_{12}=0.463$  and  $P_\tau \sim 5\%$  in the case of the  $L_{X,\text{th}}-L_{r,\text{lobe}}$  correlation, and  $\tau_{12}=0.428$ ,  $P_\tau \sim 7\%$  for the  $L_{X,\text{th}}-L_{r,\text{core}}$  correlation. X-ray observations with higher spatial resolution (e.g., with *AXAF*) will undoubtedly shed more light on the role of the ambient gas in confining the radio structure and in triggering the nuclear activity.

## 8.2. IR Emission from Radio-Loud AGN

As shown in Table 1, several radio galaxies are powerful Far-IR (FIR) emitters. The origin of the FIR emission in radio galaxies is still a matter of debate. One possibility is thermal emission by dust in the ISM of the galaxy which is heated by UV light from the AGN (e.g., Impey & Gregorini 1993; Antonucci, Barvainis, & Alloin 1990). This possibility is also supported by the detection of CO( $J = 1 \rightarrow 0$ ) line emission in several radio galaxies, with large inferred H<sub>2</sub> masses (Mazzarella et al. 1993). Another possibility is that the IR flux is the result of beamed non-thermal emission from the synchrotron jet (Hoekstra, Barthel, & Hes 1997). An attractive feature of this scenario is that it seems to account for the higher 60  $\mu\text{m}$  luminosities of quasars compared to NLRGs (Hes, Barthel, & Hoekstra 1995; Heckman et al. 1994). While this hypothesis can hold for the most distant quasars (as in the samples of Heckman et al. and Hes et al.), we note that the sources in our sample are by selection at low redshifts and are all lobe-dominated ( $\log R < 0$ ), making the contribution of a beamed component to the FIR emission negligible. A third possibility is production of FIR flux in an advection-dominated accretion flow (ADAF), which will be discussed below (§8.4).

On the other hand, there is abundant observational evidence that dust is a constituent of the interstellar medium (ISM) of elliptical galaxies (Knapp et al. 1989; Bregman 1998; Goudfrooij 1998). It is introduced into the ISM by winds from evolved stars and planetary nebulae (Tsai & Mathews 1995) or externally through galaxy-galaxy mergers (e.g., van Dokkum & Franx 1995). Obvious locations for the dust are “cold” environments where the dust grains are shielded from sputtering by the hot radiation of stars and/or the active nucleus, for example in the commonly-observed dark lanes (e.g., de Koff et al. 1996). Another possible location is a flat, large disk formed by the cooling ISM in rotating ellipticals (Brighenti & Mathews 1997). An unresolved question is the origin of the radiation that heats the dust. The most likely possibilities include young, hot stars in the galaxy or an active nucleus. The strong correlation we find between the X-ray nuclear luminosity and the 12  $\mu\text{m}$  luminosity (§6) bolsters the idea that the nucleus is primarily responsible for heating the cold interstellar dust that emits in the FIR band. This is also supported by previous studies at other wavelengths which also established links between the FIR emission and other nuclear-related activity. For example, Impey & Gregorini (1993) find a correlation between the FIR emission and the core radio emission, with more powerful radio sources having warmer FIR colors. Golombek, Miley, & Neugebauer (1988) report that the IRAS fluxes of radio galaxies correlate with the presence of strong emission lines in their optical spectra. Interestingly, *ASCA* detects large amounts of cold gas in several radio galaxies with column densities around  $10^{21}$ – $10^{23}$   $\text{cm}^{-2}$ , suggesting the presence of dust in these objects. In particular, strong excess column densities are detected in the BLRG 3C 445 and the QSRs 3C 234 and 3C 109. These objects are among the most powerful FIR emitters in our sample and are known for exhibiting unusually steep IR-to-optical spectra (Elvis et al. 1984).

Impey & Gregorini (1993) find indirect evidence that most radio galaxies harbor large amounts of cold gas and suggest that star-formation is occurring in these objects at a rate comparable to that in spirals (see also Mazzarella et al. 1993). Since the 60  $\mu\text{m}$  emission is most sensitive to

thermal emission from a starburst (e.g., Spinoglio et al. 1995), we have collected in Table 1 the IRAS 60  $\mu\text{m}$  fluxes of the radio galaxies in our sample. We first note that only a few objects are detected at 60  $\mu\text{m}$ , which *per se* is already an indication that a starburst contribution is unlikely in radio galaxies as a class. To help identify objects where star formation could be occurring, we plot in Figure 5 the ratios of the 60  $\mu\text{m}$  to 12  $\mu\text{m}$  luminosity versus the nuclear hard X-ray (power-law) luminosity. We include only those objects which were clearly detected at 60  $\mu\text{m}$ . Objects with a starburst contribution in the FIR should be characterized by excess emission at 60  $\mu\text{m}$  at a given nuclear X-ray luminosity. From Figure 5 it is apparent that large IR excesses are present only in the cases of Cygnus A, Centaurus A, and the WLRGs PKS 0131–36 and Fornax A, where the 60-to-12  $\mu\text{m}$  flux ratios are a factor  $\gtrsim 2$  larger than in “pure” AGN (BLRGs and QSRs). Thus we conclude that a starburst contribution to the observed FIR flux is negligible *in general* in our sample. Indeed, the large radio fluxes locate our sources above the range in which the FIR/radio correlation for starburst galaxies holds (Condon, Frayer, & Broderick 1991). Nevertheless, a starburst contribution could be important in some individual cases in our sample. It is very interesting that two such sources are WLRGs (see discussion below in §8.4).

In summary, we conclude that the most likely explanation for the FIR emission observed in several radio galaxies in our sample is thermal reradiation from dust in the galaxy ISM illuminated by the active nucleus. This is supported by the strong correlation between  $L_{2-10 \text{ keV}}$  and  $L_{12 \mu\text{m}}$  which adds to previous evidence for a link between the FIR emission and the nuclear activity. A starburst contribution could be present only in a few individual radio galaxies, including two WLRGs.

### 8.3. Constraints on Unification Schemes for Radio-Loud AGN

Current unification scenarios for radio-loud AGN postulate that the differences between classes are merely the result of a different orientation of the observer relative to the symmetry axis of the system (Urry & Padovani 1995 and references therein). An essential ingredient of these orientation-based scenarios is the large obscuring torus, which hides the nucleus and the broad emission-line region in type 2 objects (NLRGs and RGs) but not in type 1 objects (BLRGs or QSRs). Observational support for this view comes from optical spectropolarimetric studies (e.g., Antonucci & Barvainis 1990), which generally show the presence of broad emission lines in polarized light in type 2 objects.

X-ray observations can provide an independent test of these ideas since the hard (2–10 keV) X-rays can penetrate through the large absorbing column of the torus. In principle one could get a direct view of the nucleus at  $\gtrsim 10 \text{ keV}$  for column densities up to approximately  $10^{24} \text{ cm}^{-2}$ , above which the torus becomes optically thick even to these energies. In this context one would expect NLRGs to look just like BLRGs or QSRs viewed from the side, i.e., to have a similar hard X-ray continuum shape and luminosity and heavy absorption. Bearing in mind that our sample is of modest size and certainly not statistically complete, our results are qualitatively in agreement

with these predictions. The continuum slope distributions of the three classes are very similar, spanning the same range of values (see Figure 2a). The nuclear power law emission in NLRGs (and RGs) is generally heavily absorbed, with measured column densities  $N_{\text{H}} \sim 10^{21}\text{--}10^{24} \text{ cm}^{-2}$ . The distribution of the intrinsic (absorption-corrected) 2–10 keV nuclear luminosities of NLRGs is similar to that of BLRGs and QSRs, suggesting that these sources contain nuclei with similar levels of activity, in general.

Additional support for unification scenarios comes from the strong correlation between the 2–10 keV luminosity and the [O III] emission-line luminosity (Fig. 3a). Remarkably, this correlation holds for more than four decades in luminosity from QSRs to RGs. Besides supporting unification scenarios *qualitatively*, this correlation also suggests that the narrow emission-line regions of radio-loud AGN are photoionized by the nuclear emission, similarly to radio-quiet AGN (Mulchaey et al. 1994). It is worth noting, however, that the relation between the X-ray and [O III] luminosities is non-linear,  $L_{[\text{O III}]} \propto L_{2\text{--}10 \text{ keV}}^{1.2}$ , when NLRGs and RGs are included. A possible explanation for this effect includes a higher ionization state of the narrow-line gas with X-ray luminosity. Our results confirm earlier claims that the luminosity of the forbidden oxygen lines scales non-linearly with the non-thermal (optical) continuum, based on a mixed sample of radio-loud and radio-quiet sources (e.g., Yee 1980; Rawlings et al. 1989).

However, our detection with *ASCA* of a population of underluminous radio sources is not easily to reconcile with a simple orientation-based scheme. As Figure 2b shows, we find that a sub-class of RGs, the WLRGs, host nuclei which are underluminous in the hard X-rays by almost two orders of magnitude than the remaining objects. This indicates that another possible free parameter of unified schemes is the nuclear luminosity. A similar suggestion was also made by Hill, Goodrich, & De Poy (1996) based on the consideration that it is difficult to explain the higher UV, FIR, and [O III] luminosities of quasars with respect to NLRGs based on obscuration effects alone. Similarly, WLRGs have underluminous [O III] emission lines for their X-ray luminosities (Fig. 3a). We speculate that this is due to their weaker far-UV ionizing continua (as discussed below, §8.5). Thus, the *ASCA* data strengthen the case that the unified schemes in their simplest form are insufficient to account for the entire observational picture.

In principle, the profile of the Fe line affords another test of unification scenarios. Studies of Seyfert galaxies with *GINGA* and *ASCA* have shown that in Seyfert 1s the Fe line is broad and asymmetric to the red, suggesting an origin in an accretion disk around the central black hole (Nandra et al. 1997a; but see also the critique of Weaver & Yaqoob 1998). In Seyfert 2s, on the other hand, the Fe line typically has a very large EW (Smith & Done 1997; Turner et al. 1997a) and its profile consists of a narrow core, which is the signature of the outer obscuring torus (Weaver & Reynolds 1998), superposed on a broad base. Unfortunately, the *ASCA* spectra of radio-loud AGN set only loose constraints on the Fe line, in practice, because of their poor signal-to-noise ratio. The poor signal-to-noise ratio is a particularly serious handicap in NLRGs and RGs because their spectra are contaminated by a contribution from a thermally-emitting plasma. We were able to detect the Fe line with high confidence in two type 2 objects, Cygnus A and Centaurus A (see Table

4), and only marginally in the WLRGs PKS 0131–36 and 3C 270, and for NGC 6251. In all cases the line is unresolved, with an EW in the range 100–700 eV. The measured EWs are consistent with fluorescence in cold material with column densities  $10^{22}$ – $10^{23}$  cm $^{-2}$  (Leahy & Creighton 1993). Thus the *ASCA* data for the Fe line would tend to support unification schemes in their simple form, but do not allow us to reach more specific conclusions.

Even in BLRGs the study of the Fe K $\alpha$  line profile is plagued by practical difficulties, the most important one being the dependence of the profile on the description of the underlying continuum in the *ASCA* band. This is exemplified by the case of the BLRG 3C 382, where different authors fit the continuum with different models and find different line profiles (see discussion in the Appendix). Thus we cannot confirm the result of Woźniak et al. (1998) that BLRGs as a class have narrow and weak Fe lines. We measure instead a large range of EWs in BLRGs which could well be a result of this practical problem. Significant progress can be made only with broad-band X-ray spectra with a high spectral resolution at the Fe line region. Such spectra can be obtained through simultaneous *RXTE* + *ASCA* observations (e.g., Weaver, Krolik, & Pier 1998). Future instruments, namely *XMM* and *Astro-E*, can also provide data that are useful in this respect.

#### 8.4. Soft X-ray absorption in radio-loud AGN

An interesting result of our work is the detection with *ASCA* of soft X-ray excess cold absorption in a fraction (44–60%) of BLRGs and QSRs, with excess column densities  $\Delta N_{\text{H}} \gtrsim 10^{21}$  cm $^{-2}$  (Figure 2c and Table 5). The presence of excess X-ray absorption is also confirmed by published *ROSAT* and *SAX* data of several of these sources (3C 120, Grandi et al. 1997; 3C 390.3, Eracleous et al. 1995, Grandi et al. 1999; 3C 109, Allen & Fabian 1992; 4C +74.26, Brinkmann et al. 1998). In the following subsections we discuss two possible scenarios for the origin of the excess X-ray absorption, including a local origin in the Galaxy and an intrinsic absorber to the source.

##### 8.4.1. Origin in the Galaxy

A first possibility is that the excess column density is local to the Galaxy, and is due to absorption by molecular gas and/or dust, to which radio surveys at 21 cm are insensitive. A local origin for the excess absorption is entirely possible in the case of the BLRG 3C 111, which is located behind a dark cloud in the Galaxy (Bania, Marscher, & Barvainis 1991). From the intensity of the  $^{12}\text{CO}$  emission in the direction of 3C 111, the latter authors estimate that the molecular hydrogen column density in the direction to this source is  $N_{\text{H}_2} \approx 9 \times 10^{21}$  cm $^{-2}$ . The total Galactic column in the direction of 3C 111 is  $N_{\text{H}}^{\text{Gal}} \approx 1 \times 10^{22}$  cm $^{-2}$ , enough to account for the excess X-ray column measured by *ASCA* (Table 3; see also the discussion in Reynolds et al. 1998). We conclude that the excess X-ray column in 3C 111 could have an origin in the Galaxy, and exclude this source in the following discussion.

We checked for CO emission in the direction of all of the BLRGs and QSRs with highly-absorbed X-ray spectra by examining published surveys (Désert, Bazell, & Boulanger 1988; Liszt & Wilson 1993; Liszt 1994). Only 3C 120 was observed, but no CO emission was detected in the direction to this source (Liszt & Wilson 1993). Of the remaining sources, only 4C +74.26 is at a relatively low Galactic latitude ( $b = 19^\circ.5$ ), such that the probability of being associated with a molecular cloud could be non-negligible. The other sources are located at high latitudes,  $|b| \gtrsim 27^\circ$ , where the average density of the molecular gas is low,  $\langle N_{\text{H}_2} \rangle = 7.3 \times 10^{19} \text{ cm}^{-2}$  (Blitz, Bazell, & Désert 1990). We thus conclude that molecular gas is unlikely to be responsible for the high absorbing columns in most of our BLRGs and QSRs, with the possible exception of 4C +74.26.

The total column density of gas *and* dust in the Galaxy can also be traced by means of its emission in the infrared band, in particular at  $100 \mu\text{m}$ . The *IRAS* survey showed that the Galactic IR emission consists of several discrete “cirrus” features, associated with dusty clouds with column densities  $\sim 10^{20} \text{ cm}^{-2}$  superposed onto a more diffuse component (Low et al. 1984), with larger IR fluxes corresponding to larger column densities. From the available *IRAS*  $100 \mu\text{m}$  maps and adopting a conversion factor from IR flux to column density of  $8.5 \times 10^{-21} \text{ mJy sr}^{-1}/\text{cm}^{-2}$  (Rowan-Robinson et al. 1991), we derive total column densities in good agreement with the Galactic columns in Table 1 for all the X-ray absorbed BLRGs and QSRs, showing that cirrus obscuration is negligible.

In summary, on the basis of the available CO and IR data, we conclude that contributions from the molecular gas and dust in the Galaxy to the observed X-ray excess absorption in BLRGs and QSRs is unlikely, with the exception of 3C 111 and, possibly, 4C +74.26. In the remaining sources, the X-ray absorber is extragalactic in origin, and is most plausibly associated with the AGN itself.

#### 8.4.2. *Intrinsic X-ray absorption*

Two locations are possible for an intrinsic absorber: the host galaxy or a surrounding cluster, and the AGN central engine itself. A location of the X-ray absorber in the host galaxy (e.g., a cooling flow) and/or in the larger-scale environment of the radio source cannot be ruled out *a priori*. We note, however, that all the BLRGs and QSRs from our sample with highly absorbed spectra are found to inhabit relatively poor optical clusters (see list of Zirbel 1997), which is common for FR II radio galaxies. Moreover, there are no reports of cooling flows around these objects. Instead, the presence of intrinsic reddening in several cases (3C 445, 3C 109, 3C 234) supports a nuclear origin for the X-ray absorber, or at for least part of it. In addition, the latter was observed to vary significantly in at least one BLRG, 3C 390.3 (Grandi et al. 1999)<sup>4</sup>, supporting a nuclear location.

---

<sup>4</sup>In 3C 390.3 the *ASCA* data suggest the presence of an additional component of warmer absorbing gas. In fact, we detect an absorption edge at  $\sim 0.7 \text{ keV}$  (which we interpret as the K-edge of O VII), with column densities  $N_{\text{H,gas}} \approx 8 \times 10^{20} \text{ cm}^{-2}$  (see Appendix), similar to the column of cold gas. The presence of this additional warm

Based on the above evidence we consider it unlikely that the absorber is associated with the host galaxy or its environment.

The *ASCA* data provide initial constraints on the physical state of the X-ray absorber in most sources. A cold gas is clearly indicated in the cases of 3C 390.3, 3C 445, 3C 109, and 3C 234, because of the shape of the spectra at soft X-rays (Table 3 and Figure 1). This is also supported by *ROSAT* PSPC and *SAX* observations of these objects (Allen & Fabian 1992; Sambruna et al. 1998; Grandi et al. 1999). In 3C 445 and 3C 234, there seems to be reprocessing of the soft X-ray flux (modelled as a dual absorber/partial covering; see also Appendix). The presence of cold gas in these BLRGs and QSRs is at odds with the view that the line of sight to the nucleus in type 1 objects should be free of cold material.

In the case of 3C 303, 4C +74.26, and PKS 2155+11 the nature of the absorber detected by *ASCA* is less clear. Although the data are well fitted by a cold absorber (Table 3), a warmer gas can not be excluded. In the latter case, the most prominent features would be absorption edges of highly-ionized oxygen (O VII/VIII at rest-frame energies 0.7–0.8 keV). These would be redshifted to 0.5–0.6 keV, at the cutoff of the SIS sensitivity, mimicking “cold” absorption. Future broad-band, high-resolution X-ray observations of these sources will provide better constraints.

Our BLRGs and QSRs with excess X-ray absorption are not isolated cases. X-ray column densities larger than Galactic were also measured with the *ROSAT* PSPC in the BLRGs 3C 332 ( $z=0.151$ ), 3C 287.1 ( $z=0.216$ ), and Arp 102B ( $z=0.0244$ ) (Crawford & Fabian 1995; Halpern 1997). Interestingly, soft X-ray absorption is also detected with *ASCA* and *ROSAT* in about 30% of high-redshift (radio-loud) QSRs up to  $z \sim 3$  (Elvis et al. 1994, 1998; Cappi et al. 1997; Fiore et al. 1998), with intrinsic column densities  $\sim 10^{22} \text{ cm}^{-2}$ . These columns were not observed in radio-quiet QSOs of similar redshift, suggesting the excess absorption is found preferentially in radio-loud objects. Based on the statistical association of X-ray and optical absorption, Elvis et al. (1998) propose that the soft X-ray absorption is due to a photoionized gas in the central engine of the quasar. This interpretation is supported in a few sources of intermediate redshift ( $0.4 \lesssim z \lesssim 1$ ) by X-ray spectra of high signal-to-noise ratio, which allow detailed modelling (Fiore et al. 1993; Mathur et al. 1994). Absorption in a dusty nuclear outflow has also been suggested (Mathur 1994).

Assuming that the absorber is intrinsic in all the BLRGs and QSRs of our sample, we determined the intrinsic (rest-frame) column densities by fitting an absorption model to their *ASCA* spectra. The model consisted of the best-fit continuum model in Table 3, plus local absorption ( $z = 0$ , column fixed to the Galactic value of Table 1) and intrinsic absorption in the rest-frame of the AGN ( $z_{abs} = z_{source}$ , column treated as a free parameter). The best-fitting values of the intrinsic column,  $N_{H,intr}$ , are given in Table 7 together with the absorption-corrected 2–10 keV luminosity. 3C 120 and Pictor A are not included, since  $N_{H,intr}$  is  $\lesssim 3 \times 10^{20} \text{ cm}^{-2}$ , consistent with the SIS systematic uncertainties (Dotani et al. 1996). The sources reported in Table 7 are the BLRGs and

---

absorber could complicate absorption variability studies in this source.



QSRs of our sample where *bona fide* excess X-ray absorption is found from the *ASCA* data.

Figure 6 shows the plot of  $N_{\text{H,intr}}$  versus the X-ray luminosity for the BLRGs and QSRs of Table 7 (filled dots and triangles, respectively). Also plotted for comparison are the high- $z$  radio-loud quasars from the samples of Cappi et al. (1997) and Elvis et al. (1994), where large intrinsic columns were detected with *ROSAT* and *ASCA* (open triangles). The three open dots represent the BLRGs Arp 102B, 3C 332, and 3C 287.1, where excess X-ray columns were measured with the *ROSAT* PSPC (Halpern 1997; Crawford & Fabian 1995); the asterisks are the QSRs 3C 351 and 3C 212, where an ionized absorber is thought to be present (Fiore et al. 1993; Mathur 1994). It is noteworthy that Arp 102B and 3C 332 also feature metastable Fe II absorption lines in the near UV which could originate in the same medium that is responsible for the X-ray absorption (Halpern 1997). It is also very interesting that a few of the heavily X-ray-absorbed BLRGs and QSRs of our sample, including 3C 445, 3C 234, and 3C 109, exhibit strong polarization of the optical continuum and/or broad lines (Antonucci 1984; Goodrich & Cohen 1992; Corbett et al. 1998; Kay et al. 1999), confirming the presence of large amounts of gas along very close to their central engines.

Figure 6 shows no obvious trend between the absorbing column density and the X-ray luminosity. On the contrary, it appears that radio-loud AGN exhibit similar excess X-ray column densities over more than four orders of magnitude in luminosity. This observation contradicts the “receding torus” scenario of Hill et al. (1996) in which the absorbing medium subtends a smaller solid angle to the primary X-ray source with increasing luminosity.

In conclusion, we detected with *ASCA* excess X-ray absorption in a fraction of BLRGs and QSRs, also confirmed in a few cases by independent observations with other X-ray instruments. A cold absorber, most likely of nuclear origin, is the favored explanation in most cases, although a higher-ionization gas cannot be ruled out in the more distant sources of our sample based on the *ASCA* data alone. Interestingly, the excess X-ray columns are similar to those observed in higher- $z$  radio-loud quasars over more than 4 decades in X-ray nuclear luminosity. This stresses the importance of the X-ray absorber as a fundamental constituent of radio-loud AGN. Future higher-resolution X-ray observations are necessary to clarify the physical and dynamical conditions of the medium, and constrain its location.

### 8.5. The Low-Luminosity AGN in Weak Line Radio Galaxies

Perhaps one of the most interesting results of our study is the detection of WLRGs in hard X-rays. As discussed above, these objects represent a relatively recent discovery, sticking out in the sample of Tadhunter et al. (1998) as powerful radio-galaxies with underluminous [O III] emission lines and line ratios indicative of a low ionization state of the narrow-line region. Radio galaxies with similar properties were also discussed by Laing et al. (1994) who identified a class of “low-excitation” radio sources and noted that they formed a separate group with distinct optical properties. Tadhunter et al. (1998) advance the hypothesis that the most likely explanation for the

properties of WLRGs is that they harbor a low luminosity AGN. The *ASCA* data presented here give us the first view of these systems at hard X-rays. We find that in five out of the six WLRGs observed, the X-ray spectrum can be decomposed into a hard X-ray component plus a soft thermal component with  $kT \sim 1$  keV. The hard component can be described by either a flat power law, with  $\langle \Gamma \rangle = 1.5$  (and individual slopes as flat as  $\Gamma = 1.3$ ). The intrinsic luminosity of the hard component is  $L_{2-10 \text{ keV}} \sim 10^{40} - 10^{42} \text{ erg s}^{-1}$ , two orders of magnitude fainter than in the other radio sources.

The  $[\text{O II}]/[\text{O III}]$  line ratios of WLRGs locate them in the LINER/H II-region part of the diagnostic line-ratio diagrams of Filippenko (1996), raising the possibility that WLRGs represent the radio-loud analogs of LINERs. In fact, Fornax A is included in the LINER sample studied by Fabbiano (1996) on the basis of its optical spectroscopic properties presented by Baum, Heckman, & van Breugel (1992). The similarity between LINERs and WLRGs is reinforced by the ubiquitous soft X-ray thermal component, which could be related to a starburst in one (PKS 0131–36) and possibly two (Fornax A) of the WLRGs. As in WLRGs, the *ASCA* spectra of LINERs and other low-luminosity AGNs are also made up of a soft, thermal component plus a hard power law. However, the spectra of (radio-quiet) LINERs are considerably steeper than those of WLRGs of similar luminosities. The photon indices in LINERs are  $\Gamma \sim 1.7\text{--}1.8$  (Serlemitsos, Ptak, & Yaqoob 1996), compared to  $\Gamma \sim 1.5$  in WLRGs. We note that the X-ray spectra of WLRGs are also much flatter than those of all other radio-loud AGN in our sample, suggesting a fundamental difference.

There is considerable debate as to whether the hard X-ray emission of LINERs originates in a low-luminosity active nucleus or whether alternative mechanisms (e.g., the collective emission from a large number of X-ray binaries at near-Eddington luminosities) are more viable. Similar arguments hold for WLRGs. In the case of WLRGs, however, the presence of kpc-sized radio jets and lobes as well as compact radio cores makes an ironclad case for the presence of an AGN. The real question is whether the observed X-ray flux comes from the AGN or from some other process. While only future high-resolution *AXAF* observations will settle the issue definitively, we can still make a few comments here. Available *ROSAT* PSPC and HRI images do not show evidence for discrete X-ray binaries or other point-like sources in Fornax A (Fabbiano 1996; Kim, Fabbiano, & Mackie 1998), in 3C 270 (Worrall & Birkinshaw 1994), or in PKS 0131 – 36 (archival *ROSAT* HRI data). In 3C 270, the *ROSAT* PSPC data show explicitly the presence of a spatially unresolved component, with a power law spectrum, which is attributed to an AGN (Worrall & Birkinshaw 1994). There is marginal evidence for an Fe line in the *ASCA* spectra of two WLRGs, with EWs  $\sim 250$  eV. If confirmed this would provide support in favor of an AGN origin of the bulk of the X-ray luminosity.

An interesting possibility is that the accretion flows in the active nuclei of WLRGs are advection dominated (hereafter ADAFs; Ichimaru 1977; Rees et al. 1982; Narayan & Yi 1994, 1995; see Narayan, Mahadevan, & Quataert 1998 for a recent review). ADAFs are possible if the accretion rate is very low relative to the Eddington rate, i.e., when  $\dot{m} \lesssim \alpha^2 \dot{m}_{\text{Edd}}$  (where  $\alpha$  is the Shakura-Sunyaev viscosity parameter). At these low densities, the Coulomb collisions between the ions and

the electrons are an inefficient means of equilibration, and the plasma settles into a two temperature phase, with the ions being much hotter than the electrons ( $T_i \sim 10^{11}$  K,  $T_e \sim 10^9$  K). The ions take most of the potential energy and advect it to the black hole, while the relativistic electrons radiate a small fraction of it. The emission is by the synchrotron, inverse Compton, and bremsstrahlung mechanisms, with the output in the radio, optical, and hard X-rays, respectively. The X-rays in particular provide very sensitive constraints on ADAF models, since the slope of the X-ray spectrum is a sensitive function of the accretion rate (see, for example, Figure 6 of Narayan et al. 1998). At low densities the dominant X-ray emission mechanism is bremsstrahlung with  $h\nu_{B,\max} \sim kT_e \sim 100$  keV (Narayan et al. 1998), while when the density increases inverse Compton losses are more important and the X-ray spectrum is a steeper power law. ADAFs have been successful in accounting for the relatively flat X-ray spectra and low X-ray luminosities of NGC 4258 (Lasota et al. 1996), M87 (Reynolds et al. 1996), and M60 (Di Matteo & Fabian 1997). These models are particularly attractive for radio-loud AGN since some of the gas in an ADAF is unbound and may escape in an outflow, potentially forming a jet (Blandford & Begelman 1999; see also Narayan & Yi 1994, 1995 for ADAFs and relativistic jets).

The alternative possibility that the flat X-ray slopes of WLRGs are due to the beamed contribution from the inner parts of the radio jet is ruled out by the lack of correlation between their nuclear X-ray luminosities and the core radio emission. In fact, all WLRGs in the present sample are lobe-dominated (Table 1), assuring that the jet emission is beamed away from the line of sight.

Are ADAFs consistent with the observed low luminosities and flat X-ray slopes of WLRGs? We study the case of 3C 270 (hosted by the giant elliptical NGC 4261) since for this WLRG there is an accurate dynamical estimate of the central mass from recent *HST* observations (Ferrarese, Ford, & Jaffe 1996):  $M_{\text{BH}} = (4.9 \pm 1.0) \times 10^8 M_{\odot}$  (a factor 10 lower than in M87). This implies an Eddington luminosity  $L_{\text{Edd}} \sim (5-8) \times 10^{46}$  erg s<sup>-1</sup>. The radio-to-X-ray spectral energy distribution of 3C 270 is shown in Figure 7 (using data from Table 1, the *ASCA* data, optical nuclear fluxes from Ferrarese et al. 1996, and an UV upper limit from the *HST* observations of Zirbel & Baum 1998). Also plotted for comparison is the spectral distribution of M87, where an ADAF is thought to be present (Reynolds et al. 1996), and for which a recent analysis of the *ASCA* data has given a flat X-ray slope,  $\Gamma = 1.40_{-0.46}^{+0.37}$  (Allen, Di Matteo, & Fabian 1999), similar to what we measure in 3C 270 and other WLRGs. Integration of the flux of 3C 270 from radio to X-rays gives a bolometric luminosity of  $L_{\text{Bol}} \sim 2 \times 10^{43}$  erg s<sup>-1</sup>; this probably overestimates the true nuclear luminosity, because it includes the IR datapoints, where contribution from the nuclear dust could be present. Thus,  $L_{\text{Bol}}/L_{\text{Edd}} \lesssim (2-4) \times 10^{-4}$ , placing 3C 270 in the ADAF regime. Note the lack of UV continuum emission, too shallow to be entirely due to dust absorption. We speculate that the lack of a strong far-UV ionizing continuum is the cause of the observed underluminous [O III] emission lines.

It is worth noting that not all WLRGs have abnormally flat X-ray continua even though they all have low X-ray luminosities. For example, in 3C 353 the measured 2–10 keV photon index is 1.9, very similar to the values found in Seyfert galaxies. Interestingly, 3C 353 is a powerful FR II

radio galaxy, while 3C 270 is a lower-power FR I radio galaxy<sup>5</sup>. It is tempting to speculate that WLRGs represent that segment of the population of radio-loud AGN in which the accretion rate is so low that an ADAF is inevitable. The exact shape of the X-ray spectrum would depend on the exact value of the accretion rate, hence a range of spectral slopes would be possible.

Also interesting is the tentative detection with *ASCA* of an Fe line in two WLRGs, 3C 270 and PKS 0131–36 (Table 4). Future observations of these and other WLRGs at higher-sensitivity (e.g., with *XMM*) will allow us to study the line profile and energy, discriminating among possible scenarios for its origin. Particularly intriguing is the possibility that the Fe line originate from the coronal gas in the outer parts of the ADAF (Narayan & Raymond 1999). In this case, soft X-ray lines would be expected as well, and from their relative strength the size and dynamical conditions of the ADAF can be diagnosed (Narayan & Raymond 1999).

In the context of ADAF models a large energy output in the IR/FIR band is expected (e.g., Narayan et al. 1998). Since the FIR flux originates in the thin disk exterior to the ADAF, it would be expected to vary on short timescales. FIR flux variability in WLRGs could thus provide a diagnostic tool to discriminate between an AGN (ADAF) and a dust/starburst origin for their FIR emission.

### 8.6. The Radio-Loud/Radio-Quiet AGN Dichotomy

Various samples of radio-quiet AGN have been studied with *ASCA* by different authors recently, allowing a systematic comparison with our sample of radio-loud objects. The main advantage of comparing samples of radio-loud and radio-quiet AGN observed with the same instrument is that the systematic effects are the same and hence are unlikely to affect the results. In particular, compilations of *ASCA* results for Seyfert 1s, Seyfert 2s, and QSOs have been presented by Nandra et al. (1997a), Turner et al. (1997a), and Reeves et al. (1997), respectively. We extracted from these studies subgroups of objects in a range of intrinsic (rest-frame) 2–10 keV luminosities matching the range of the corresponding subclass of radio-loud objects. We also used the collection of LINERs from Serlemitsos et al. (1996) for comparison with the WLRGs. This gave 7 Seyfert 1s, 13 Seyfert 2s, 7 QSOs, and 4 LINERs. Their average photon indices and luminosities are reported in Table 5.

The distribution of spectral indices of Seyfert 1s, Seyfert 2s, and QSOs are compared to those of their radio-loud counterparts in Figure 2a (dotted histograms). A Kolmogorov-Smirnov test gives a probability of only  $P_{KS} \sim 94\%$  that the distribution for Seyfert 1s and BLRGs are different, while their average photon indices,  $\langle \Gamma_{BLRGs} \rangle = 1.6$  and  $\langle \Gamma_{Sy\ 1s} \rangle = 1.9$ , differ at 93% according to a Student t-test. The distribution of photon indices for the QSR/QSO, NLRG/Sy 2, WLRG/LINER samples are not demonstrably different. The average values for the last pair differ at the 95% confidence level, with WLRGs having flatter spectra than LINERs.

---

<sup>5</sup>Of the 23 WLRGs in Tadhunter et al. (1998), 61% are of the FR I type while 40% have FR II morphologies.

We thus conclude that *ASCA* does not provide evidence that radio-loud AGN have flatter X-ray spectra than their radio-quiet counterparts. The observed difference in photon indices between BLRGs and Seyfert 1s (the only case where the two distributions are significantly different) is  $\Delta\Gamma \sim 0.3$ . This is less than the  $\Delta\Gamma \sim 0.5$  found in samples observed with *Einstein* (Wilkes & Elvis 1987) and *EXOSAT* (Lawson et al. 1992). One difference from earlier results is that we have matched the radio-loud and radio-quiet AGN samples in X-ray luminosity, which was not always possible in previous studies. In so doing, we took into account possible intrinsic trends with luminosity and we compared spectral slopes by subclass. More importantly, our sample also differs from previous ones in including only lobe-dominated radio sources in which beaming is unlikely to be important. The effect of beaming was more important in samples presented in the literature (Wilkes & Elvis 1987; Shastri et al. 1993; Lawson & Turner 1997), especially when high-redshift objects were included. Our results thus show that the X-ray spectral slopes of radio-loud and radio-quiet AGN are intrinsically similar, confirming that a beamed component from the inner regions of the radio jet is responsible for the flatter slopes previously observed.

A leading model for the production of the X-ray continuum in Seyfert galaxies is Comptonization of thermal photons from the disk (Haardt & Maraschi 1993), which can produce photon indices in the large range 1.4–2.0. This model can thus accommodate the observed spectral indices of radio-loud AGN of  $\Gamma \sim 1.7$  and there is no need for special geometry or physical processes for them *based on their ASCA spectral slopes alone*. Besides, a few Seyferts also exhibit flatter than average spectral indices, which are comparable to those of WLRGs. Examples include Mrk 841 (George et al. 1993) and 1H 0419 – 577 (Turner et al. 1999).

Perhaps the most intriguing observational evidence so far in favor of differences in the accretion flows of radio-loud and radio-quiet AGN is provided by high-energy observations. Woźniak et al. (1998) studied archival *GINGA* and *CGRO/OSSE* spectra of BLRGs and reported that these objects have weaker Compton reflection components than Seyferts (Nandra & Pounds 1994; Weaver et al. 1998). These findings are also confirmed by recent observations with *RXTE* (Eracleous, Sambruna, & Mushotzky 1999, Rothschild et al. 1999) and *SAX* (Grandi et al. 1999). The simplest interpretation is that the dense, cold reprocessor in radio-loud objects subtends a smaller solid angle to the central X-ray source. This would be the case, for example, if the inner disk were of a vertically extended, quasi-spherical structure such as an ion torus (Rees et al. 1982), or an ADAF (see the estimate of Chen & Halpern 1989). The lower photon indices measured by *ASCA* for radio-loud AGN fit well into this picture, since flat X-ray continua are expected from ADAFs. Also, the non-linear variability trends of the X-ray flux, such as observed for 3C 390.3 (Leighly & O’Brien 1997), find a natural explanation in ADAFs.

If the cold reprocessor in BLRGs is indeed at larger distances from the central black hole than in radio-quiet AGN, then one expects also to observe narrower Fe  $K\alpha$  lines in BLRGs. Indeed Woźniak et al. (1998) claimed to have observed such an effect, although we can neither confirm nor disprove their results. Figure 8 shows a plot of the Fe line EWs, or their 90% upper limits, versus intrinsic continuum X-ray luminosity for the BLRG and QSR sub-classes of radio-loud AGN that

we have studied (updated from Eracleous & Halpern 1998). The shaded area is the  $EW - L_X$   $1\sigma$  relationship (the X-ray Baldwin effect) for radio-quiet AGN found by Nandra et al. (1997c). Radio-loud AGN have a large dispersion of EWs around the shaded area. We suggest that uncertainties in determining the continuum in the vicinity of the Fe line limit one’s ability to measure the properties of the line profile.

Another result of our work is the edence for different gas environments in radio-loud AGN. Recent systematic studies of Seyfert 1s with *ASCA* (Reynolds 1997; George et al. 1998) show that a large fraction (13/18, or 72%) of the objects studied exhibit ionized absorption, which manifests itself as absorption edges in the observed energy range 0.6–0.8 keV. Thanks to the sensitivity of *ASCA* at energies  $\lesssim 1$  keV it is possible to set interesting limits to the amount of ionized gas along the line of sight in the BLRGs of our sample. We find that only one BLRG (3C 390.3) exhibits an absorption edge at  $\sim 0.78$  keV (which we thus interpret as the O VII edge), with optical depth  $\tau \sim 0.3$ . The latter corresponds to a column density of ionized gas  $N_{\text{H,gas}} \sim 8 \times 10^{20} \text{ cm}^{-2}$ , at the lower end of the distribution for Seyfert 1s of similar X-ray luminosity (Reynolds 1997; George et al. 1998). Thus, radio-loud AGN appear to have smaller amounts of ionized gas around their nuclear X-ray sources than Seyferts. Instead we have detected large columns of cold gas in BLRGs and QSRs (Fig. 6), which are uncommon in Seyfert galaxies. This result stresses a fundamental difference in the circumnuclear environment of radio-loud and radio-quiet AGNs, which could be important for the formation and collimation of jets, and which needs to be further explored by future *AXAF* and *XMM* higher-resolution observations. For example, the absorbing medium can have the form of a cold accretion-disk wind, which is invoked in models for jet collimation (e.g., Blandford & Payne 1982; Königl & Kartje 1994). It is interesting to note that radio-loud quasars exhibit narrow UV absorption lines much more frequently than radio-quiet quasars (Foltz et al. 1986; Anderson et al 1987), which may be an additional manifestation of the X-ray absorber.

## 9. Conclusions

We have studied the X-ray spectral properties of a sample of radio-loud AGN observed with *ASCA*. The sample includes 10 BLRGs, 9 NLRGs, 5 QSRs, and 10 RGs observed by *ASCA* up until 1998 September, with enough detected counts to allow spectral analysis.

We find that the soft X-ray emission of about 50% of the sources is dominated by a thermal component, most likely associated to the hot, diffuse gas detected in *ROSAT* images. The temperatures and luminosities determined from the *ASCA* spectra have a bimodal distribution, with some sources being dominated by cluster-type emission while others having parameters typical of loose groups or hot coronae. There is no difference in the temperature and luminosity between clusters hosting radio galaxies and those without, suggesting that the presence of an active nucleus is not closely connected to the larger-scale properties of the environment. Future higher-resolution observations with *AXAF* will elucidate the role of this external gas in confining the radio jets and for fueling the central engine.

At hard X-rays, a power-law component is detected in most sources, including NLRGs and RGs where it is heavily absorbed. The measured 2–10 keV intrinsic luminosities and photon indices have similar distributions in BLRGs, QSRs, and NLRGs, with  $L_{2-10 \text{ keV}} \sim 10^{42-10^{45}} \text{ erg s}^{-1}$  and  $\langle \Gamma_{2-10 \text{ keV}} \rangle = 1.7-1.8$ . This is in agreement with simple orientation-based unification scenarios, which postulate that all subclasses of AGN have fairly similar central engines. The presence of significant amounts of cold gas with column densities  $N_{\text{H}} \sim 10^{21-10^{24}} \text{ cm}^{-2}$  in NLRGs and RGs supports the presence of an obscuring torus in these objects. However, significant excess column densities are also detected in a fraction of BLRGs (4/9, or 44%) and QSRs (3/5, or 60%), in contrast to Seyfert 1 galaxies. Another pronounced difference between BLRGs and QSRs and their radio-quiet counterparts is the absence of warm absorbers in the radio-loud objects. In particular, absorption edges from highly-ionized species, a hallmark of the X-ray spectra of Seyfert 1s, are detected in only one BLRG with a column density that falls at the lower end of the distribution among Seyferts of similar intrinsic luminosity. These observational results suggest a systematic difference in the conditions in the gas surrounding the X-ray source in radio-loud and radio-quiet AGN, that needs to be studied with future higher-resolution observations.

The X-ray luminosity of the power-law spectral component is primarily correlated with the luminosity of the [O III] emission line, in a linear way for the sub-sample of BLRGs and QSRs ( $L_{[\text{O III}]} \propto L_{2-10 \text{ keV}}^{1.05}$ ); the relationship steepens when NLRGs and RGs are added ( $L_{[\text{O III}]} \propto L_{2-10 \text{ keV}}^{1.23}$ ). The X-ray nuclear luminosity is also primarily correlated with the FIR power at 12  $\mu\text{m}$  ( $L_{12 \mu\text{m}} \propto L_{2-10 \text{ keV}}^{0.83}$ ), and with the lobe radio power ( $L_{\text{lobe}} \propto L_{2-10 \text{ keV}}^{0.92}$ ), indicating that the same basic physical process is responsible for turning on the nucleus and feeding the distant radio lobes.

The Fe K $\alpha$  line is detected in 50% BLRGs and 20% QSRs with a large dispersion of EWs and velocity widths. The line is generally broad with  $FWHM \gtrsim 20,000 \text{ km s}^{-1}$ . In the few NLRGs and RGs where the line is detected, it is narrow and unresolved, with EWs consistent with an origin through fluorescence in cold material, such as an obscuring torus.

Particularly intriguing is the detection in hard X-rays of the subclass of WLRGs. The *ASCA* spectra of 5/6 WLRGs in our sample are decomposed into a hard power law with  $\langle \Gamma \rangle = 1.5$  (with individual slopes as flat as  $\Gamma = 1.3$ ) and  $L_{2-10 \text{ keV}} \sim 10^{40-10^{42}} \text{ erg s}^{-1}$  and a Raymond-Smith thermal plasma model with  $kT \sim 1 \text{ keV}$ . Based on their optical and X-ray properties, WLRGs could be the radio-loud counterparts of LINERs, although with considerably flattened hard X-ray spectra. If a low-luminosity AGN is present in WLRGs (which seems to be the case in most of the sources discussed here), we suggest that the latter is fuelled at a rate well below the Eddington rate. Starburst activity could also be present at soft X-rays, and, viewed from this perspective, the true nature of some WLRGs may be different to ascertain, as for LINERs. Future *AXAF* and *XMM* observations may clarify the picture.

We compared the X-ray spectral slopes of radio-loud AGN to those of their radio-quiet counterparts in matched ranges of intrinsic luminosity. We find only weak indication (94% confidence)

that BLRGs have flatter X-ray spectra than Seyfert 1s by  $\Delta\Gamma \sim 0.3$ , while the slopes of the remaining subclasses (NLRGs/Seyfert 2s, QSRs/QSOs) are not demonstrably different. This shows that the X-ray continuum slopes of radio-loud and radio-quiet AGN are intrinsically similar, confirming that a beamed component from the inner regions of a relativistic jet is responsible for the flatter slopes observed in radio-loud sources in previous works.

RMS acknowledges support from NASA contract NAS-38252 and from an NRC Fellowship at the Laboratory for High Energy Astrophysics at Goddard where this research was started. During the early parts of this work, ME was based at the University of California, Berkeley, and was supported by a Hubble Fellowship (grant HF-01068.01-94A from the Space Telescope Science Institute, which is operated for NASA by the Association of Universities for Research in Astronomy, Inc., under contract NAS 5-26255). We are grateful to Michael Akritas for kindly sharing his code for partial correlation analysis of censored data, and Eric Feigelson for interesting conversations about astrostatistics. We also thank Tahir Yaqoob for all his help with several questions about the *ASCA* data analysis. The referee, Belinda Wilkes, provided constructive criticism and many comments which improved the presentation of the paper. This research made use of the *ASCA* data archive at HEASARC, Goddard Space Flight Center, and of the NASA/IPAC Extragalactic Database (NED) which is operated by the Jet Propulsion Laboratory, California Institute of Technology, under contract with the National Aeronautics and Space Administration.



### Appendix: Comments on individual sources

**3C 111:** The *ASCA* data were previously studied by Reynolds et al. (1998). Our results are in agreement with theirs. In particular, we confirm the detection of the Fe line ( $\Delta\chi^2=10.6$  over the single absorbed power law for 3 additional parameters) with an EW  $\sim 100$  eV. We fixed the line energy and width in Table 4 to their best-fitting values ( $E=6.4$  keV,  $\sigma = 0.50$  keV) to derive a better estimate of the EW. Because the source is located behind a dark molecular clouds in the Galaxy (Bania et al. 1991), it is unclear whether the excess X-ray absorption detected with *ASCA* is local or intrinsic to the source (see discussion by Reynolds et al. 1998). No ionized absorption is detected, with a 90% confidence upper limit to the O VII K-edge of  $\tau_e < 1.0$ .

**3C 120:** Our results for the continuum are in full agreement with previous analysis by Grandi et al. (1997). Our best-fitting model for the Fe line, however, gives a larger width and EW than found by those authors ( $\sigma = 0.89^{+0.17}_{-0.15}$  keV, EW= $509^{+67}_{-85}$  eV), with larger uncertainties on the fitted parameters. A possible cause of the discrepancy is that we used the SIS data in BRIGHT2 mode, while Grandi et al. (1997) used the data in BRIGHT mode, and fixed the continuum slope during the fits. There is no evidence for a warm absorber; the optical depth of the O VII K-edge is unconstrained in the fit.

**Pictor A:** The *ASCA* data were analyzed by Eracleous & Halpern (1998). Our results are in full agreement with theirs. The *ASCA* column density,  $N_H \sim 8 \times 10^{20}$  cm $^{-2}$ , and photon index,  $\Gamma \sim 1.8$ , are completely consistent with previous measurements with *EXOSAT* in a slightly higher ( $F_{2-10 \text{ keV}} \sim 1.7 \times 10^{-11}$  erg cm $^{-2}$  s $^{-1}$ ) intensity state (Singh, Rao, & Vahia 1990). The latter authors also report the detection of an Fe emission line between 6 and 8 keV with a large EW  $\sim 1.3$  keV, which is not confirmed with *ASCA*. Recent *SAX* observations of Pictor A showed a thermal-plasma component with  $kT \sim 0.6$  keV at low energies, contributing  $\sim 5\%$  of the power law flux at 0.1–2.4 keV (Padovani et al. 1999). Adding a thermal component to the *ASCA* data (both fixing the  $N_H$  and leaving it free) does not lead to an improved fit ( $\Delta\chi^2=2$  for 3 additional parameters). We do not detect absorption edges, with an (interesting) 90% confidence upper limit to the optical depth of the K-edge of O VII of  $\tau_e < 0.09$ .

**3C 303:** The best-fitting model for the *ASCA* continuum is a power law absorbed by a column of cold gas in excess to the Galactic value. A formally equivalent fit is obtained with a power law, absorbed by the Galactic column of cold gas, plus an absorption edge, with the following parameters:  $\Gamma = 1.85^{+0.08}_{-0.04}$ , edge rest-frame energy  $E_e = 0.685^{+0.051}_{-0.373}$  keV and optical depth  $\tau = 0.98^{+9.02}_{-0.34}$ ,  $\chi_r^2/dof_s=1.01/365$ . The edge energy falls well below the SIS sensitivity cutoff, suggesting that the edge model is only a parameterization of excess cold absorption. A *ROSAT* spectrum from the all-sky survey ( $\sim 500$  counts) is fitted with a single power law with  $\Gamma = 2.07 \pm 0.56$  and  $N_H = 2.6 \pm 1.6$  cm $^{-2}$ , consistent with Galactic (Almudena Prieto 1996); however, the fit is not acceptable ( $\chi_r^2/dof_s=1.49/26$ ). Future broader-band observations of 3C 303 are necessary to better study the low-energy absorption in this BLRG. The only previous pointed X-ray observations of 3C 303 were performed with the *Einstein* IPC, which measured a flux in 0.5–3 keV of  $F_{0.5-3 \text{ keV}} \sim 1.2 \times 10^{-12}$

erg cm<sup>-2</sup> s<sup>-1</sup> (Fabbiano et al. 1984), similar to *ASCA*, but no spectral information is reported.

**3C 382:** The *ASCA* data were previously analyzed by Reynolds (1997) and Woźniak et al. (1998). The *ASCA* continuum was modelled in different ways, which resulted in different constraints on the Fe line profile. Reynolds (1997) fits the *ASCA* continuum with a single power law with photon index  $\Gamma \sim 1.9$  plus two absorption edges at  $\sim 0.6$  and  $0.7$  keV (representing O VII and O VIII) with optical depths  $\tau \sim 0.2$ . He finds a strong (EW  $\sim 1$  keV) and broad ( $\sigma \sim 2$  keV) Fe K $\alpha$  line. Woźniak et al. (1998) parameterize the continuum in terms of a broken power law model with a break at 4 keV and  $\Gamma_{\text{hard}} \sim 1.7$ ,  $\Gamma_{\text{soft}} \sim 2$ , and find a very weak (EW  $\sim 27$  eV) and unresolved ( $\sigma \equiv 0$  keV) Fe line. We fit the *ASCA* continuum with a single power law ( $\Gamma \sim 1.2$ ) plus a soft excess described by a thermal bremsstrahlung ( $kT \sim 2$  keV), and find a moderately strong (EW  $\sim 760$  eV) and broad ( $\sigma \sim 1.4$  keV) Fe line (see Tables 3 and 4). This illustrates the difficulty of modeling the Fe line in the relatively narrow *ASCA* band. In support of our parameterization of the data, we note that a soft excess in 3C 382 at energies  $\lesssim 2$  keV was found in previous *EXOSAT* (Barr & Giommi 1992) and *GINGA* (Kaastra, Kunieda, & Awaki 1991) observations. The flat continuum slope is not unprecedented: depending on the parameterization of the soft excess the range of photon indices measured from the *GINGA* spectrum is 1.03–1.51. The power law slope also appears to vary significantly on timescales of days to years with the X-ray flux (Barr & Giommi 1992; Kaastra et al. 1991). The *ASCA* observations correspond to an intermediate state. In this model, the 90% confidence upper limit to the K-edge of O VII is  $\tau_e < 0.2$ .

**3C 390.3:** The *ASCA* observations of this BLRG were previously analyzed by Eracleous et al. (1995) and Leighly et al. (1997). Eracleous et al. fit the 1993 data with an absorbed power law plus reflection plus an Fe line; our results for the column density, photon index, and line parameters are completely consistent with those of Eracleous et al., who fixed the reflection strength to 0.5. This value is consistent with the one we find when this parameter is left free to vary (Table 3). We also report the first detection of a significant ( $\Delta\chi^2=17$  for 2 additional degrees of freedom) absorption edge at a rest-energy  $E_e \sim 0.78$  keV with  $\tau \sim 0.3$ ; if the feature is identified with the absorption edge of O VII ( $E = 0.739$  eV), a column density of  $N_{\text{H,warm}} \sim 8 \times 10^{20}$  cm<sup>-2</sup> is implied for the ionized gas, similar to the column density of cold gas. We also find that the Fe K $\alpha$  line profile is better described by a disk-line model than by a symmetric Gaussian (§4.3); the disk-line model fitted parameters are  $E_{\text{rest}} = 6.43 \pm 0.06$  keV,  $\text{EW} = 132_{-48}^{+40}$  eV, inclination  $i \sim 33^\circ$  (pegged at the radio upper limit),  $\chi^2_{\text{r}}/\text{dof} = 1.03/1158$ . Our results for the remaining 1995 *ASCA* observations of 3C 390.3 are consistent with Leighly et al. (1997). 3C 390.3 was recently observed with *SAX* in 0.1–100 keV (Grandi et al. 1999). The *SAX* data are consistent with a  $\Gamma \sim 1.8$  powerlaw continuum, plus a reflection component with strength  $R \equiv N_{\text{refl}}/N_{\text{plaw}} \sim 1$ , plus a narrow ( $\sigma \sim 73$  eV) Fe line with EW  $\sim 140$  eV. At soft X-rays, the *SAX* spectrum is consistent with cold absorption in excess to Galactic,  $N_{\text{H}} \sim 10^{21}$  cm<sup>-2</sup> (Grandi et al. 1999). The latter authors also point out a historical variability of the column density of cold gas, without an apparent correlation with the nuclear X-ray luminosity. No absorption edges are reported from the *SAX* data; however, the lower sensitivity and reduced observing efficiency of the LECS makes it difficult to observe weak edges

such as detected with *ASCA* in 3C 390.3.

**3C 445:** The *ASCA* observation of 3C 445 was previously published by Sambruna et al. (1998), with fully consistent results. The 90% confidence upper limit to the K-edge of O VII is  $\tau_e < 0.6$ . The 0.6–10 keV *ASCA* spectrum is consistent with a dual absorber (Table 3), which also fits the combined *ROSAT* plus *ASCA* data well. Interestingly, 3C 445 is the only source among the X-ray absorber BLRGs and QSRs of our sample to exhibit soft X-ray emission above the extrapolation of the hard, absorbed power law (cfr. the best-fit model in Figure 1). This indicates the presence of reprocessed radiation at soft X-rays, of which the dual absorber is a possible parameterization. In this respect, the X-ray spectrum of 3C 445 is similar to the Seyfert 2 NGC 6552 (Fukazawa et al. 1994), where the “soft X-ray excess” was resolved into a blend of several emission lines in a long (350 ks) serendipitous *ASCA* exposure. The lines were interpreted as due to emission from neutral elements such as O, Ne, and Mg (Reynolds et al. 1994). The large inclinations of 3C 445 ( $i \gtrsim 60$  deg; Eracleous & Halpern 1998) makes it conceivable that we are intercepting the reprocessed radiation from the absorber, diluted by the primary direct emission. We thus reanalyzed the combined *ROSAT* and *ASCA* SIS data of 3C 445 to constrain the strength of possible soft X-ray lines. We fitted the data with a simple continuum model including a heavily absorbed ( $N_H = (3 \pm 1) \times 10^{23}$  cm $^{-2}$ ) power law with  $\Gamma \sim 1$  at energies  $\gtrsim 2$  keV, plus a power law with the same slope and Galactic  $N_H$  only at softer energies. We added narrow ( $\sigma = 0$  keV) Gaussians with energies fixed at the redshifted energies of neutral abundant elements in the range 0.6–2 keV, following the model of Reynolds et al. (1994) for NGC 6552. We find marginal ( $\gtrsim 90\%$  confidence) detections in the case of OI (0.56 keV), with  $EW=140_{-124}^{+100}$  eV, and Mg(1.26 keV), with  $EW=45_{-43}^{+48}$  eV. In addition, we significantly detect ( $\Delta\chi^2 = 10.8$  for 3 additional parameters,  $P_F \gtrsim 95\%$ ) an emission line at 2.76 keV with  $EW=280 \pm 121$  eV, which we tentatively identify as the Si recombination continuum line. These results support the idea that significant soft X-ray reprocessing is present in 3C 445 from the gas responsible for the observed X-ray absorption. High-resolution X-ray observations of 3C 445 at both soft and medium-hard energies (e.g., with *XMM*) will constrain the physical and dynamical state of the absorber(s) in this source, and its location.

**PKS 2251+113:** The *ASCA* data were independently analyzed by Brandt, Laor, & Wills (1999); our results agree with theirs. In particular, large excess X-ray absorption of  $N_H \sim 1 \times 10^{22}$  cm $^{-2}$  in the quasar’s rest-frame is measured with *ASCA*. This quasar also exhibits intrinsic UV absorption; possible association of the UV and X-ray absorbers and the implications for the spectral energy distribution is discussed by Brandt et al. (1999).

**PKS 0634–20:** A partial covering model describes best the (low signal-to-noise ratio) *ASCA* spectrum of this NLRG. The measured column density from the X-rays,  $N_H \sim 8 \times 10^{23}$  cm $^{-2}$ , is one order of magnitude larger than the extinction inferred from IR observations of the continuum (Simpson, Ward, & Wilson 1995),  $N_H \sim 7 \times 10^{22}$  cm $^{-2}$ , assuming a Galactic gas-to-dust ratio. The continuum X-ray slope,  $\Gamma \sim 1.9$ , and the 2–10 keV intrinsic luminosity,  $L_{2-10 \text{ keV}} \sim 3 \times 10^{43}$  erg s $^{-1}$ , point to the presence of an AGN. Thus, we confirm the suggestion by Simpson et al. (1995) that an active nucleus is present in PKS 0634–205, buried under several magnitudes of visual extinction.

The *ASCA* data also suggest that  $\sim 4\%$  of the primary nuclear emission is scattered into the line of sight at soft X-rays, consistent with the presence of dust/hot electrons around the active nucleus, as suggested by Simpson et al. (1995).

**4C +55.16:** The X-ray emission of this radio galaxy is dominated by diffuse cluster emission. There is a report of a cooling flow and lensing effects (Iwasawa et al. 1999a).

**3C 219:** A broad component of the Pa $\alpha$  line was detected in the IR observations of Hill et al. (1996), showing the presence of a hidden broad-line region in this NLRG. The amount of reddening inferred for the broad-line region is  $A_V \sim 1.8$ , implying a column density of  $4 \times 10^{21} \text{ cm}^{-2}$  for a Galactic gas-to-dust ratio. The *ASCA* data on 3C 219 confirm the presence of a hidden AGN: the hard X-ray spectrum is described by a heavily-absorbed power law with  $\Gamma \sim 1.7 - 1.8$  and  $N_H \sim 2 \times 10^{21} \text{ cm}^{-2}$ . There is little or no flux and spectral variability between the two *ASCA* observations. Our results for the second observation are consistent with the results reported by Brunetti et al. (1999). A thermal contribution by the host galaxy to the observed soft X-ray spectrum is also detected in the first observation, when the emission from the nucleus was slightly lower (factor 1.3) than during the second exposure.

**3C 295:** This NLRG at  $z=0.51$  resides in an optical cluster of galaxies, whose X-ray emission completely dominates the *ASCA* data: no point-like source is detected with *ASCA*. This confirms previous X-ray observations with the *Einstein* IPC and HRI (Henry & Henriksen 1986), which indicated the presence of a massive ( $\sim 145 M_\odot \text{ yr}^{-1}$ ) cooling flow, with loose constraints on the X-ray temperature of the cluster ( $kT \sim 3-10 \text{ keV}$ ). The gas parameters measured with *ASCA* are a temperature  $kT \sim 6 \text{ keV}$ , a metallicity  $Y \sim 0.5$ , and a 2–10 keV luminosity  $L_{2-10 \text{ keV}} \sim 6 \times 10^{44} \text{ erg s}^{-1}$  (Table 3).

**3C 313:** This FR II radio galaxy resides in a rich optical environment (Hill & Lilly 1991). However, the *ASCA* spectrum is consistent with a power law absorbed by a Galactic column of cold gas (Table 3). Fitting the spectrum with a Raymond-Smith model also leads to an acceptable fit,  $\chi_r^2/dof=0.91/80$ ; however, this is worse by  $\Delta\chi^2 = 4$  than the power-law model which has the same number of parameters. The fitted parameters of the thermal model are: temperature  $kT = 9(> 3) \text{ keV}$  and 0.1–2.4 keV intrinsic luminosity  $L_{0.1-2.4 \text{ keV}} \sim 4 \times 10^{43} \text{ erg s}^{-1}$  (for  $Y \equiv 1$ ), one order of magnitude lower than predicted from the  $L-T$  relationship for clusters (Figure 4; Markevitch 1998), although the uncertainties on the temperature are large. If the abundance  $Y$  is left free to vary, we obtain  $kT \sim 10 \text{ keV}$  and  $Y \sim 0.06$ , thus effectively mimicking a power law. We conclude that, unless the optical cluster around 3C 313 has very unusual X-ray properties, the X-ray emission of this radio galaxy in the *ASCA* band is dominated by the non-thermal radio source. Note, however, that some excess flux is present in the residuals of the single power-law model around 0.9 keV (Figure 1), which may suggest the presence of a thermal contribution. Adding a Raymond-Smith model to the power law decreases  $\chi^2$  by  $\Delta\chi^2 \sim 4$  only, not significant for 2 additional parameters according to the F-test. The upper limit on the thermal component luminosity in this case is  $L_{0.5-2 \text{ keV}} \lesssim 3 \times 10^{43} \text{ erg s}^{-1}$  (for  $kT \sim 2 \text{ keV}$  and  $Y \equiv 1$ ).

**3C 321:** This FR II radio galaxy has a double nucleus (separation 4 arcsec) and large-scale diffuse structures suggestive of a recent merger (Young et al. 1996 and references therein). UV spectropolarimetric observations show the presence of three distinct emission components contributing to the UV: the host galaxy, a hidden AGN whose emission is scattered into the line of sight (20-70% of the total continuum), and a young starburst (Tadhunter, Dickson, & Shaw 1996). The presence of a hidden AGN is also confirmed by the detection of a broad H $\alpha$  component in polarized optical light (Young et al. 1996). In X-rays, 3C 321 is detected with *ASCA* with a poor signal-to-noise ratio (Table 2). The SIS images show an extended ( $\sim 2$  arcmin) asymmetric structure, while a point-like source is present at hard energies in the GIS data. Modelling of the spectrum is hampered by the poor signal-to-noise ratio and the following results must be taken with caution. At energies below 1 keV, the *ASCA* spectrum is consistent with a Raymond-Smith plasma model with  $kT \sim 0.6$  keV (Table 3). The intrinsic 0.5–4.5 keV luminosity of the thermal component is  $L_{X,\text{obs}} \sim 6 \times 10^{41}$  erg s $^{-1}$ . This value is close to the predicted X-ray luminosity of the starburst,  $L_{X,\text{starb}} \lesssim 4 \times 10^{41}$  erg s $^{-1}$  (using equations (1) and (2) of David, Jones, & Forman 1992, and the IRAS fluxes at 60  $\mu\text{m}$  and 100  $\mu\text{m}$ ). While *ASCA* provides initial evidence for the presence of a starburst in 3C 321, future higher resolution observations with *AXAF* are needed to confirm this suggestion. Above 3 keV, the *ASCA* spectrum of 3C 321 is best described by an absorbed power law with  $N_{\text{H}} \sim 10^{22}$  cm $^{-2}$  and  $\Gamma \sim 1.5$ . There is some evidence in SIS0, SIS1, and GIS3 for a narrow unresolved Fe K $\alpha$  line with EW  $\sim 1.8$  keV (Table 4). This feature persists even when different extraction cells for the background are used. Moreover, several “line-like features” are present between 0.9–3 keV at 1–2 $\sigma$  level; if real, these features could be similar to those detected in the *ASCA* data of a few Seyfert 2s (Ueno et al. 1994a; Iwasawa et al. 1994; Turner et al. 1997a) and expected on theoretical grounds in scattering-dominated AGN. It will be important to observe 3C 321 with future high-resolution X-ray observatories to obtain a high-quality spectrum and confirm the marginal features in the *ASCA* data.

**Cygnus A:** The X-ray emission from this galaxy is complex, including contributions from the intracluster gas emission and a cooling flow at lower energies (Arnaud 1996; Reynolds & Fabian 1996). Previous observations with *EXOSAT* and *GINGA* detected a power-law spectral component at hard X-rays (Arnaud et al. 1987; Ueno et al. 1994b), attributed to a hidden AGN. These claims are also confirmed by recent optical spectropolarimetry, which led to the detection of a broad H $\alpha$  emission line in polarized light (Ogle et al. 1997). In order to avoid the contribution of the cooling flow and concentrate on the AGN component, we restricted our analysis to the energy range 4–10 keV, while allowing a thermal component to include the cluster emission. The power-law photon index and absorption column density measured with *ASCA* are  $\Gamma \sim 1.8$  and  $N_{\text{H}} \sim 1 - 2 \times 10^{23}$  cm $^{-2}$  (Table 3), in good agreement with the previous *EXOSAT* and *GINGA* results. With *ASCA* we also detect for the first time the Fe K $\alpha$  line at  $\sim 6.4$  keV. Constraining the line to be narrow, we measure an EW  $\sim 100$  eV (Table 4), consistent with an origin by fluorescence in cold gas. However, a marginally improved fit is obtained if the line is allowed to be broad ( $\Delta\chi^2=4.7$ , significant at  $P_{\text{F}} \gtrsim 95\%$  confidence for 1 additional parameter), with  $\sigma_{\text{rest}} = 0.36^{+0.24}_{-0.11}$  keV and EW=208 $^{+140}_{-106}$  eV. Because of the spectral complexity in the energy range 5–7 keV, where contributions from the gas

cluster are present, we regard this result as preliminary and quote only the results for a narrow line in Table 4. While the Fe line detection provides further unambiguous proof of the presence of an AGN in the central regions of Cygnus A, under a heavy layer of cold gas, future higher-resolution X-ray observations are needed to study the line profile in more detail.

**PKS 2152–69:** This NLRG has an intermediate FR I/II radio morphology. It is famous for exhibiting a cloud of highly ionized gas at  $\sim 10$  arcsec from the nucleus, also emitting a blue continuum (Tadhunter et al. 1988), which is either photoionized by a beamed radiation from the nucleus (di Serego Alighieri et al. 1988), or by shocks induced by jet/cloud interactions (Fosbury et al. 1998). The *ASCA* data of PKS 2152–69 are consistent at hard energies with an absorbed power law with  $\Gamma \sim 1.9$ , typical of the other NLRGs in the sample, and with relatively lower luminosity,  $L_{2-10 \text{ keV}} \sim 6 \times 10^{42} \text{ erg s}^{-1}$ . The presence of an Fe line is difficult to assess because of the thermal contribution in the range 6–7 keV (Figure 1). At soft energies, a thermal-plasma component is the best description of the *ASCA* spectrum, with luminosity and temperature typical of a poor group of galaxies or the corona of the elliptical host galaxy as detected in the optical (Tadhunter et al. 1988). An archival *ROSAT* HRI exposure shows that the soft X-ray emission is extended up to 1 arcmin around the optical body of the galaxy (E. Colbert 1999, priv. comm.), confirming the *ASCA* result.

**3C 109:** The *ASCA* spectrum of the QSR 3C 109 is best fitted by an absorbed power law with  $N_{\text{H}} \sim 5 \times 10^{21} \text{ cm}^{-2}$  and  $\Gamma \sim 1.7$  (Table 3). These values are consistent with those previously published by Allen et al. (1997) and with a previous *ROSAT* observation (Allen & Fabian 1992). The presence of intrinsic absorption in 3C 109 is also supported by optical observations, which show a highly polarized continuum and reddened Balmer lines (Goodrich & Cohen 1992), suggestive of a dust screen covering the active nucleus. 3C 109 also exhibits an unusually red IR-to-optical continuum (Elvis et al. 1984). The detection of an Fe  $K\alpha$  line in the *ASCA* data, with  $\text{EW} \sim 300$  eV, was previously reported by Allen et al. (1997). However, we do not confirm this result: we find that the addition of a line to the GIS spectrum, with  $\text{EW} \sim 200$  eV and width  $\sigma \sim 0.7$  keV, improves the fit by  $\Delta\chi^2=5$ , not significant for 3 additional parameters according to the F-test. The SIS data give only an upper limit of  $\text{EW}=60$  eV (for an unresolved line) and of 170 eV (for a broad line). More sensitive observations, e.g., with *XMM*, are necessary to confirm the Fe line detection in 3C 109.

**3C 234:** This classical triple radio galaxy has been extensively studied at optical and IR wavelengths. We classify it as a QSR following Grandi & Osterbrock (1978) who detected a highly-luminous broad line. Recent optical studies have shown that the nuclear continuum and broad  $\text{H}\alpha$  line are highly polarized ( $\sim 25\%$ ), with a position angle perpendicular to the radio axis (Antonucci 1984; Tran, Cohen, & Goodrich 1995; Young et al. 1998). This was interpreted in terms of scattering into the line of sight by a population of hot electrons or dust, the latter also advocated to explain the steep IR-to-optical continuum (Elvis et al. 1984). The *ASCA* X-ray spectrum of 3C 234 has a low signal-to-noise ratio, allowing us to draw only limited conclusions. The 0.6–10 keV continuum is best described by a partial covering model, where a large fraction ( $\sim 67\%$ ) of the

primary X-ray emission is scattered/transmitted into the line of sight. The photon index is unusually low,  $\Gamma \sim 0.08$ , supporting a scattering origin of the radiation in the *ASCA* band (as in Seyfert 2s; Turner et al. 1997a). It is thus possible that the primary X-rays are blocked up to 10 keV by a very large ( $\gtrsim 10^{24} \text{ cm}^{-2}$ ) column density (by analogy with the Seyfert 2 galaxy NGC 1068). At low energies, the *ASCA* spectrum can be described by a Raymond-Smith thermal plasma model. The temperature and luminosity of this component suggest an origin in the ISM of the host galaxy. However, another possibility is that this component consists of a blend of soft X-ray lines around 1 keV, which would be expected in scattering-dominated AGN on both observational and theoretical grounds (Ueno et al. 1994a; Iwasawa et al. 1994; Netzer, Turner, & George 1998).

**3C 254:** Extended soft X-ray emission associated to the optical cluster of galaxies was recently detected for this QSR in a 30 ks ROSAT HRI exposure (Crawford et al. 1999), contributing  $\lesssim 20\%$  of the total X-ray luminosity of the source. The *ASCA* data are well fitted by a single power law with  $\Gamma \sim 1.7$  (Table 3) absorbed by Galactic  $N_{\text{H}}$  only; addition of a Raymond-Smith thermal model yields a decrease of the  $\chi^2$  of 4, not significant for 3 additional parameters. The upper limit to the 0.1–2.4 keV luminosity of the extended component is  $L_{0.1-2.4 \text{ keV}} \lesssim 1 \times 10^{45} \text{ erg s}^{-1}$ , in very good agreement with the measured luminosity from the ROSAT data (Crawford et al. 1999).

**4C +74.26:** This QSR is associated with a giant double-lobed radio source. Its *ASCA* spectrum was previously published by Brinkmann et al. (1998), together with optical and radio data. These authors fitted the *ASCA* spectrum with a complex model, including a power law ( $\Gamma \sim 2.03$ ), cold reflection (with strength  $R \equiv N_{\text{ref}}/N_{\text{pl}} \sim 6$ ), an Fe  $K\alpha$  line ( $\sigma \sim 0.08 \text{ keV}$ ,  $\text{EW} \sim 100 \text{ eV}$ ), and a warm absorber at low energies. We find that the 0.6–10 keV continuum of 4C +74.26 is concave. When we fit it with a power law plus reflection model, we recover a similar solution to Brinkmann et al. However, the Fe line is no longer significantly detected in our solution, which is in striking contrast with the strength of the reflected component. In fact, for  $R \sim 6$ , the expected EW of the Fe  $K\alpha$  line is  $\gtrsim 400 \text{ eV}$  assuming  $i \lesssim 49^\circ$  (from the radio morphology, Brinkmann et al. 1998) and  $\Gamma = 2.1$  (George & Fabian 1991). We suggest that the concavity of the X-ray continuum is related to the presence of a hard tail, possibly associated with the radio jet. Fitting the spectrum with a double power law model, we obtain  $\Gamma_{\text{soft}} \sim 2$ ,  $\Gamma_{\text{hard}} \sim 0.2$ . With this continuum model, the Fe line is broad ( $\sigma \sim 0.6 \text{ keV}$ ) with  $\text{EW} \sim 215 \text{ eV}$ . We do not find evidence for ionized absorption at low energies, where a cold absorber is sufficient to fit adequately the *ASCA* and the archival *ROSAT* data. We are only able to set an upper limit to the optical depth of the O VII edge of  $\tau_e = 0.8$  (at 99% confidence).

**3C 28:** This radio galaxy is the dominant member of the distant ( $z = 0.195$ ) Abell cluster A115. Previous X-ray observations with the *Einstein* HRI are entirely consistent with diffuse emission centered on the optical galaxy and extending in a direction roughly orthogonal to the radio structure (Feretti et al. 1984). The authors interpret this component, which has a luminosity  $L_{\text{X}} \sim 5 \times 10^{43} \text{ erg s}^{-1}$  ( $\pm 30\%$ ), as a cooling flow onto the central regions of the galaxy. The *ASCA* spectrum is best described by a thermal plasma model representing the emission from A115 ( $kT \sim 3.3 \text{ keV}$ , metallicity  $Y \sim 0.3$ ), plus a hard, absorbed power-law component ( $N_{\text{H}} \sim 2 \times 10^{21} \text{ cm}^{-2}$ ,  $\Gamma \sim 1.5$ ),

which could be associated with a hidden AGN. The hard tail is clearly detected in the SIS0+SIS1 spectra ( $\Delta\chi^2=12.5$  for 2 additional parameters,  $P_F \gtrsim 99\%$ ) but only marginally detected in the GIS2+GIS3 spectra ( $\Delta\chi^2=7$ ,  $P_F \sim 95\%$ ). Since the hard tail dominates the emission above  $\sim 5$  keV, we examined the 5–10 keV SIS and GIS images. The presence of a point-source was not obvious. In addition, only an upper limit is given in the literature for the radio core emission and for the [O III] emission line (Table 1). We thus regard the detection of the hard tail in the *ASCA* data and its interpretation as due to an active nucleus as tentative. More sensitive observations at hard X-rays are necessary to confirm this result.

**PKS 0131–36:** This WLRG lies in an early-type elliptical with a dark lane crossing the main optical body of the host galaxy (Ekers et al. 1978). Strong FIR emission is also detected (Table 1 and references therein). In the radio, PKS 0131–36 exhibits a compact core and two extended lobes, which are weak X-ray sources ( $F_{0.5-10 \text{ keV}} \sim 3 \times 10^{-13} \text{ erg cm}^{-2} \text{ s}^{-1}$ ) in the X-rays (Tashiro et al. 1998), most likely via inverse Compton scattering of the cosmic microwave background photons. The nuclear X-ray emission measured with *ASCA* is complex. At soft X-rays, a thermal component with  $kT \sim 1$  keV is detected; its intrinsic 0.5–4.5 keV luminosity,  $L_{0.5-4.5 \text{ keV}} \sim 9 \times 10^{40} \text{ erg s}^{-1}$ , is compatible with the predicted X-ray luminosity of a starburst (from the FIR fluxes at 60 and 100  $\mu\text{m}$  and eqs. (1) and (2) of David et al. 1992),  $L_{0.5-4.5 \text{ keV}}^{\text{starb}} \sim 1 \times 10^{41} \text{ erg s}^{-1}$ . Thus the *ASCA* data provide evidence for the presence of a starburst in PKS 0131–36, for which a possible location is the dark lane (Brosch 1987). Alternatively, the thermal component may originate in the hot ISM of the host galaxy. A deep (68 ks) archival ROSAT HRI observation shows extended emission centered on the optical body of the galaxy. The hard X-ray spectrum is described by a flat ( $\Gamma \sim 1.3$ ) power law with 2–10 keV luminosity  $L_{2-10 \text{ keV}} \sim 4 \times 10^{42} \text{ erg s}^{-1}$ , heavily absorbed ( $N_{\text{H}} \sim 10^{23} \text{ cm}^{-2}$ ). The residual flux at low energies is consistent with 10% of the nuclear flux being scattered into the line of sight. An Fe line with EW  $\sim 240$  eV is tentatively detected.

**Fornax A:** This nearby radio galaxy, located in the outskirts of the Fornax cluster of galaxies, exhibits extended radio lobes which also emit in the X-rays ( $F_{1 \text{ keV}} \sim 0.2 \mu\text{Jy}$ ) via inverse Compton scattering of the cosmic microwave photons (Feigelson et al. 1995; Kaneda et al. 1995). According to Tadhunter et al. (1998), the nucleus of Fornax A contains a Weak Line Radio Galaxy. The presence of a low-luminosity AGN is also indicated by the LINER-like optical spectrum (Baum et al. 1992). Strong FIR emission is detected from the galaxy (Table 1). The *ASCA* spectrum is described by a soft thermal-plasma model ( $kT \sim 0.8$  keV,  $Y \sim 0.1$ ), most likely due to the cluster. The FIR colors of Fornax A, however, suggest that a starburst could be present (Figure 5). The 0.5–4.5 keV luminosity of the thermal component is  $L_{0.5-4.5 \text{ keV}} \sim 9 \times 10^{40} \text{ erg s}^{-1}$ , while the predicted X-ray luminosity of a starburst based on the IRAS flux of Fornax A is  $L_{0.5-4.5 \text{ keV}}^{\text{starb}} \sim 5 \times 10^{39} \text{ erg s}^{-1}$ . Thus it is possible that part of the thermal emission is due to a starburst, which needs to be confirmed with future X-ray observations. At high energies, an absorbed ( $N_{\text{H}} \sim 3.3 \times 10^{22} \text{ cm}^{-2}$ ) power law, with a poorly constrained spectral index, is detected in the spectrum. Fixing the spectral index at  $\Gamma = 1.5$  (the average value for WLRGs), we measure an intrinsic luminosity  $L_{2-10 \text{ keV}} \sim 5 \times 10^{40} \text{ erg s}^{-1}$ . Fornax A was previously observed with *ROSAT* (Kim et al. 1998);



the 0.1–2.4 keV range is dominated by the extended thermal component. The *ASCA* data were previously published by Iyomoto et al. (1998); while our results for the thermal component agree with those of the latter authors, we can not compare directly our findings for the power law component since Iyomoto et al. (1998) fixed the absorption to Galactic and derive the photon index ( $\Gamma = 1.1 \pm 0.5$ ), while we left  $N_H$  free and fixed the slope. However, the power law luminosity in both cases agree well. Comparing the *ASCA* results to previous observations, Iyomoto et al. (1998) conclude that the nucleus of Fornax A has been inactive for the last 0.1 Gyr.

**IC 310:** This head-tail radio galaxy is one of the dominant members of the Perseus cluster. The optical spectrum is characterized by strong  $H\alpha$ ,  $[N\ II]$ , and  $[S\ II]$  emission lines, with  $L_{H\alpha+[N\ II]} \sim 1.6 \times 10^{40}$  erg s $^{-1}$  (Owen et al. 1995). While IC 310 does not meet the selection criteria of our sample (§2) and was not included in any of the statistical tests, its *ASCA* data are presented here for the first time. The *ASCA* observations are consistent with a steep ( $\Gamma \sim 2.3$ ) power law, confirming previous *ROSAT* results (Rhee, Burns, & Kowalski 1994; Edge & Röttgering 1995), plus a thermal component related to the cluster emission, with  $kT \sim 6$  keV,  $Y \sim 0.3$ .

**PKS 0625–53:** This radio galaxy is classified as a WLRG by Tadhunter et al. (1998). The *ASCA* observation shows extended emission, and the spectrum is best fitted with an absorbed Raymond-Smith thermal model with temperature  $kT \sim 6$  keV and metallicity  $Y \sim 0.3$ , typical of cluster emission. There is no evidence for a point source; the upper limit to the 2–10 keV luminosity of a power law component is  $L_{2-10\ keV}^{nucl} \lesssim 4 \times 10^{42}$  erg s $^{-1}$  (assuming  $\Gamma = 1.5$ ).

**4C +41.17:** This high-redshift radio galaxy is a complex system with at least two distinct components showing up in high-resolution *HST* images at rest-frame UV wavelengths (van Breugel et al. 1998 and references therein). Star formation, possibly induced by the interaction of the jet with the ambient gas, is responsible for most of the unpolarized UV continuum emission (Dey et al. 1997). The source was observed with *ASCA* with the SIS in 2CCD mode; a weak extended ( $\sim 7$  arcmin) source is present in the image, with an elongated morphology and at least two distinct peaks. However, the position of both peaks is  $\gtrsim 3.5$  arcmin away from the radio position of 4C +41.17 (from NED), which is much larger than the uncertainties of  $\sim 23$  arcsec expected from the attitude solution. Moreover, the discrepancy remains after the (small: DETX\_off=+0.1 mm, DETY\_off=-0.66 mm) correction for incorrect star-tracker reading which affects these data is applied (<http://heasarc.gsfc.nasa.gov/docs/asca/coord/updatecoord.html>). We conclude that the association of the X-ray emission detected by *ASCA* to 4C +41.17 is ambiguous. However, no radio or optical counterpart is known in the NED database at the *ASCA* position of either X-ray peak. Integrating over the whole extended X-ray emission yields a total of  $\sim (5 \pm 0.7) \times 10^{-3}$  count s $^{-1}$  both for SIS0 and GIS2. The spectrum can be described by a single power law with  $\Gamma = 1.97 \pm 0.33$  and Galactic  $N_H = 1.2 \times 10^{21}$ , flux  $F_{2-10\ keV} \sim 2 \times 10^{-13}$  erg cm $^{-2}$  s $^{-1}$ .

**3C 270:** This radio galaxy, hosted by the nearby giant elliptical NGC 4261, is classified as a WLRG by Tadhunter et al. (1998). Its central regions were mapped in IR and optical with *HST* (Ferrarese et al. 1996). The high-resolution *HST* images show that the galaxy hosts a small nuclear

disk of dust which is displaced from the nucleus; a dynamical estimate of the central mass is also provided,  $(4.9 \pm 1.0) \times 10^8 M_\odot$ . 3C 270 was previously studied in X-rays with the *ROSAT* PSPC. A diffuse thermal component ( $kT \sim 0.6$  keV for a fixed solar metallicity), possibly associated with a cooling flow, plus an unabsorbed power law ( $\Gamma \sim 1.7$ ) component were found to adequately describe the *ROSAT* spectrum (Worrall & Birkinshaw 1994). The *ASCA* spectrum confirms this spectral decomposition and the low X-ray luminosity ( $L_{2-10 \text{ keV}} \sim 9 \times 10^{40}$  erg s $^{-1}$ ) of the power law component. The temperature of the soft component is found to be slightly higher and the metallicities lower than with *ROSAT*. The power-law index measured with *ASCA* is flatter than that measured with *ROSAT*, although the latter has large uncertainties. No excess cold absorption is detected with *ASCA*, in agreement with the *ROSAT* findings (Worrall & Birkinshaw 1994). An Fe line with EW  $\sim 260$  eV is tentatively detected in the *ASCA* data.

**Centaurus A:** The *ASCA* spectrum was modelled following the prescription of Turner et al. (1997b), who jointly analyzed archival *ROSAT* HRI, PSPC, and *ASCA* data (see also Sugizaki et al. 1997). The *ASCA* spectrum can be modelled as a hard power law with  $\Gamma \sim 1.9$  absorbed by three different absorbers of cold gas, plus a steep ( $\Gamma \sim 2.3$ ) power law representing the jet synchrotron contribution, plus two Raymond-Smith components, the softer one related to a starburst (Turner et al. 1997b). As can be seen in Figure 1, there are line-like residuals around 1 and 2 keV, which can be modelled as Gaussians with EW  $\sim 100$  eV or less, and interpreted as the fluorescent lines of Mg, Si, and S (Sugizaki et al. 1997). A strong Fe line is also present at 6.4 keV, with EW  $\sim 140$  eV (Table 4). Since the line is unresolved at 90% confidence,  $\sigma_{rest} \lesssim 0.12$  keV, its width was fixed at  $\sigma_{rest} \equiv 0.05$  keV in the fits to have better constraints on the other line parameters.

**NGC 6251:** This RG was recently observed with the *HST* (Ferrarese & Ford 1999). Its central regions have a complex morphology with a warped disk of dust stretching across the optical body of the galaxy for  $\sim 760$  pc. It appears to harbor a black hole of mass  $(4 - 8) \times 10^8 M_\odot$ . NGC 6251 has a prominent radio jet which emits also at X-ray wavelengths (Mack, Kerp, & Klein 1997). In X-rays, previous observations with the *ROSAT* PSPC show a diffuse thermal component ( $kT \sim 0.5$  keV), possibly associated with a cooling flow powering the central nucleus, and a power law component with  $\Gamma \sim 2$  and little intrinsic absorption,  $N_H \sim 5 \times 10^{20}$  (Birkinshaw & Worrall 1992). The *ASCA* spectrum is best described by a hard ( $\Gamma \sim 1.8$ ) power law absorbed by  $N_H \sim 7.5 \times 10^{21}$  cm $^{-2}$  (with large uncertainties), plus a thermal plasma component with  $kT \sim 1$  keV, harder than measured with the *ROSAT* PSPC. The *ASCA* data were previously analyzed by Turner et al. (1997a), whose continuum model agrees with ours. We confirm the detection of an Fe line with marginal significance ( $\Delta\chi^2 = 6.8$ ,  $P_F \geq 90\%$ ) at a rest-frame energy  $E \sim 6.6$  keV, consistent with emission from highly ionized Fe (Fe xxv), and with EW  $\sim 443$  eV (Table 4).

**3C 353:** The *ASCA* GIS images are dominated by the extended emission of an elongated cluster, with the radio galaxy 3C 353 located at the edge of the structure. The nucleus of 3C 353 contains a WLRG (Tadhunter et al. 1998), and indeed the *ASCA* spectrum above 2 keV is described by a power law, with  $\Gamma \sim 1.9$  and heavy absorption ( $N_H \sim 4 \times 10^{22}$  cm $^{-2}$ ). The soft X-ray spectrum is described by a thermal Raymond-Smith model with  $kT \sim 1.4$  keV and low metallicity, associated

with the cluster. Analysis of the cluster emission at different locations in the *ASCA* image shows variations of the temperature and metallicity with position. A detailed analysis of the cluster emission is beyond the scope of this paper and will be presented by Iwasawa et al. (1999b).

## REFERENCES

- Akritas, M. G. & Siebert, J. 1996, MNRAS, 278, 919
- Allen, S. W., Di Matteo, T., & Fabian, A. C. 1999, MNRAS, *subm.* (astro-ph/9905052)
- Allen, S. W., Fabian, A. C., Idesawa, E., Inoue, H., Kii, T., & Otani, C. 1997, MNRAS, 286, 765
- Allen, S. W. & Fabian, A. C. 1992, MNRAS, 258, 29
- Almudena Prieto, M. 1996, MNRAS, 282, 421
- Anderson, S. F., Weymann, R. J., Foltz, C. B., & Chaffee, F. H. 1987, AJ, 94, 278
- Antonucci, R. R. J. 1984, ApJ, 281, 112
- Antonucci, R., Barvainis, R., & Alloin, D. 1990, ApJ, 353, 416
- Antonucci, R. & Barvainis, R. 1990, ApJ, 363, L17
- Arnaud, K. A., 1996, in *Cygnus A – Study of a Radiogalaxy*, Proc. of the Greenbank Workshop, Greenbank, WV, May 1–4, 1995, eds. C. L. Carilli & D. E. Harris, Cambridge Univ. Press, p.51
- Arnaud, K. A. Johnstone, R. M., Fabian, A. C., Crawford, C. S., Nulsen, P. E. J., Shafer, R. A., & Mushotzky, R. F. 1987, MNRAS, 227, 241
- Bania, T. M., Marscher, A. P., & Barvainis, R. 1991, AJ, 101, 2147
- Barr, P. & Giommi, P. 1992, MNRAS, 255, 495
- Baum, S. A., Heckman, T. M., & van Breugel, W. 1992, ApJ, 389, 208
- Becker, R. H., White, R. L., & Edwards, A. L. 1991, ApJS, 75, 1
- Blandford, R.D. & Begelman, M. C. 1999, MNRAS, 303, L1
- Blandford, R. D. & Payne, 1982, MNRAS, 199, 883
- Blitz, L., Bazell, D., & Désert, F.X. 1990, ApJ, 352, L13
- Birkinshaw, M. & Worrall, D. M. 1992, ApJ, 412, 568
- Brandt, W. N., Laor, A., & Wills, B.J. 1999, ApJ, *subm.*
- Bregman, J. 1998, ApJ, 499, 670
- Bridle, A. H., Hough, D. H., Lonsdale, C. J., Burns, J. O., & Laing, R. A. 1994, AJ, 108, 766
- Brinkmann, W., Otani, C., Wagner, S. J., & Siebert, J. 1998, A&A, 330, 67
- Brinkmann, W., Siebert, J., & Boller, Th. 1994, A&A, 281, 355
- Brighenti, F. & Mathews, W. G. 1997, ApJ, 490, 592
- van Breugel, W. et al. 1998, astro-ph/9809186
- Brosch, N. 1987, MNRAS, 225, 257
- Brunetti, G., Comastri, A., Setti, G., & Feretti, L. 1999, A&A, 342, 57
- Cappi, M., Matsuoka, M., Comastri, A., Brinkmann, W., Elvis, M., Palumbo, G.G.C., & Vignali, C. 1997, ApJ, 478, 492
- Chen, K., & Halpern, J. P. 1989, ApJ, 344, 115
- Condon, J. J., Frayer, D. T., & Broderick, J. J. 1991, AJ, 101, 362
- Corbett, E. A., Robinson, A., Axon, D. J., Young, S., & Hough, J. H. 1998, MNRAS, 296, 721
- Crawford, C. S., Lehmann, I., Fabian, A. C., Bremer, M. N., & Hasinger, G. 1999, MNRAS, *in press* (astro-ph/9904371)
- Crawford, C. S. & Fabian, A. C. 1995, MNRAS, 273, 827
- Danziger, I. J., Goss, W. M., & Frater, R. H. 1978, MNRAS, 184, 341
- David, L. P., Jones, C., & Forman, W. 1992, ApJ, 388, 82
- Désert, F. X., Bazell, D., & Boulanger, F. 1988, ApJ, 334, 815
- Dey, A., van Breugel, W., Vacca, W. D., & Antonucci, R. 1997, ApJ, 490, 698

- Di Matteo, T. & Fabian, A.C. 1997, MNRAS, 286, L50
- van Dokkum, P. G. & Franx, M. 1995, AJ, 110, 2027
- Dotani, T. et al. 1996, *ASCA News* No. 4, 3
- Ekers, R.D., Goss, W. M., Kotanyi, C. G., & Kellern, D. J. 1978, A&A, 69, L21
- Edge, A. C. & Röttgering, H. 1995, MNRAS, 277, 1580
- Elvis, M., Fiore, F., Giommi, P., & Padovani, P. 1998, ApJ, 492, 91
- Elvis, M., Fiore, F., Wilkes, B., McDowell, J., & Bechtold, J. 1994, ApJ, 422, 60
- Elvis, M., Lockman, F. J., & Wilkes, B. J. 1989, AJ, 97, 777
- Elvis, M., Willner, S. P., Fabbiano, G., Carleton, N. P., Lawrence, A., & Ward, M. 1984, ApJ, 280, 574
- Eracleous, M., Sambruna, R. M., & Mushotzky, R. F. 1999, in prep.
- Eracleous, M. & Halpern, J. P. 1998, ApJ, 505, 577
- Eracleous, M., Halpern, J. P., & Livio, M. 1996, ApJ, 459, 89
- Eracleous, M. & Halpern, J. P. 1994, ApJS, 90, 1
- Fabbiano, G. 1996, in *The Physics of LINERs in View of Recent Observations*, ASP Conference Series, vol. 103, eds. M.Eracleous, A.Koratkar, C.Leitherer, & L.Ho, p.56
- Fabbiano, G. 1989, ARA&A, 27, 87
- Fabbiano, G., Gioia, I. M., & Trinchieri, G. 1989, ApJ, 347, 127
- Fabbiano, G., Trinchieri, G., Elvis, M., Miller, L., & Longair, M. 1984, ApJ, 277, 115
- Fabian, A. C., Rees, M. J., Stella, L., & White, N. E. 1989, MNRAS, 238, 729
- Fanaroff, B. L. & Riley, J. M. 1974, MNRAS, 167, P31
- Feigelson, E. D., Laurent-Muehleisen, S. A., Kollgaard, R.I., & Fomalont, E.B. 1995, ApJ, 449, L149
- Feigelson, E. D., Isobe, T., & Kembhavi, A. 1984, AJ, 89, 1464
- Feigelson, E. D. & Berg, C.J. 1983, ApJ, 269, 400
- Feretti, L. Gioia, I. M., Giovannini, G., Gregorini, L., & Padrielli, L. 1984, A&A, 139, 50
- Ferrarese, L. & Ford, H. C. 1999, ApJ, 515, 583
- Ferrarese, L., Ford, H. C., & Jaffe, W. 1996, ApJ, 470, 444
- Filippenko, A. V. 1996, in *The Physics of LINERs in View of Recent Observations*, ASP Conference Series, vol. 103, eds. M.Eracleous, A.Koratkar, C.Leitherer, & L.Ho, p.17
- Fiore, F., Elvis, M., Giommi, P., & Padovani, P. 1998, ApJ, 492, 79
- Fiore, F., Elvis, M., Mathur, S., Wilkes, B.J., & McDowell, J. 1993, ApJ, 415, 129
- Foltz, C. B., Weymann, R. J., Sun, L., Malkan, M. A., & Chaffee, F. H. 1986, ApJ, 307, 504
- Fosbury, R. A. E, Morganti, R., Wilson, W., Ekers, R. D., di Serego Alighieri, S., & Tadhunter, C.N. 1998, MNRAS, 296, 701
- Fukazawa, Y. et al. 1994, PASJ, 46, L141
- Gelderman, R. & Whittle, M. 1994, ApJS, 91, 491
- George, I. M. & Fabian, A. C. 1991, MNRAS, 249, 352
- George, I. M., Nandra, K., Fabian, A. C. Turner, T. J. Done, C., & Day, C. S. R. 1993, MNRAS, 260, 111
- George, I. M., Turner, T. J., Netzer, H., Nandra, K., Mushotzky, R. F., & Yaqoob, T. 1998, ApJS, 114, 73
- Giovannini, G., Feretti, L., Greogorini, L., & Parma, P. 1988, A&A, 199, 73
- Golombek, D., Miley, G. K., & Neugebauer, G. 1988, AJ, 95, 26
- Goodrich, R. W. & Cohen, M.H. 1992, ApJ, 391, 623
- Goudfroij, P. 1998, A&A, 330, 123

- Grandi, P. et al. 1999, *A&A*, 343, 33
- Grandi, P., Sambruna, R. M., Maraschi, L., Matt, G., Urry, C. M., & Mushotzky, R. F. 1997, *ApJ*, 487, 636
- Grandi, S.A. & Osterbrock, D.E. 1978, *ApJ*, 220, 783
- Guilbert, P. W. & Rees, M.J. 1988, *MNRAS*, 233, 475
- Haardt, F. & Maraschi, L. 1993, *ApJ*, 413, 507
- Halpern, J. P. 1997, in *Mass ejection from Active Galactic Nuclei*, ASP Conference Series, vol. 128, Eds. N.Arav, J.Shlosman, & R.J.Weymann, p. 41
- Heckman, T. M., O’Dea, C.P., Baum, S.A., & Laurikainen, E. 1994, *ApJ*, 428, 65
- Henry, J. P. & Henriksen, M.J. 1986, *ApJ*, 301, 689
- Hes, R., Barthel, P.D., & Hoekstra, H. 1995, *A&A*, 303, 8
- Hill, G. J., Goodrich, R.W., & DePoy, D. L. 1996, *ApJ*, 462, 163
- Hill, G. J. & Lilly, S.J. 1991, *ApJ*, 367, 1
- Ho, L. C., Filippenko, A. V., & Sargent, W. L. W. 1997, *ApJS*, 112, 315
- Hoekstra, H., Barthel, P. D., & Hes, R. 1997, *A&A*, 319, 757
- Holt, S. S. et al. 1980, *ApJ*, 241, L13
- Hui, Z., Ford, H. C., Ciardullo, R., & Jacoby, G. H. 1993, *ApJ*, 414, 463
- Ichimaru, S. 1977, *ApJ*, 214, 840
- Impey, C. & Gregorini, L. 1993, *AJ*, 105, 853
- Iyomoto, N., Makishima, K., Tashiro, M., Inoue, S., Kaneda, H., Matsumoto, Y., & Mizuno, T. 1998, *ApJ*, 503, L311
- Isobe, T., Feigelson, E. D., & Nelson, P.I. 1986, *ApJ*, 306, 490
- Iwasawa, K., Allen, S. W., Fabian, A. C., Edge, A. C., & Ettori, S. 1999a, *MNRAS*, in press (astro-ph/9902159)
- Iwasawa, K. et al. 1999b, in prep.
- Iwasawa, K., Yaqoob, T., Awaki, H., & Ogasaka, Y. 1994, *PASJ*, 46, L167
- Jackson, N. & Browne, I. W. A. 1990, *Nature*, 343, 43
- Jackson, N. & Browne, I. W. A. 1991, *MNRAS*, 250, 414
- Jackson, N. & Rawlings, S. 1997, *MNRAS*, 286, 241
- Jones, P. A. & McAdam, W. B. 1992, *ApJS*, 80, 137
- Kaastra, J.S., Kunieda, H., & Awaki, H. 1991, *A&A*, 242, 27
- Kay, L., Eracleous, M., Moran, E., Magalhaes, A. M., & Halpern, J., 1999, in *Structure and kinematics of quasar Broad-Line Regions*, eds. C. M. Gaskell et al., (San Francisco: ASP), in press
- Kaneda, H. et al. 1995, *ApJ*, 453, L13
- Keel, W. C., & Martini, P. 1995, *AJ*, 109, 2305
- Kellerman, K. I., Pauliny-Toth, I. I. K., & Williams, P. J. S. 1969, *ApJ*, 157, 1
- Kellerman, K. I., Sramek, R. A., Schmidt, M., Shaffer, D. B. , & Green, R. F. 1989, *AJ*, 98, 1195
- Kellerman, K. I., Sramek, R. A., Schmidt, M., Green, R. F., & Shaffer, D. B. 1994, *AJ*, 108, 1163
- Kim, D.-W., Fabbiano, G., & Mackie, G. 1998, *ApJ*, 497, 699
- Knapp, G.R., Guhathakurta, P., Kim, D.-W., & Jura, M.A. 1989, *ApJS*, 70, 329
- de Koff, S. et al. 1996, *ApJS*, 107, 621
- Königl, A. & Kartje, J. F. 1994, *ApJ*, 434, 446
- Kubo, H., Takahashi, T., Madejski, G., Tashiro, M., Makino, F., Inoue, S., & Takahara, F. 1998, *ApJ*, 504, 693
- Kühr, H., Witzel, A., Pauliny-Toth, I. I. K., & Nauber, U. 1981, *A&AS*, 45, 367

- Laing, R. A., Jenkins, C. R., Wall, J. V., & Unger, S. W. 1994 in *The First Stromlo Symposium: The Physics of Active Galaxies*, eds. G. V. Bicknell, M. A. Dopita, & P. J. Quinn, ASP Conference Series 54, (San Francisco: ASP), 201
- Lasota, J.-P., Abramowicz, M. A., Chen, X., Krolik, J., Narayan, R., & Yi, I. 1996, *ApJ*, 462, 142
- Lawrence, C. R., Zucker, J.R., Readhead, A. C. S., Unwin, S.C., Pearson, T.J., & Xu, W. 1996, *ApJS*, 107, 541
- Lawson, A. J. & Turner, M. J. L. 1997, *MNRAS*, 288, 920
- Lawson, A. et al. 1992, *MNRAS*, 259, 743
- Leahy, D.A. & Creighton, J. 1993, *MNRAS*, 263, 314
- Leahy, J. P. & Perley, R. A. 1991, *AJ*, 102, 537 Lawrence, C. R., Zucker, J. R., Readhead, A. C. S. Unwin, S. C., Pearson, T. J., & Xu, W. 1996, *ApJS*, 107, 541
- Lee, J. C., Fabian, A. C., Reynolds, C. S., Iwasawa, K., & Brandt, W.N. 1998, *MNRAS*, 300, 583
- Leighly, K. M. & O'Brien, P. T. 1997, *ApJ*, 481, L15
- Leighly, K. M. et al. 1997, *ApJ*, 483, 767
- Lightman, A. P. & White, T. R. 1988, *ApJ*, 335, 57
- Liszt, H. 1994, *ApJ*, 429, 638
- Liszt, H. & Wilson, R. W. 1993, *ApJ*, 403, 663
- Low, F. J. et al. 1984, *ApJ*, 278, L19
- Mack, K.-H., Kerp, J., & Klein, U. 1997, *A&A*, 324, 870
- Magdziarz, P. & Zdziarski, A.A. 1995, *MNRAS*, 273, 837
- Mantovani, F., Junor, R., Fanti, R., Padrielli, L., Browne, I. W. A., & Muxlow, T. W. B. 1992, *MNRAS*, 257, 353
- Markevitch, M. 1998, *ApJ*, 504, 27
- Marziani, P., Sulentic, J. W., Dultzin-Hacyan, D., Calvani, M., & Moles, M. 1996, *ApJS*, 104, 37
- Mathur, S. 1994, *ApJ*, 431, L75
- Mathur, S., Wilkes, B., Elvis, M., & Fiore, F. 1994, *ApJ*, 434, 493
- Mazzarella, J. M., Graham, J. R., Sanders, D. B., & Djorgovski, S. 1993, *ApJ*, 409, 170
- Miley, G. K. 1980, *ARAA*, 18, 165
- Miller, L., Longair, M. S., Fabbiano, G., Trinchieri, G., & Elvis, M. 1985, *MNRAS*, 215, 799
- Morganti, R., Killeen, N. E. B., & Tadhunter, C. N. 1993, *MNRAS*, 263, 1023
- Morganti, R., Fanti, R., Gioia, I.M., Harris, D.E., Parma, P., & de Ruiter, H. 1988, *A&A*, 189, 11
- Morrison, R. & McCammon, D. 1983, *ApJ*, 270, 119
- Moshir, M. et al. 1990, *IRAS Faint Source Catalog*, v.2.0
- Mulchaey, J. S. et al. 1994, *ApJ*, 436, 586
- Mulchaey, J. S. & Zabludoff, A. I. 1998, *ApJ*, 498, L5
- Murphy, E. M., Lockman, F. J., Laor, A., & Elvis, E. 1996, *ApJS*, 105, 369
- Mushotzky, R. F. & Scharf, C. A. 1997, *ApJ*, 482, L13
- Mushotzky, R. F., Fabian, A. C., Iwasawa, K., Kunieda, H., Matsuoka, M., Nandra, K., & Tanaka, Y. 1995, *MNRAS*, 272, L9
- Nandra, K., George, I. M., Mushotzky, R. F., Turner, T.J., & Yaqoob, T. 1997a, *ApJ*, 477, 602
- Nandra, K., George, I. M., Mushotzky, R. F., Turner, T.J., & Yaqoob, T. 1997b, *ApJ*, 476, 70
- Nandra, K., George, I. M., Mushotzky, R. F., Turner, T.J., & Yaqoob, T. 1997c, *ApJ*, 488, L91
- Nandra, K. & Pounds, K. A. 1994, *MNRAS*, 268, 405
- Narayan, R. & Raymond, J. 1999, *ApJ*, 515, L69
- Narayan, R., Mahadevan, R., & Quataert, E. 1998, in *The Theory of Black Hole Accretion Disks*, eds. M.A.Abramowicz, G.Bjornsson, & J.E.Pringle (Cambridge University Press) (astro-ph/9803141)

- Narayan, R. & Yi, I. 1995, ApJ, 444, 231
- Narayan, R. & Yi, I. 1994, ApJ, 428, L13
- Netzer, H., Turner, T. J., & George, I.M. 1998, ApJ, 504, 680
- Neugebauer, G., Miley, G. K., Soifer, B. T., & Clegg, P. E. 1986, ApJ, 308, 815
- Ogle, P. M., Cohen, M. H., Miller, J. S., Tran, H. S., Fosbury, R. A. E., & Goodrich, R. W. 1997, ApJ, 484, 193
- Osterbrock, D. E. & Miller, J. S. 1975, ApJ, 197, 535
- Owen, F. N., Ledlow, M. J., & Keel, W. C. 1996, AJ, 111, 530
- Owen, F. N., & Puschell, J. J., 1984, AJ, 89, 932
- Padovani, P., Morganti, R., Siebert, J., Vagnetti, F., & Cimatti, A. 1999, MNRAS, in press (astro-ph/9901129)
- Preuss, E., Pauliny-Toth, I. I. K., Witzel, A., Kellerman, K. I., & Shaffer, D. B. 1977, A&A, 54, 29
- Rawlings, S., Saunders, R., Eales, S. A., & Mackay, C.D. 1989, MNRAS, 240, 701
- Rawlings, S. & Saunders, R. 1991, Nature, 349, 138
- Rees, M. J., Begelman, M.C., Blandford, R. D., & Phinney, E.S. 1982, Nature, 295, 17
- Reeves, J. N., Turner, M. J. L., Ohashi, T., & Kii, T. 1997, MNRAS, 292, 468
- Reynolds, C. S., Iwasawa, K., Crawford, C. S., & Fabian, A.C. 1998, MNRAS, 299, 410
- Reynolds, C. S. 1997, MNRAS, 286, 513
- Reynolds, C.S., di Matteo, T., Fabian, A.C., Hwang, U., & Canizares, C.R. 1996, MNRAS, 283, L111
- Reynolds, C. S. & Fabian, A.C. 1996, MNRAS, 278, 479
- Reynolds, C. S. Fabian, A. C., Makishima, K., Fukazawa, Y., & Tamura, T. 1994, MNRAS, 268, L55
- Rhee, G., Burns, J. O., & Kowalski, M. 1994, AJ, 108, 1137
- Rothschild, R. et al. 1999, ApJ, 510, 651
- Rowan-Robinson, M., Jones, M., Leech, K., Vedi, K., & Hughes, J. 1991, MNRAS, 249, 729
- Sambruna, R. M., George, I. M., Mushotzky, R. F., Nandra, K., & Turner, T. J. 1998, ApJ, 495, 749
- Savage, B. D. & Mathis, J. S. 1979, ARAA, 17, 73
- Saunders, R., Baldwin, J. E., Rawlings, S., Warner, P. J., & Miller, L. 1989, MNRAS, 238, 777
- Seaton, M. J. 1979, MNRAS, 187, 73P
- di Serego Alighieri, S., Binette, L., Courvoisier, T.J.-L., Fosbury, R. A. E., & Tadhunter, C. N. 1988, Nature, 334, 591
- Serlemitsos, P., Ptak, A., & Yaqoob, T. 1996, in The Physics of LINERS in View of Recent Observations, ASP Conference Series, vol. 103, eds. M. Eracleous, A. Koratkar, C. Leitherer, & L. Ho, p.70
- Shastri, P., Wilkes, B.J., Elvis, M., & McDowell, J. 1993, ApJ, 410, 29
- Simon, A. 1979, MNRAS, 188, 637
- Simpson, C., Ward, M. J., & Wilson, A. S. 1995, ApJ, 454, 683
- Singh, K. P., Rao, A. R., & Vahia, M. N. 1990, MNRAS, 246, 706
- Smith, D. A. & Done, C. 1996, MNRAS, 280, 355
- Smith, H. E., Spinrad, H., & Hunstead, R. 1976, ApJ, 206, 345
- Spinoglio, L., Malkan, M. A., Rush, B., Carrasco, L., & Recillas-Cruz, E. 1995, ApJ, 453, 616
- Spinrad, H., Smith, H. E., Hunstead, R., & Ryle, M. 1975 ApJ 198, 7
- Stark, A. A., Gammie, C. F., Wilson, R. W., Bally, J., Linke, R. A., Heiles, C., & Hurwitz, M. 1992, ApJS, 79, 77
- Storchi-Bergmann, T., Bica, E., Kinney, A. L., & Bonato, C. 1997, MNRAS, 293, 231
- Sugizaki, M., Inoue, H., Sonobe, T., Takahashi, T., & Yamamoto, Y. 1997, PASJ, 49, 59
- Tadhunter, C. N., Morganti, R., Robinson, A., Dickson, R., Villar-Martin, M., & Fosbury, R. A. E. 1998, MNRAS, 298, 1035



- Tadhunter, C. N., Dickson, R. C., & Shaw, M.A. 1996, MNRAS, 281, 591
- Tadhunter, C. N., Morganti, R., di Serego Alighieri, S., Fosbury, R. A. E., & Danziger, I. J. 1993, MNRAS, 263, 999
- Tadhunter, C. N. et al. 1988, MNRAS, 235, 403
- Tanaka, Y., Inoue, H., & Holt, S.S. 1994, PASJ, 46, L37
- Tanaka, Y., et al. 1995, Nature, 375, 659
- Tashiro, M., Kaneda, H., & Makishima, K. 1998, in *The Hot Universe*, eds. K.Koyama et al., 289
- Tran, H. D., Cohen, M. H., & Goodrich, R. W. 1995, AJ, 110, 2597
- Trussoni, E., Massaglia, S., Ferrari, R., Fanti, R., Feretti, L., Parma, P., & Brinkmann, W. 1997, A&A, 327, 27
- Tsai, J. C. & Mathews, W. G. 1995, ApJ, 448, 84
- Turner, T. J., George, I. M., Nandra, K., & Mushotzky, R. F. 1997a, ApJS, 113, 23
- Turner, T. J., George, I. M., Mushotzky, R. F., & Nandra, K. 1997b, ApJ, 475, 118
- Turner, T. J., et al. 1999, ApJ, 510, 178
- Ueno, S., Mushotzky, R. F., Koyama, K., Iwasawa, K., Awaki, H., & Hayashi, I. 1994a, PASJ, 46, L71
- Ueno, S., Koyama, K., Nishida, M., Yamauchi, S., & Ward, M. 1994b, ApJ, 431, L1
- Urry, C.M. & Padovani, P. 1995, PASP, 107, 803
- Vignali, C., Comastri, A., Cappi, M., Palumbo, G.G.C., Matsuoka, M., & Kubo, H. 1999, ApJ, in press (astro-ph/9812176)
- Wall, J. V. & Peacock, J. A. 1985, MNRAS, 216, 173
- Weaver, K. A., Krolik, J. H., & Pier, E. A. 1998, ApJ, 498, 213
- Weaver, K. A. & Reynolds, C. S. 1998, ApJ, 503, L39
- Weaver, K. A. & Yaqoob, T. 1998, ApJ, 502, L139
- White, R. L. & Becker, R. H. 1992, ApJS, 79, 331
- Wilkes, B. J., Tananbaum, H., Worrall, D. M., Avni, Y., Oey, M. S., & Flanagan, J. 1994, ApJS, 92, 53
- Wilkes, B. J. & Elvis, M. 1987, ApJ, 323, 293
- Wills, B. J. & Browne, I. W. A. 1986, ApJ, 302, 56
- Wills, B. J., et al. 1993, ApJ, 410, 534
- Wills, B. J., et al. 1995, ApJ, 447, 139
- Worrall, D. M., Birkinshaw, M., & Cameron, R.A. 1995, ApJ, 449, 93
- Worrall, D. M., Lawrence, C. R., Pearson, T. J., & Readhead, A. C. S. 1994, ApJ, 420, L17
- Worrall, D. M. & Birkinshaw, M. 1994, ApJ, 427, 134
- Woźniak, P. R., Zdziarski, A. A., Smith, D., Madejski, G.M., & Johnson, W. N. 1998, MNRAS, 299, 449
- Yates, M. G. & Longair, M. S. 1989, MNRAS, 241, 29
- Yee, H. K. C. 1980, ApJ, 241, 894
- Young, S., Axon, D.J., Hough, J. H., Fabian, A. C., & Ward, M. J. 1998, MNRAS, 294, 478
- Young, S., Hough, J. H., Efstathiou, A., Wills, B.J., Axon, D. J., Bailey, J.A., & Ward, M. J. 1996, MNRAS, 279, L72
- Zensus, J. A., Porcas, R. W., & Pauliny-Toth, I. I. K. 1984, A&A, 133, 27
- Zirbel, E. L. & Baum, S. A. 1998, ApJS, 114, 177
- Zirbel, E. L. 1997, ApJ, 476, 489

TABLE 1  
ASCA SAMPLE OF RADIO-LOUD AGNs AND THEIR PROPERTIES

Object	$z$	Coordinates (B1950)	Other Name(s)	$N_{\text{H, Gal}}^{\text{a}}$ ( $10^{20} \text{ cm}^{-2}$ )	$\log R^{\text{c}}$	$\log \text{Luminosity}^{\text{b}}$ ( $\text{erg s}^{-1}$ )				References <sup>d</sup>
						5 GHz <sup>c</sup>	[O III]	12 $\mu\text{m}$	60 $\mu\text{m}$	
<i>Broad-Line Radio Galaxies</i>										
3C 111	0.048	0415 + 37	4C +37.12	32.61 <sup>e</sup>	-0.80	42.17	...	44.56	45.06	1,2
3C 120	0.033	0430 + 05	4C +05.20	12.32	-0.13	41.68	42.85	44.70	45.38	3,4,5,6
Pictor A	0.035	0518 - 45	PKS	4.20	-1.17	42.24	41.87	44.32	44.49	4,7,6
3C 215	0.412	0903 + 16	4C +16.26, PKS	3.61	-1.53	42.88	43.09	...	...	1,8
3C 303	0.141	1441 + 52	4C +52.33	1.60	-1.08	42.24	42.43	<45.02	<45.73	1,2,9,10,11
3C 382	0.058	1833 + 32	4C +32.55	6.70	-1.05	41.82	42.63	44.57	44.74	1,2,3,10,12
3C 390.3	0.057	1845 + 79	4C +79.18	3.74	-1.00	42.09	43.27	44.88	45.08	2,3,6
3C 411	0.467	2019 + 09	4C +09.67	12.00	...	43.19	43.09	...	...	1,13,14
3C 445	0.057	2221 - 02	4C -02.83	5.33	-1.43	41.84	41.13	44.88	45.14	2,4,5,6
PKS 2251+11	0.326	2155 + 11	4C +11.72, PG	4.77	-1.51	42.76	42.86	<45.48	<46.30	15,16,17
<i>Narrow-Line Radio Galaxies</i>										
3C 99	0.426	0358 + 04	4C +00.14	10.50	-0.70	43.00	43.20	...	...	1,2,14,18,19
PKS 0634 - 20	0.055	0634 - 20		21.00	<-2.32	41.90	41.44	<44.69	...	20,21,22
4C +55.16	0.242	0831 + 55	S4	4.13	-0.82	43.44	44.17	...	...	6,23,24
3C 219	0.174	0917 + 45	4C +45.19	1.52	-2.70	42.86	42.72	<45.12	<45.03	2,6,10,25
3C 275	0.480	1239 - 04	4C -04.43	2.09	...	43.43	43.74	...	...	1,2,14,26,27
3C 295	0.510	1409 + 52		1.38	<-2.53	44.31	42.42	<47.19	<46.07	1,2,10,25
3C 313	0.461	1508 + 08	4C +08.44	2.54	<-3.12	43.49	43.19	...	...	1,2,14,25,26
3C 321	0.096	1529 + 24	4C +24.34	5.00	-1.68	42.00	43.49	<46.02	<46.22	2,6,28,29
3C 330	0.550	1609 + 66	4C +66.17	2.94	...	43.90	42.34	<46.08	<47.01	2,6,30
3C 346	0.161	1641 + 17	4C +17.70	5.49	-1.59	42.53	42.04	...	...	6,25,31
Cygnus A	0.056	1957 + 40	3C 405, 4C +40.40	33.00	-2.63	44.06	43.55	44.90	46.17	1,2,32
PKS 2152 - 69	0.028	2152 - 69		3.60	-1.49	41.97	41.55	<43.88	<44.53	2,4,5,6
<i>Quasars</i>										
3C 109	0.306	0410 + 11	4C +11.18, PKS	14.70	-0.79	43.23	43.72	46.08	46.54	1,2,10,14
3C 234	0.185	0958 + 29	4C +20.35	2.00	-1.34	42.73	43.66	46.00	46.11	2,6,10,14,33
3C 249.1	0.312	1100 + 77	4C +77.09, PG	3.23	-1.09	42.89	44.10	...	...	1,2,26,34,35
3C 254	0.734	1111 + 40	4C +40.28	1.82	-2.04	43.75	43.87	...	...	1,2,36,37,38

TABLE 1—*Continued*

Object	$z$	Coordinates (B1950)	Other Name(s)	$N_{\text{H,Gal}}^{\text{a}}$ ( $10^{20} \text{ cm}^{-2}$ )	$\log R^{\text{c}}$	log Luminosity <sup>b</sup> (erg s <sup>-1</sup> )				References <sup>d</sup>
						5 GHz <sup>c</sup>	[O III]	12 $\mu\text{m}$	60 $\mu\text{m}$	
3C 368	1.131	1802 + 11	4C +11.54, PKS	9.80	<-4.32	43.68	45.59	<46.80	<47.54	1,2,25,26
4C +74.26	0.104	2043 + 74	S5	12.80	...	...	...	...	...	23
<i>Radio Galaxies</i>										
3C 28	0.195	0053 + 26	4C +26.02	5.10	<-4.61	42.23	<41.25	<45.37	<45.69	1,25,39
PKS 0131 - 36 <sup>†</sup>	0.030	0131 - 36	NGC 612, MRC	1.83	-2.04	41.54	39.71	44.48	45.41	2,4,5
IC 310	0.018	0313 + 41	MCG +07-07-045	14.00	-0.25	39.71	...	<44.32	<44.38	22,40,41,42
Fornax A <sup>†</sup>	0.005	0320 - 37	NGC 1316	1.98	-3.40	41.24	<38.65	42.94	44.08	2,4,5
PKS 0625 - 53 <sup>†</sup>	0.054	0625 - 53	MRC	4.00	-1.67	41.72	<39.42	...	...	4,5,6
4C +41.17	3.798	0647 + 41	B3	12.00	-0.70	45.21	...	...	...	42
3C 270 <sup>†</sup>	0.0074	1216 + 06	NGC 4261	1.70	-1.46	40.67	<41.06	42.63	41.60	2,5,6,43
Centaurus A	0.0008 <sup>f</sup>	1322 - 42	NGC 5128	7.00	-0.90	39.93	39.58	43.05	44.23	5,6,44
PKS 1333 - 33 <sup>†</sup>	0.013	1333 - 33	IC 4296	4.20	-1.31	40.99	<38.87	<44.38	<43.64	2,4,5,6
NGC 6251	0.025	1638 + 83		5.80	...	40.93	40.92	<44.27	44.28	6,12,45
3C 353 <sup>†</sup>	0.030	1717 - 00	4C -00.67	8.53	-2.25	42.25	40.28	<43.56	...	4,5,6,33

<sup>a</sup> The Galactic equivalent H I column density from 21 cm surveys (see §2 of the text for references).

<sup>b</sup> All luminosities are rest-frame monochromatic luminosities (i.e.,  $\nu L_\nu$ ) at the listed frequency or wavelength with the exception of the [O III] luminosity, which is the integrated emission-line luminosity. They were computed assuming  $H_0 = 75 \text{ km s}^{-1} \text{ Mpc}^{-1}$  and  $q_0 = \frac{1}{2}$ . For more details about the applied corrections and relevant assumptions, see §2 of the text.

<sup>c</sup>  $R$  is the rest-frame ratio of the compact-core radio power to lobe radio power, defined as  $R = S_{\text{core}}/S_{\text{lobe}}$ . The quoted 5 GHz luminosity is a total (spatially-integrated) luminosity of the double-lobed radio source *without* the compact core.

<sup>d</sup> REFERENCES.— (1) Kellerman, Pauliny-Toth, & Williams 1969; (2) Golombek, Miley, & Neugebauer 1988; (3) Wills & Browne 1986; (4) Tadhunter et al. 1993; (5) Morganti, Killeen, & Tadhunter 1993; (6) Wall & Peacock 1985; (7) Jones & McAdam 1992; (8) Heckman et al. 1994; (9) Jackson & Browne 1991; (10) Rawlings et al. 1989; (11) Leahy & Perley 1991; (12) Rawlings & Saunders 1991; (13) Spinrad et al. 1975; (14) Hes, Barthel, & Hoekstra 1995; (15) Feigelson, Isobe, & Kembhavi 1984; (16) Marziani et al. 1996; (17) Neugebauer et al. 1986; (18) Smith, Spinrad, & Hunstead 1976; (19) Grandi & Osterbrock 1978; (20) Simpson, Ward, & Wilson 1995; (21) Danziger, Goss, & Frater 1978; (22) Moshir et al. 1990; (23) Zensus, Porcas, & Pauliny-Toth 1984; (24) Lawrence et al. 1996; (25) Giovannini et al. 1988; (26) Jackson & Rawlings 1997; (27) Mantovani et al. 1992 (28) Saunders et al. 1989; (29) Kühr et al. 1981; (30) Keel & Martini 1995; (31) Gelderman & Whittle, 1994; (32) Osterbrock & Miller 1975; (33) Yates & Longair 1989; (34) Kellerman et al. 1994; (35) Bridle et al. 1994; (36) Wills et al. 1995; (37) Wills et al. 1993; (38) Owen & Puschell 1984; (39) Jackson & Browne 1990; (40) White & Becker 1992; (41) Preuss et al. 1977; (42) Becker, White, & Edwards 1991; (43) Ho, Filippenko, & Sargent 1997 (44) Storchi-Bergmann et al. 1997; (45) Antonucci 1984.

<sup>e</sup> The source is located behind a molecular cloud (Bania, Marscher, & Barvainis 1991; see § 8.4.2 of the text) with complex structure; here only the HI contribution to the Galactic column is quoted (from Elvis et al. 1989).

<sup>f</sup> The observed, kinematic redshift of Centaurus A is 0.002. However, the distance to the host galaxy is measured to be 3.5 Mpc (Hui et al. 1993), which corresponds to a cosmological redshift of 0.0008.

<sup>†</sup> Weak-line radio galaxy (see text for details).

TABLE 2  
LOG OF ASCA OBSERVATIONS OF RADIO-LOUD AGNs

Object	U.T. Date (yy/mm/dd)	Image #	Exposure (ks)	SIS 0 Count Rate (counts s <sup>-1</sup> )	GIS 2 Count Rate (counts s <sup>-1</sup> )
<i>Broad-Line Radio Galaxies</i>					
3C 111	96/02/13	74087000	37.4	0.716 ± 0.005	0.511 ± 0.004
3C 120	94/02/17	71014000	47.9	1.863 ± 0.006	0.978 ± 0.004
Pictor A	96/11/23	74066000	62.5	0.464 ± 0.003	0.296 ± 0.002
3C 215	95/11/04	83041000	32.6	0.083 ± 0.002	0.050 ± 0.002
3C 303 (1)	95/05/21	73008000	17.8	0.064 ± 0.003	0.037 ± 0.002
(2)	96/01/24	73008010	14.4	0.058 ± 0.002	0.030 ± 0.002
3C 382	94/04/18	71025000	40.5	1.793 ± 0.007	1.072 ± 0.005
3C 390.3 (1)	93/11/16	71008000	43.5	0.532 ± 0.004	0.302 ± 0.003
(2)	95/01/15	73082000	19.2	0.528 ± 0.004	0.363 ± 0.005
(3)	95/05/05	73082010	18.0	0.856 ± 0.009	0.545 ± 0.006
3C 411	94/10/23	72018000	21.5	0.016 ± 0.001	0.012 ± 0.001
3C 445	95/06/01	73007000	41.3	0.054 ± 0.001	0.048 ± 0.001
PKS 2251+11	96/06/01	74076000	25.0	0.014 ± 0.003	0.017 ± 0.001
<i>Narrow-Line Radio Galaxies</i>					
3C 99	95/08/27	73016000	29.3	< 0.005 <sup>a</sup>	< 0.003 <sup>a</sup>
PKS 0634-205	95/10/09	73058000	40.5	0.005 ± 0.0005	0.006 ± 0.001
4C +55.16	96/11/01	74036000	21.0	0.126 ± 0.002	0.066 ± 0.002
3C 219 (1)	94/04/16	71042020	19.1	0.086 ± 0.003	0.049 ± 0.003
(2)	95/04/12	71042020	16.6	0.124 ± 0.004	0.067 ± 0.003
3C 275	96/08/05	74017000	17.5	< 0.008 <sup>a</sup>	< 0.006 <sup>a</sup>
3C 295	94/05/03	71003000	22.9	0.048 ± 0.002	0.033 ± 0.006
3C 313	94/02/06	71004000	41.4	0.005 ± 0.0008	0.010 ± 0.0006
3C 321	97/02/06	75055000	60.0	0.003 ± 0.0005	0.003 ± 0.0007
3C 330	95/03/05	83042000	38.3	< 0.010 <sup>a</sup>	< 0.009 <sup>a</sup>
3C 346	95/02/17	73092000	21.2	0.022 ± 0.001	0.015 ± 0.002
Cygnus A (1)	93/05/27	70003000	21.1	0.911 ± 0.007	0.947 ± 0.006
(2)	93/10/27	70003010	27.8	0.967 ± 0.006	1.261 ± 0.006
PKS 2152-69	95/10/17	73083000	29.2	0.206 ± 0.004	0.119 ± 0.003
<i>Quasars</i>					

TABLE 2—*Continued*

Object	U.T. Date (yy/mm/dd)	Image #	Exposure (ks)	SIS 0 Count Rate (counts s <sup>-1</sup> )	GIS 2 Count Rate (counts s <sup>-1</sup> )
3C 109	95/08/28	73046000	37.5	0.132 ± 0.003	0.084 ± 0.002
3C 234	94/05/04	71043000	19.1	0.010 ± 0.003	0.009 ± 0.001
3C 249.1	96/12/03	74050000	23.0	0.079 ± 0.002	0.037 ± 0.002
3C 254	96/12/08	74035000	39.0	0.038 ± 0.001	0.026 ± 0.001
3C 368	93/09/12	70017000	27.7	... <sup>b</sup>	< 0.004 <sup>a</sup>
4C +74.26	96/08/10	74097000	23.0	0.616 ± 0.006	0.366 ± 0.004
<i>Radio Galaxies</i>					
3C 28	94/08/05	82034000	22.9	0.195 ± 0.003	0.100 ± 0.002
PKS 0131 – 36 <sup>†</sup>	96/07/14	64002000	70.0	0.0076 ± 0.0005	0.0095 ± 0.0007
Fornax A <sup>†</sup>	94/01/11	61002000	19.0	0.036 ± 0.002	0.0251 ± 0.0012
IC 310	94/02/09	81026000	13.9	0.164 ± 0.005	0.1833 ± 0.0033
PKS 0625 – 53 <sup>†</sup>	94/11/28	72019000	20.0	0.236 ± 0.004	0.337 ± 0.005
4C+41.17	94/03/23	71001000	35.3	... <sup>c</sup>	... <sup>c</sup>
3C 270 <sup>†</sup>	96/06/23	74085000	60.3	0.045 ± 0.001	0.029 ± 0.001
Centaurus A	93/08/14	70020000	37.4	0.706 ± 0.005	1.374 ± 0.007
PKS 1333 – 33 <sup>†</sup>	94/02/15	61006000	40.0	0.032 ± 0.002	0.031 ± 0.001
NGC 6251	94/10/28	72035000	41.1	0.071 ± 0.002	0.042 ± 0.001
3C 353 <sup>†</sup>	96/09/15	74037000	28.0	0.039 ± 0.001	0.036 ± 0.001

<sup>a</sup> 3 $\sigma$  upper limit.<sup>b</sup> Out of the SIS field of view.<sup>c</sup> Source located on the outskirts of an extended unidentified system (see Appendix).<sup>†</sup> Weak-Line Radio Galaxy

TABLE 3  
BEST-FITTING CONTINUUM MODELS

Object	Best-Fitting Model and Parameters <sup>a</sup>	$\chi_r^2/\text{d.o.f.}$	Observed Flux <sup>b</sup>		Intrinsic Luminosity <sup>c</sup>	
			0.5–2 keV ( $10^{-12}$ erg $\text{cm}^{-2}$ $\text{s}^{-1}$ )	2–10 keV	0.5–2 keV ( $10^{44}$ erg $\text{s}^{-1}$ )	2–10 keV
<i>Broad-Line Radio Galaxies</i>						
3C 111	Absorbed P.law ( $N_{\text{H}} = 9.63_{-0.21}^{+0.24} \times 10^{21}$ $\text{cm}^{-2}$ , $\Gamma = 1.75 \pm 0.02$ )	0.98/1713	...	35.0	...	1.6
3C 120	Absorbed P.law ( $N_{\text{H}} = 1.65 \pm 0.05 \times 10^{21}$ $\text{cm}^{-2}$ , $\Gamma = 2.02_{-0.03}^{+0.05}$ )	0.96/1143	...	42.0	...	0.9
Pictor A	Absorbed P.law ( $N_{\text{H}} = 8.25_{-0.97}^{+0.99} \times 10^{20}$ $\text{cm}^{-2}$ , $\Gamma = 1.80 \pm 0.02$ )	1.02/1501	...	13.4	...	0.3
3C 215	P.law ( $\Gamma = 1.72 \pm 0.04$ )	0.92/386	...	2.3	...	8.0
3C 303	Absorbed P.law ( $N_{\text{H}} = 1.24_{-0.44}^{+0.63} \times 10^{21}$ $\text{cm}^{-2}$ , $\Gamma = 1.82_{-0.05}^{+0.18}$ )	1.01/366	...	2.0	...	0.8
3C 382	Power law ( $\Gamma = 1.12_{-0.29}^{+0.10}$ )	1.03/982	...	31.0	...	2.0
	+ Bremsstrahlung ( $kT = 1.94_{-0.06}^{+0.24}$ keV)		18.0	...	1.4	...
3C 390.3 (1)	Absorbed P.Law ( $N_{\text{H}} = 6.96_{-2.38}^{+2.66} \times 10^{20}$ $\text{cm}^{-2}$ , $\Gamma = 1.75 \pm 0.02$ ) + Edge ( $E_c = 0.776_{-0.021}^{+0.063}$ keV, $\tau_e = 0.25_{-0.14}^{+0.08}$ ) + Reflection ( $A \sim 0.7$ )	1.04/1157	...	16.0	...	1.0
(2)	Absorbed P.Law ( $N_{\text{H}} = 1.2 \pm 0.3 \times 10^{21}$ $\text{cm}^{-2}$ , $\Gamma = 1.70 \pm 0.030.05$ )	1.02/792	...	19.4	...	1.2
(3)	Absorbed P.law ( $N_{\text{H}} = 9.9_{-1.48}^{+1.15} \times 10^{20}$ $\text{cm}^{-2}$ , $\Gamma = 1.78 \pm 0.02$ )	1.03/963	...	30.2	...	1.9
3C 411	P.law ( $\Gamma = 1.75 \pm 0.15$ )	1.21/59	...	0.8	...	3.6
3C 445	Dual Absorber ( $\Gamma = 1.25_{-0.27}^{+0.29}$ , $N_{\text{H},1} = 2.5_{-1.3}^{+8.7} \times 10^{23}$ $\text{cm}^{-2}$ , $N_{\text{H},2} = 5.8_{-1.8}^{+3.2} \times 10^{22}$ $\text{cm}^{-2}$ , $f_{c,2} = 0.88_{-0.21}^{+0.13}$ )	1.05/414	...	7.3	...	0.8
PKS 2251+11	Absorbed P.law ( $N_{\text{H}} = 6.0_{-2.2}^{+3.0} \times 10^{21}$ $\text{cm}^{-2}$ , $\Gamma = 1.14_{-0.18}^{+0.23}$ )	1.28/97	...	1.5	...	2.8
<i>Narrow-Line Radio Galaxies</i>						
PKS 0634 – 205	Partial Covering ( $N_{\text{H}} = 7.9_{-4.3}^{+12.9} \times 10^{23}$ $\text{cm}^{-2}$ , $f_c = 0.96_{-0.08}^{+0.03}$ , $\Gamma = 1.94_{-0.33}^{+0.40}$ )	1.03/52	...	0.6	...	0.3
4C +55.16	Absorbed Raymond-Smith ( $N_{\text{H}} = 1.22_{-0.32}^{+0.26} \times 10^{21}$ $\text{cm}^{-2}$ , $kT = 3.92_{-0.27}^{+0.28}$ keV, $Y = 0.54_{-0.11}^{+0.12}$ )	1.10/443	2.0	...	2.9	...
3C 219 (1)	Absorbed P.law ( $N_{\text{H}} = 2.2_{-1.1}^{+1.5} \times 10^{21}$ $\text{cm}^{-2}$ , $\Gamma = 1.79_{-0.12}^{+0.18}$ ) + Raymond-Smith ( $kT = 0.78_{-0.20}^{+0.18}$ keV, $Y \equiv 1$ )	0.88/188	...	2.6	...	1.6
(2)	Absorbed P.law ( $N_{\text{H}} = 1.1_{-1.1}^{+0.4} \times 10^{21}$ $\text{cm}^{-2}$ , $\Gamma = 1.73 \pm 0.08$ )	0.95/291	...	3.4	...	2.1
3C 295	Raymond-Smith ( $kT = 6.22_{-1.03}^{+1.33}$ keV, $Y = 0.49_{-0.28}^{+0.31}$ )	1.00/85	0.6	...	3.2	...
3C 313	P.law ( $\Gamma = 1.73_{-0.30}^{+0.36}$ )	0.86/79	...	0.1	...	0.6
3C 321	Absorbed P.law ( $N_{\text{H}} = 1.0_{-1.0}^{+2.2} \times 10^{22}$ $\text{cm}^{-2}$ , $\Gamma = 1.46_{-0.79}^{+1.20}$ ) + Raymond-Smith ( $kT = 0.57_{-0.27}^{+0.20}$ keV, $Y \equiv 1$ )	1.41/133	...	0.2	...	0.03
			0.03	...	0.006	...

TABLE 3—Continued

Object	Best-Fitting Model and Parameters <sup>a</sup>	$\chi_r^2/\text{d.o.f.}$	Observed Flux <sup>b</sup>		Intrinsic Luminosity <sup>c</sup>	
			0.5–2 keV ( $10^{-12}$ erg $\text{cm}^{-2}$ $\text{s}^{-1}$ )	2–10 keV	0.5–2 keV ( $10^{44}$ erg $\text{s}^{-1}$ )	2–10 keV
3C 346	P.law ( $\Gamma = 1.81 \pm 0.12$ )	0.88/99	...	0.9	...	0.5
Cygnus A (1) <sup>d</sup>	Absorbed P.law ( $N_{\text{H}} = 1.1_{-0.6}^{+2.1} \times 10^{23}$ $\text{cm}^{-2}$ , $\Gamma = 1.80_{-0.43}^{+0.28}$ )	1.03/834	...	24.0	...	1.1
	+ Raymond-Smith ( $kT = 7.56 \pm 1.45$ keV, $Y = 0.77_{-0.40}^{+4.23}$ )		16.0	...	2.0	...
(2) <sup>d</sup>	Absorbed P.law ( $N_{\text{H}} = 1.5_{-0.9}^{+2.1} \times 10^{23}$ $\text{cm}^{-2}$ , $\Gamma = 1.76_{-0.34}^{+0.35}$ )	1.04/932	...	33.3	...	3.4
	+ Raymond-Smith ( $kT = 8.4_{-1.4}^{+1.3}$ keV, $Y = 0.53_{-0.19}^{+4.57}$ )		16.0	...	1.8	...
PKS 2152 – 69	Absorbed P.law ( $N_{\text{H}} = 1.4_{-0.9}^{+2.1} \times 10^{21}$ $\text{cm}^{-2}$ , $\Gamma = 1.88 \pm 0.08$ )	0.93/586	...	4.3	...	0.06
	+ Raymond-Smith ( $kT = 0.88_{-0.11}^{+0.07}$ keV, $Y = 0.20_{-0.04}^{+0.15}$ )		1.0	...	0.02	...
<i>Quasars</i>						
3C 109	Absorbed P.law ( $N_{\text{H}} = 4.8 \pm 0.4 \times 10^{21}$ $\text{cm}^{-2}$ , $\Gamma = 1.73_{-0.06}^{+0.05}$ )	1.04/683	...	5.5	...	10.8
3C 234	Partial Covering ( $N_{\text{H}} = 2.4_{-1.2}^{+4.0} \times 10^{23}$ $\text{cm}^{-2}$ , $f_{\text{c}} = 0.33_{-0.26}^{+0.16}$ , $\Gamma \sim 0.08$ ) + Raymond-Smith ( $kT = 0.89_{-0.67}^{+0.79}$ keV, $Y \equiv 1$ )	1.08/50	...	1.3	...	0.8
			0.02	...	0.04	...
3C 249.1	P.law ( $\Gamma = 1.76 \pm 0.04$ )	1.00/341	...	2.3	...	4.6
3C 254	P.law ( $\Gamma = 1.67 \pm 0.06$ )	1.09/248	...	1.4	...	15.0
4C +74.26	Absorbed Double P.law ( $N_{\text{H}} = 3.5_{-0.3}^{+0.4} \times 10^{21}$ $\text{cm}^{-2}$ , $\Gamma_1 = 2.02 \pm 0.12$ , $\Gamma_2 \approx 0.2$ )	0.93/931	...	16.9 <sup>e</sup>	...	3.8 <sup>e</sup>
<i>Radio Galaxies</i>						
3C 28	Absorbed P.law ( $N_{\text{H}} = 2.4_{-1.1}^{+3.7} \times 10^{21}$ $\text{cm}^{-2}$ , $\Gamma = 1.53_{-0.28}^{+0.35}$ ) <sup>f</sup>	1.00/688	...	2.6	...	2.0
	+ Raymond-Smith ( $kT = 3.32_{-0.77}^{+1.13}$ keV, $Y = 0.28_{-0.14}^{+0.47}$ )		1.8	...	1.5	...
PKS 0131 – 36 <sup>†</sup>	Partial Covering ( $N_{\text{H},1} = 5.0_{-1.3}^{+1.7} \times 10^{23}$ $\text{cm}^{-2}$ , $f_{\text{c}} = 0.90_{-0.11}^{+0.03}$ , $\Gamma = 1.26_{-0.73}^{+0.39}$ )	1.11/244	...	0.8	...	0.04
	+ Raymond-Smith ( $kT = 1.03 \pm 0.12$ keV, $Y = 2.76_{-1.53}^{+3.07}$ )		0.1	...	0.002	...
Fornax A <sup>†</sup>	Absorbed p.law ( $N_{\text{H}} = 3.28_{-1.66}^{+2.04} \times 10^{22}$ $\text{cm}^{-2}$ , $\Gamma \equiv 1.5$ )	0.91/146	...	0.8	...	$5 \times 10^{-4}$
	+ Raymond-Smith ( $kT = 0.76 \pm 0.06$ keV, $Y = 0.09 \pm 0.04$ )		1.6	...	$8 \times 10^{-4}$	...
IC 310	P.law ( $\Gamma = 2.34_{-0.40}^{+1.90}$ )	0.98/420	...	2.4	...	0.02
	+ Raymond-Smith ( $kT = 5.61_{-2.76}^{+2.51}$ keV, $Y = 0.32_{-0.23}^{+1.87}$ )		1.8	...	0.02	...
PKS 0625 – 53 <sup>†</sup>	Absorbed Raymond-Smith ( $N_{\text{H}} = 8.4_{-2.1}^{+1.7} \times 10^{20}$ $\text{cm}^{-2}$ , $kT = 5.85_{-0.30}^{+0.52}$ keV, $Y = 0.32 \pm 0.08$ )	1.01/713	20.0	...	1.5	...
3C 270 <sup>†</sup>	P.law ( $\Gamma = 1.27_{-0.26}^{+0.19}$ )	1.03/424	...	0.9	...	$9 \times 10^{-4}$
	+ Raymond-Smith ( $kT = 0.84 \pm 0.03$ keV, $Y = 0.24 \pm 0.11$ )		0.5	...	$6 \times 10^{-4}$	...

TABLE 3—*Continued*

Object	Best-Fitting Model and Parameters <sup>a</sup>	$\chi_r^2/\text{d.o.f.}$	Observed Flux <sup>b</sup>		Intrinsic Luminosity <sup>c</sup>	
			0.5–2 keV ( $10^{-12}$ erg $\text{cm}^{-2}$ $\text{s}^{-1}$ )	2–10 keV	0.5–2 keV ( $10^{44}$ erg $\text{s}^{-1}$ )	2–10 keV
Centaurus A <sup>§</sup>	Multi-Absorbed P.Law ( $N_{\text{H},1} = 3.2_{-1.0}^{+0.6} \times 10^{23}$ $\text{cm}^{-2}$ , $N_{\text{H},2} = 1.0_{-0.1}^{+0.1} \times 10^{23}$ $\text{cm}^{-2}$ , $N_{\text{H},3} = 7_{-7}^{+3} \times 10^{20}$ $\text{cm}^{-2}$ , $\Gamma = 1.93_{-0.12}^{+0.06}$ )	1.10/1871	...	92.0	...	0.006
	+ P.Law ( $\Gamma \equiv 2.3$ )	...	0.4	...	$4 \times 10^{-6}$	...
	+ Raymond-Smith ( $kT_1 \equiv 0.29$ keV, $Y \equiv 0.4$ )	...	0.3	...	$6 \times 10^{-6}$	...
	+ Raymond-Smith ( $kT_2 \equiv 5.0$ keV, $Y \equiv 0.4$ )	...	0.2	...	$3 \times 10^{-6}$	...
PKS 1333 – 33 <sup>†</sup>	Absorbed P.law ( $N_{\text{H}} = 3.2_{-3.2}^{+0.9} \times 10^{21}$ $\text{cm}^{-2}$ , $\Gamma = 1.51_{-0.20}^{+0.76}$ )	1.07/177	...	0.5	...	0.002
	+ Raymond-Smith ( $kT = 0.86 \pm 0.04$ keV, $Y = 0.21_{-0.12}^{+4.8}$ )	...	0.6	...	0.002	...
NGC 6251	Absorbed P.law ( $N_{\text{H}} = 7.5_{-5.8}^{+6.4} \times 10^{21}$ $\text{cm}^{-2}$ , $\Gamma = 1.83_{-0.18}^{+0.21}$ )	0.97/369	...	1.4	...	0.02
	+ Raymond-Smith ( $kT = 1.04_{-0.18}^{+0.21}$ keV, $Y = 0.06_{-0.04}^{+0.51}$ )	...	0.8	...	0.01	...
3C 353 <sup>†</sup>	Absorbed P.law ( $N_{\text{H}} = 3.7_{-1.5}^{+3.0} \times 10^{22}$ $\text{cm}^{-2}$ , $\Gamma = 1.91_{-0.23}^{+0.39}$ )	1.04/304	...	1.6	...	0.04
	+ Raymond-Smith ( $kT = 1.35_{-0.52}^{+1.67}$ keV, $Y = 0.01_{-0.01}^{+0.05}$ )	...	0.4	...	0.01	...

<sup>a</sup> From the fits to the ASCA data with the best-fit continuum model plus the Fe line (see Table 4). All models include a column density fixed to the Galactic value. The column density reported here is measured in excess of the Galactic column. If the column density is not given, then it was assumed to be equal to the Galactic value, as listed in Table 1.

<sup>b</sup> Flux calculated with the best-fit values of the spectral parameters in column 2.

<sup>c</sup> Intrinsic luminosity (corrected for absorption) in the specified energy range for the corresponding spectral component in column 2.

<sup>d</sup> Only data at energies  $\geq 4$  keV to avoid the contamination of the cooling flow.

<sup>e</sup> Flux and luminosity of the dominant power law ( $\Gamma_1$ ) in the 2–10 keV range.

<sup>f</sup> Tentative detection of the hard tail (see Appendix).

<sup>§</sup> Following Turner et al. (1997b).

<sup>†</sup> Weak-Line Radio Galaxy.



TABLE 4  
GAUSSIAN MODEL PARAMETERS FOR Fe K $\alpha$  EMISSION LINES

Object	$E_{\text{rest}}$ (keV)	$\sigma_{\text{rest}}$ (keV)	$FWHM_{\text{rest}}$ ( $10^3 \text{ km s}^{-1}$ )	$EW_{\text{rest}}^{\text{a}}$ (eV)	$\chi_r^2/\text{d.o.f.}$	$P_{\text{F}}^{\text{b}}$
<i>Broad-Line Radio Galaxies</i>						
3C 111	6.4 <sup>c</sup>	0.50 <sup>c</sup>		105 <sup>+42</sup> <sub>-58</sub>	0.98/1713	$\sim 98\%$
3C 120	6.63 <sup>+0.26</sup> <sub>-0.50</sub>	1.96 <sup>+0.91</sup> <sub>-0.44</sub>	240 <sup>+160</sup> <sub>-70</sub>	1300 <sup>+724</sup> <sub>-397</sub>	0.96/1143	$> 99\%$
Pictor A	6.4 <sup>c</sup>	0.05 <sup>c</sup>		$< 46$	1.02/1501	
3C 215	6.4 <sup>c</sup>	0.05 <sup>c</sup>		$< 100$	0.92/386	
3C 303	6.36 <sup>+0.17</sup> <sub>-0.18</sub>	0.21 <sup>+0.26</sup> <sub>-0.21</sub>	24 <sup>+32</sup> <sub>-24</sub>	489 <sup>+209</sup> <sub>-210</sub>	1.01/366	$> 99\%$
3C 382	6.30 <sup>+0.21</sup> <sub>-0.32</sub>	1.36 <sup>+0.73</sup> <sub>-0.43</sub>	170 <sup>+120</sup> <sub>-60</sub>	758 <sup>+792</sup> <sub>-382</sub>	1.03/981	$> 99\%$
3C 390.3 (1)	6.40 <sup>+0.19</sup> <sub>-0.05</sub>	0.27 <sup>+0.20</sup> <sub>-0.07</sub>	31 <sup>+24</sup> <sub>-9</sub>	256 <sup>+80</sup> <sub>-64</sub>	1.04/1157	$> 99\%$
(2)	6.52 $\pm$ 0.10	0.05 <sup>c</sup>		108 <sup>+60</sup> <sub>-57</sub>	1.02/792	$\geq 98\%$
(3)	6.4 <sup>c</sup>	0.05 <sup>c</sup>		$< 65$	1.03/963	
3C 411	6.4 <sup>c</sup>	0.05 <sup>c</sup>		$< 380$	1.21/59	
3C 445	6.4 <sup>c</sup>	0.15 <sup>+0.15</sup> <sub>-0.12</sub>	17 <sup>+17</sup> <sub>-13</sub>	268 <sup>+272</sup> <sub>-118</sub>	1.05/414	$\geq 98\%$
PKS 2251+11	6.4 <sup>c</sup>	0.05 <sup>c</sup>		$< 315$	1.28/97	
<i>Narrow-Line Radio Galaxies</i>						
PKS 0634 – 205	6.4 <sup>c</sup>	0.05 <sup>c</sup>		$< 400$	1.04/52	
3C 219 (1)	6.4 <sup>c</sup>	0.05 <sup>c</sup>		$< 270$	0.88/188	
(2)	6.4 <sup>c</sup>	0.05 <sup>c</sup>		$< 130$	0.95/291	
3C 313	6.4 <sup>c</sup>	0.05 <sup>c</sup>		$< 600$	0.86/79	
3C 321	6.4 <sup>c</sup>	0.05 <sup>c</sup>		1510 <sup>+950</sup> <sub>-756</sub>	1.41/133	$\geq 95\%$ <sup>d</sup>
3C 346	6.4 <sup>c</sup>	0.05 <sup>c</sup>		$< 570$	0.88/99	
Cygnus A (1)	6.4 <sup>c</sup>	0.05 <sup>c,e</sup>		99 <sup>+78</sup> <sub>-37</sub>	1.03/834	$> 99\%$
(2)	6.4 <sup>c</sup>	0.05 <sup>c,e</sup>		93 <sup>+86</sup> <sub>-27</sub>	1.04/932	$> 99\%$
PKS 2152-69	6.4 <sup>c</sup>	0.05 <sup>c</sup>		$< 250$	0.93/586	
<i>Quasars</i>						
3C 109	6.4 <sup>c</sup>	0.05 <sup>c</sup>		$< 90$	1.04/683	
3C 234	6.4 <sup>c</sup>	0.05 <sup>c</sup>		$< 500$	1.04/53	
3C 249.1	6.4 <sup>c</sup>	0.05 <sup>c</sup>		$< 86$	1.00/341	
3C 254	6.4 <sup>c</sup>	0.05 <sup>c</sup>		$< 87$	1.09/248	
4C +74.26	6.2 <sup>+0.11</sup> <sub>-0.40</sub>	0.59 <sup>+0.47</sup> <sub>-0.20</sub>	69 <sup>+60</sup> <sub>-24</sub>	215 <sup>+297</sup> <sub>-120</sub>	0.93/931	$> 99\%$

TABLE 4—*Continued*

Object	$E_{\text{rest}}$ (keV)	$\sigma_{\text{rest}}$ (keV)	$FWHM_{\text{rest}}$ ( $10^3 \text{ km s}^{-1}$ )	$EW_{\text{rest}}^{\text{a}}$ (eV)	$\chi_r^2/\text{d.o.f.}$	$P_{\text{F}}^{\text{b}}$
<i>Radio Galaxies</i>						
3C 28	6.4 <sup>c</sup>	0.05 <sup>c</sup>		< 160	1.00/688	
PKS 0131 – 36 <sup>†</sup>	6.4 <sup>c</sup>	0.05 <sup>c</sup>		238 <sup>+212</sup> <sub>-165</sub>	1.12/243	> 90%
Fornax A <sup>†</sup>	6.4 <sup>c</sup>	0.05 <sup>c</sup>		< 706	0.91/144	
IC 310 <sup>†</sup>	6.4 <sup>c</sup>	0.05 <sup>c</sup>		< 210	0.98/419	
3C 270 <sup>†</sup>	6.4 <sup>c</sup>	0.05 <sup>c</sup>		255 <sup>+242</sup> <sub>-241</sub>	1.03/424	> 90%
Centaurus A	6.4 <sup>c</sup>	0.05 <sup>c</sup>		140 ± 23	1.10/1871	> 99%
PKS 1333 – 33 <sup>†</sup>	6.4 <sup>c</sup>	0.05 <sup>c</sup>		< 743	1.07/177	
NGC 6251	6.65 <sup>+0.17</sup> <sub>-0.16</sub>	0.05 <sup>c</sup>		443 <sup>+313</sup> <sub>-272</sub>	0.97/369	> 90%
3C 353 <sup>†</sup>	6.4 <sup>c</sup>	0.05 <sup>c</sup>		< 174	1.04/304	

<sup>a</sup> Upper limits on the rest-frame equivalent width correspond to the 90% confidence level.

<sup>b</sup> Significance of fit improvement after adding the line to the model (based on the F-test). This is calculated assuming that there are always three free parameters, even in the cases where two of them are held fixed.

<sup>c</sup> This parameter was held fixed in the fit.

<sup>d</sup> Detection should be regarded with great caution because of the low signal-to-noise.

<sup>e</sup> Marginal improvement is obtained when the line is allowed to be broad; see discussion in the Appendix.

<sup>†</sup> Weak-Line Radio Galaxy.

TABLE 5  
AVERAGE CONTINUUM MODEL PARAMETERS BY CLASS

Class	Number of Objects	Simple Averages <sup>a</sup>						Weighted Mean <sup>b</sup>
		$\langle \Gamma \rangle$	$\sigma_{\Gamma}$	$\langle \log L_{2-10 \text{ keV}} \rangle$ (erg s <sup>-1</sup> )	$\sigma_{\log L}$ (erg s <sup>-1</sup> )	$\log \langle (N_{\text{H}} - N_{\text{H,Gal}}) \rangle$ (cm <sup>-2</sup> )	$\log \langle \sigma_{\Delta N_{\text{H}}} \rangle$ (cm <sup>-2</sup> )	$\bar{\Gamma}$
BLRGs	9	1.64	0.29	44.17	0.37	22.37	22.87	1.78 ± 0.01
	8					20.88 <sup>c</sup>	21.21 <sup>c</sup>	
QSRs	5	1.80	0.15	44.67	0.50	22.69	23.03	1.75 ± 0.03
	4					21.10 <sup>d</sup>	21.18 <sup>d</sup>	
NLRGs	9	1.77	0.13	43.68	0.67	23.30	23.55	1.80 ± 0.05
RGs	6	1.62	0.31	41.76	0.77	23.02	23.30	1.81 ± 0.07
WLRG	4	1.49	0.30	41.65	0.89	23.00	23.35	1.47 ± 0.16
Other RGs	2	1.88	0.07	42.04	0.37	23.04	23.26	1.89 ± 0.08
Sy 1s	7	1.88	0.14	43.66	0.24	...	...	1.87 ± 0.02
QSOs	7	1.86	0.20	45.08	0.55	...	...	1.78 ± 0.01
Sy 2s	13	1.91	0.88	42.58	0.53	...	...	2.17 ± 0.03
LINERs	4	1.88	0.09	41.09	0.26	...	...	1.88 ± 0.05

<sup>a</sup>  $\sigma$  denotes the dispersion in a particular quantity:  $\sigma_x^2 = \langle x^2 \rangle - \langle x \rangle^2$ .

<sup>b</sup> The weighted mean is computed by weighing each sample by its inverse square error bar. The quoted final uncertainty is the error in the mean.

<sup>c</sup> Without 3C 445 (see text).

<sup>d</sup> Without 3C 234 (see text).

TABLE 6  
RESULTS OF CORRELATION ANALYSIS

Objects in Sample	$L_1$ <sup>a</sup>	$L_1$ Upper Limits	$L_2$ <sup>b</sup>	$L_2$ Upper Limits	$\tau_{12}$ <sup>c</sup>	$P_\tau$ <sup>d</sup>	$L_3$ <sup>e</sup>	$L_3$ Upper Limits	$\tau_{12,3}$ <sup>f</sup>	$\sigma$ <sup>g</sup>	$P_{12,3}$ <sup>h</sup>
27	$L_{2-10 \text{ keV}}$	0	$L_{[\text{O III}]}$	3	0.586	$< 10^{-4}$	$L_{5 \text{ GHz, core}}$	2	0.442	0.133	$1.0 \times 10^{-3}$
25	$L_{2-10 \text{ keV}}$	0	$L_{[\text{O III}]}$	3			$L_{5 \text{ GHz, lobe}}$	0	0.449	0.135	$8 \times 10^{-4}$
20	$L_{2-10 \text{ keV}}$	0	$L_{[\text{O III}]}$	2			$L_{12 \mu\text{m}}$	11	0.504	0.119	$< 4 \times 10^{-4}$
24	$L_{2-10 \text{ keV}}$	0	$L_{5 \text{ GHz, lobe}}$	0	0.509	$5 \times 10^{-3}$	$L_{[\text{O III}]}$	3	0.344	0.154	0.026
20	$L_{2-10 \text{ keV}}$	0	$L_{5 \text{ GHz, lobe}}$	0			$L_{12 \mu\text{m}}$	10	0.404	0.107	$< 2 \times 10^{-4}$
21	$L_{2-10 \text{ keV}}$	0	$L_{12 \mu\text{m}}$	11	0.608	$1 \times 10^{-4}$	$L_{[\text{O III}]}$	3	0.229	0.068	$8 \times 10^{-4}$
20	$L_{2-10 \text{ keV}}$	0	$L_{12 \mu\text{m}}$	10			$L_{5 \text{ GHz, lobe}}$	0	0.308	0.090	$6 \times 10^{-4}$
27	$L_{2-10 \text{ keV}}$	0	$L_{5 \text{ GHz, core}}$	3	0.563	$1 \times 10^{-4}$	$L_{[\text{O III}]}$	5	0.265	0.148	0.073
24	$L_{2-10 \text{ keV}}$	0	$L_{60 \mu\text{m}}$	11	0.409	$5 \times 10^{-3}$	$L_{[\text{O III}]}$	3	0.151	0.078	0.052

<sup>a</sup> Independent variable (luminosity).

<sup>b</sup> Dependent variable (luminosity).

<sup>c</sup> Kendall correlation coefficient.

<sup>d</sup> Probability of chance correlation from Kendall test (small probabilities indicate significant correlations).

<sup>e</sup> Third luminosity that is correlated with both  $L_1$  and  $L_2$ .

<sup>f</sup> Kendall *partial* correlation coefficient (see description in text).

<sup>g</sup> Square root of the variance associated with  $\tau_{12,3}$  (see text for details).

<sup>h</sup> Probability of spurious correlation from Kendall *partial* correlation test (small probabilities indicate significant correlations).

TABLE 7  
INTRINSIC EXCESS ABSORPTION OF BLRGs AND QSRs<sup>a</sup>

Object	$N_{\text{H,intr}}$ ( $\text{cm}^{-2}$ )	$L_{2-10 \text{ keV}}$ ( $\text{erg s}^{-1}$ )
<i>Broad-Line Radio Galaxies</i>		
3C 303	$1.5^{+0.6}_{-0.5} \times 10^{21}$	$8.4 \times 10^{43}$
3C 390.3 (1)	$3.7^{+2.0}_{-2.0} \times 10^{20}$	$1.0 \times 10^{44}$
(2)	$1.4^{+0.3}_{-0.3} \times 10^{21}$	$1.2 \times 10^{44}$
(3)	$7.2^{+1.0}_{-1.0} \times 10^{20}$	$1.9 \times 10^{44}$
3C 445	$3.0^{+8.0}_{-1.3} \times 10^{23}$	$8.0 \times 10^{43}$
PKS 2251+11	$1.2^{+0.5}_{-0.5} \times 10^{22}$	$3.0 \times 10^{44}$
<i>Quasars</i>		
3C 109	$6.8^{+0.8}_{-0.8} \times 10^{21}$	$1.1 \times 10^{45}$
3C 234	$3.8^{+4.0}_{-1.2} \times 10^{23}$	$8.0 \times 10^{43}$
4C +74.26	$2.5^{+0.3}_{-0.3} \times 10^{21}$	$4.0 \times 10^{44}$

<sup>a</sup> From a fit to the *ASCA* data with the best-fit continuum model in Table 3 where the absorption includes a local ( $z=0$ ) absorber fixed to Galactic plus a cold absorber at the source redshift ( $z_{\text{abs}} = z_{\text{source}}$ ), free to vary in the fit. The latter is the quantity reported,  $N_{\text{H,intr}}$ .

**Figure 1** is separate, in the form of 5 TIFF files. It can also be obtained in postscript form along with the complete preprint from

[http://www.astro.psu.edu/users/mce/preprint\\_index.html](http://www.astro.psu.edu/users/mce/preprint_index.html).

**Figure 1.** – Results of spectral fits to the 0.6–10 keV *ASCA* continuum of radio-loud AGN. For each source, we show the best-fitting continuum model (*top panels*) and the corresponding residuals (*bottom panels*). In the cases where an Fe line was required between 6 and 7 keV, the line profile model was excluded from the model plotted in Figure 1 to make the line appear in the ratio spectrum. The best-fit models are reported in Tables 3 and 4, with the continuum parameters in Table 3 and the Fe  $K\alpha$  parameters in Table 4. Only the SIS0 and SIS1 data are plotted here for clarity, although the model was fitted to the data from all four detectors jointly.

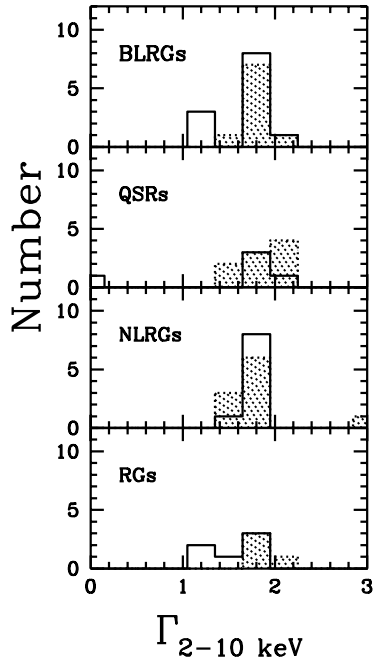


**Figure 2a** – Distribution of the 2–10 keV intrinsic photon indices for the various subclasses of radio-loud AGN (*solid lines*). The distribution spans a similar range in all subclasses with a mean  $\langle \Gamma \rangle \sim 1.7 - 1.8$ . Superposed on the distribution for each subclass is the distribution in the corresponding subclass of radio-quiet AGN (Seyfert 1s, Seyfert 2s, QSOs, and LINERs) in matching ranges of intrinsic 2–10 keV luminosities (*dotted areas*). The distributions in Seyfert 1s and BLRGs differ at the 94% confidence level (based on the Kolmogorov-Smirnov test). Their mean values,  $\langle \Gamma_{\text{BLRG}} \rangle = 1.6$  and  $\langle \Gamma_{\text{Sy1}} \rangle = 1.9$ , differ at the 93% level (based on the t-test). The other classes of radio-loud and radio-quiet AGN are not demonstrably different according to the KS test.

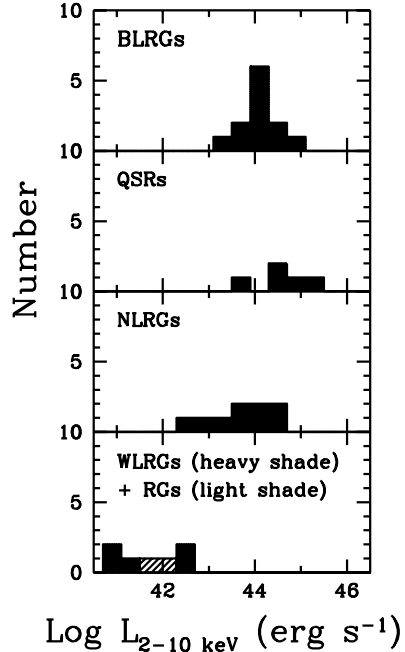


**Figure 2b** – Distribution of the intrinsic (absorption-corrected) 2–10 keV luminosity of the nuclear power-law component in the various subclasses of radio-loud AGN. BLRGs, QSRs, and NLRGs largely overlap, with QSRs populating the highest luminosities and NLRGs the lowest. RGs and WLRGs are found at luminosities lower than  $10^{42} \text{ erg s}^{-1}$ , significantly fainter than the other subclasses. This is at odds with the predictions of simple orientation-based unification schemes.

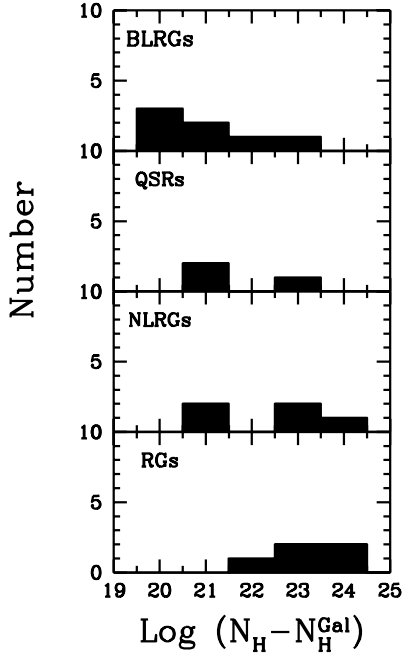


**Figure 2c** – Histogram of the excess X-ray column density for the various subclasses of radio-loud AGN from Table 3 (compensated for the systematic overestimation by the SIS detector at low energies). Only sources where excess column densities were detected with *ASCA* are plotted. In NLRGs and RGs the obscuring columns are around  $10^{21}$ – $10^{24}$   $\text{cm}^{-2}$ . Excess X-ray absorption with similar columns is also present in a fraction of BLRGs and QSRs.

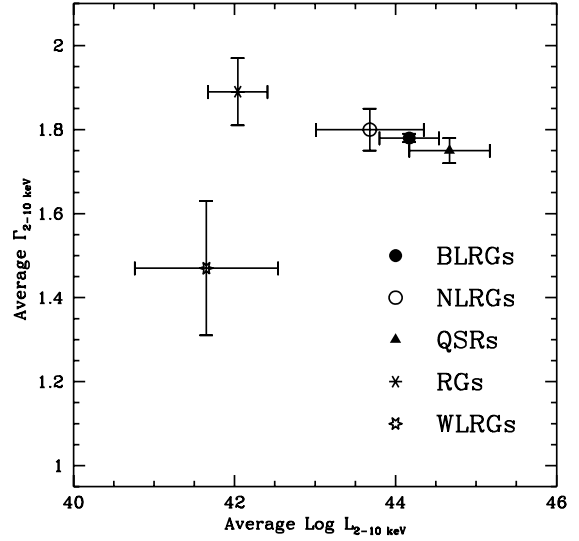


**Figure 2d** – Plot of the average 2–10 keV photon index (the weighted average in Table 5) versus the average intrinsic 2–10 keV luminosity for the various classes of radio sources. There is an apparent trend of flatter slopes with increasing luminosity going from RGs to QSRs, although a Kendall non-parametric correlation test gives only a probability of  $\sim 95\%$  that a correlation is present. WLRGs stick out for having lower luminosities and flatter slopes than the remaining sources.



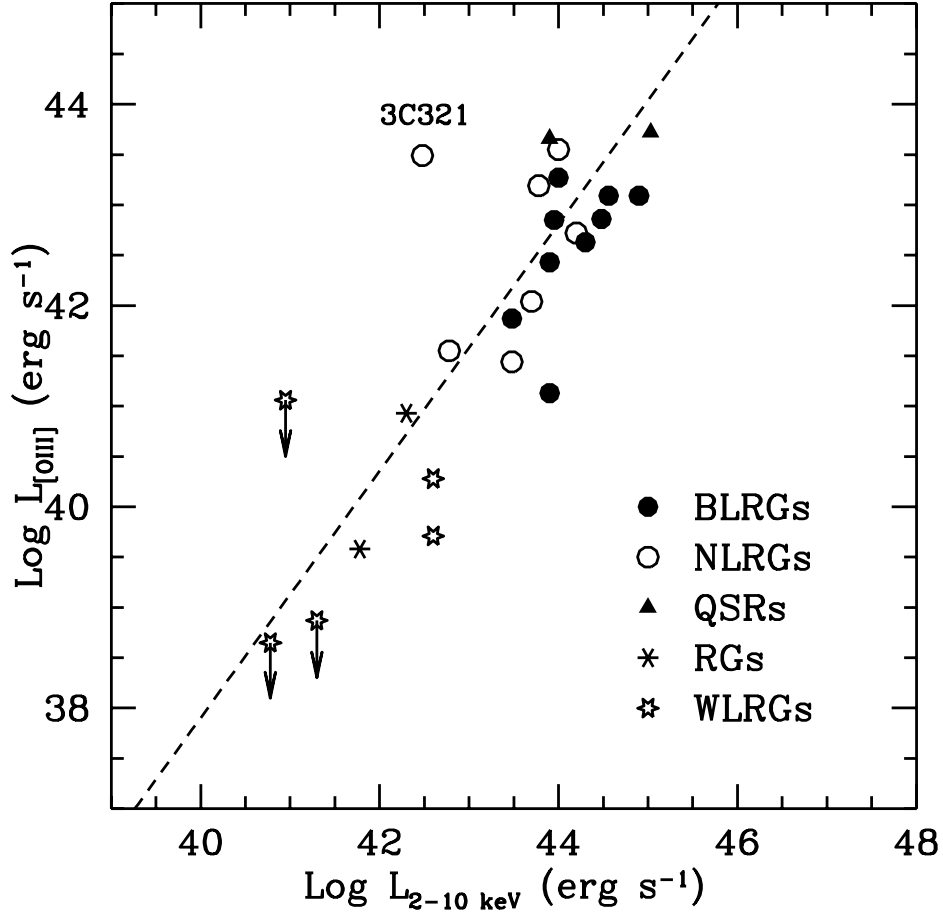


**Figure 3a** – Correlation between the rest-frame luminosity of the [O III] emission lines, corrected for Galactic extinction, and the intrinsic 2–10 keV power-law luminosity for the various subclasses of radio-loud AGN. The correlation holds over more than four decades in X-ray luminosity. The outlier at higher [O III] luminosities is 3C 321, where a contribution from a starburst could be present. Excluding this source, the upper limits, and WLRGs, the linear regression analysis yields  $\log L_{[\text{OIII}]} = 1.23 \log L_{2-10 \text{ keV}} - 11.14$  for the sample of BLRGs, QSRs, NLRGs, and RGs (dotted line). Note that WLRGs have abnormally low  $L_{[\text{OIII}]}$  for their X-ray luminosity, which is one of their defining properties.

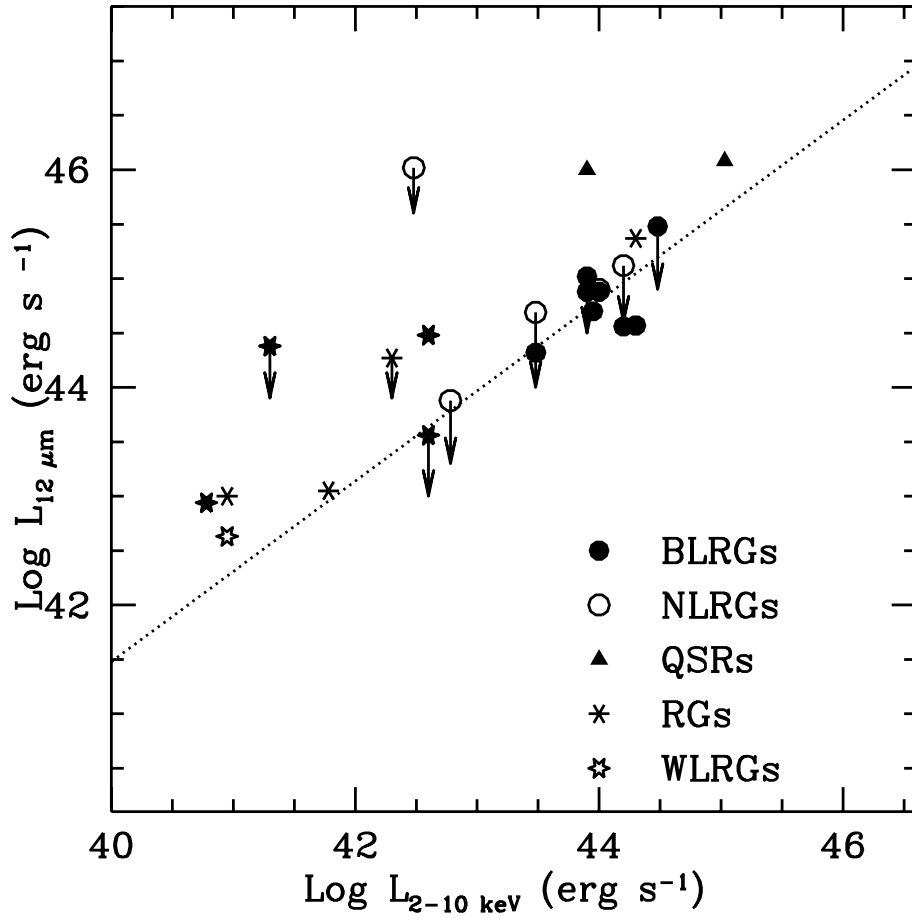


**Figure 3b** – Correlation between the FIR emission at  $12 \mu\text{m}$  and the intrinsic 2–10 keV power-law luminosity. Excluding the upper limits and WLRGs, a linear regression analysis gives  $\log L_{12 \mu\text{m}} = 0.83 \log L_{2-10 \text{ keV}} + 8.28$  for the sample of BLRGs, QSRs, NLRGs, and RGs (dotted line).

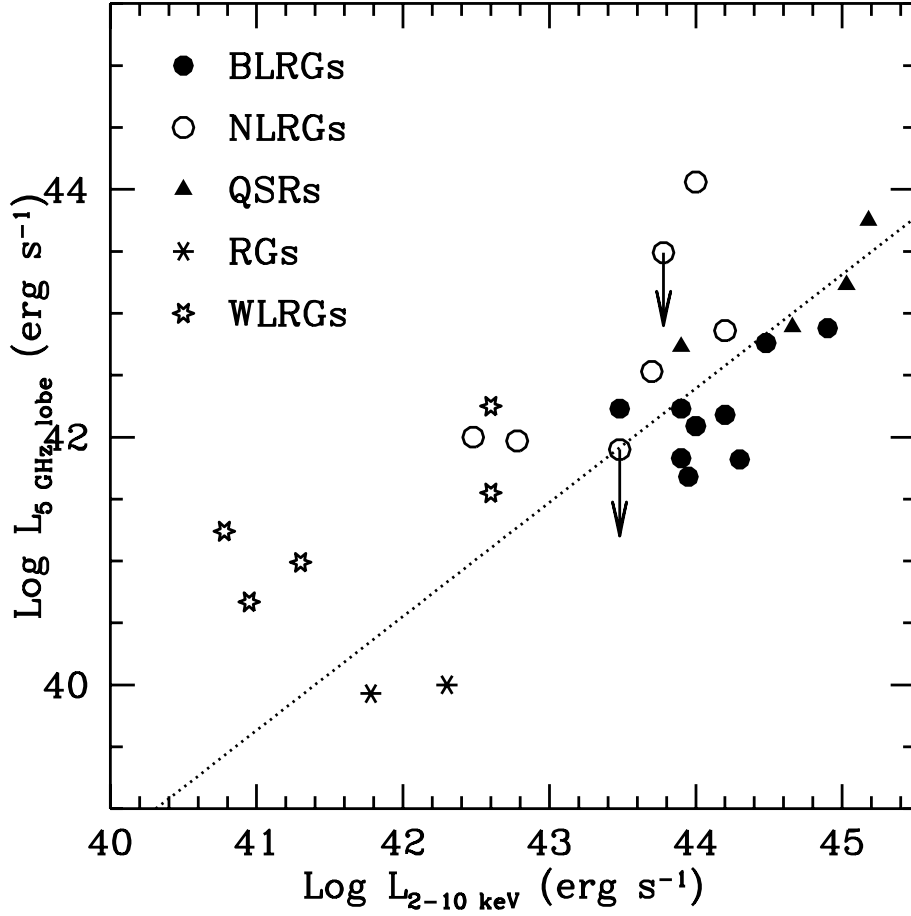


**Figure 3c** – Correlation between the lobe radio power at 5 GHz and the intrinsic 2–10 keV power-law luminosity. Excluding the upper limits and WLRGs, a linear regression analysis gives  $\log L_{\text{lobe}} = 0.92 \log L_{2-10 \text{ keV}} + 1.91$  for the sample of BLRGs, QSRs, NLRGs, and RGs (dotted line). WLRGs have powerful radio lobe emission, consistent with their defining properties.

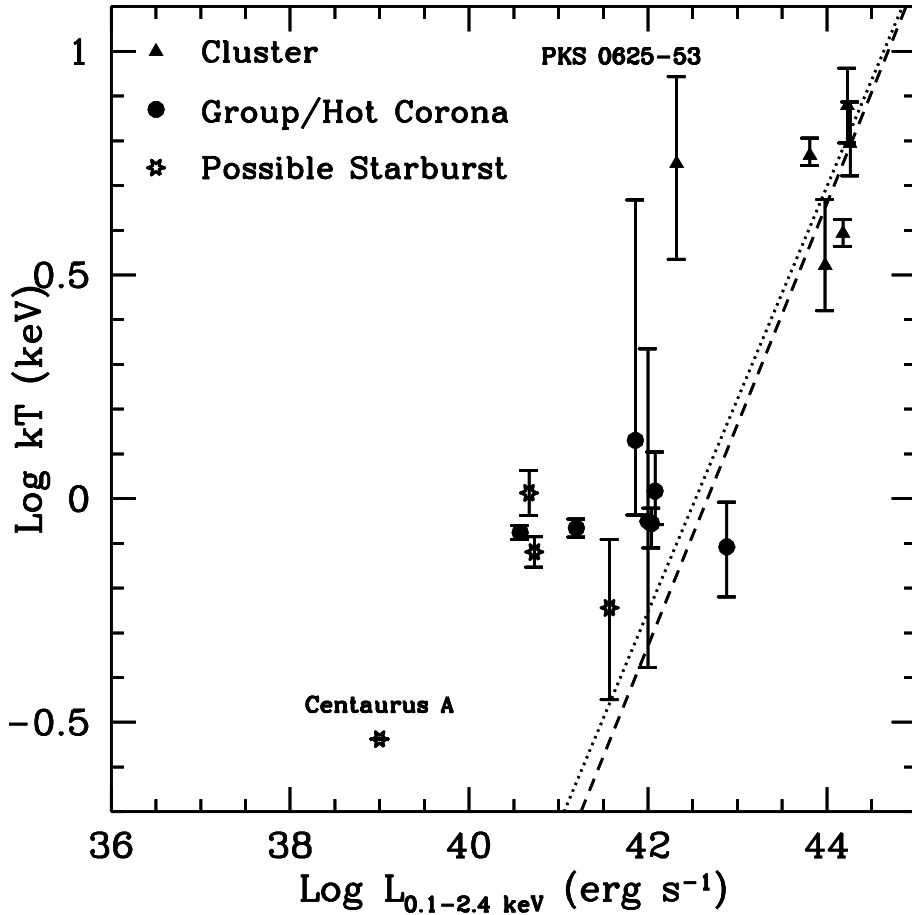


**Figure 4** – Plot of the temperature versus the intrinsic 0.1–2.4 keV luminosity of the soft thermal component detected with *ASCA* in several NLRGs, RGs, and WLRGs from our sample. A bimodal distribution is apparent, with several sources grouped in the region of high  $kT$  and  $L_{0.1-2.4 \text{ keV}}$ , typical of clusters of galaxies (*filled triangles*), and others having lower  $kT$  and luminosities reminiscent of poor groups and/or hot coronae of isolated giant ellipticals (*filled circles*). The sources 3C 321, 3C 234, Centaurus A, and PKS 0131–36, where the thermal component could have a starburst or nuclear origin, are plotted with different symbols (*stars*). The solid and dotted lines represent the best-fitting linear-regression lines to the  $kT - L_x$  relationship of normal clusters, both with and without cooling flows (from Markevitch 1998). The clusters hosting radio galaxies (*upper right corner*) appear to have properties similar to normal clusters.

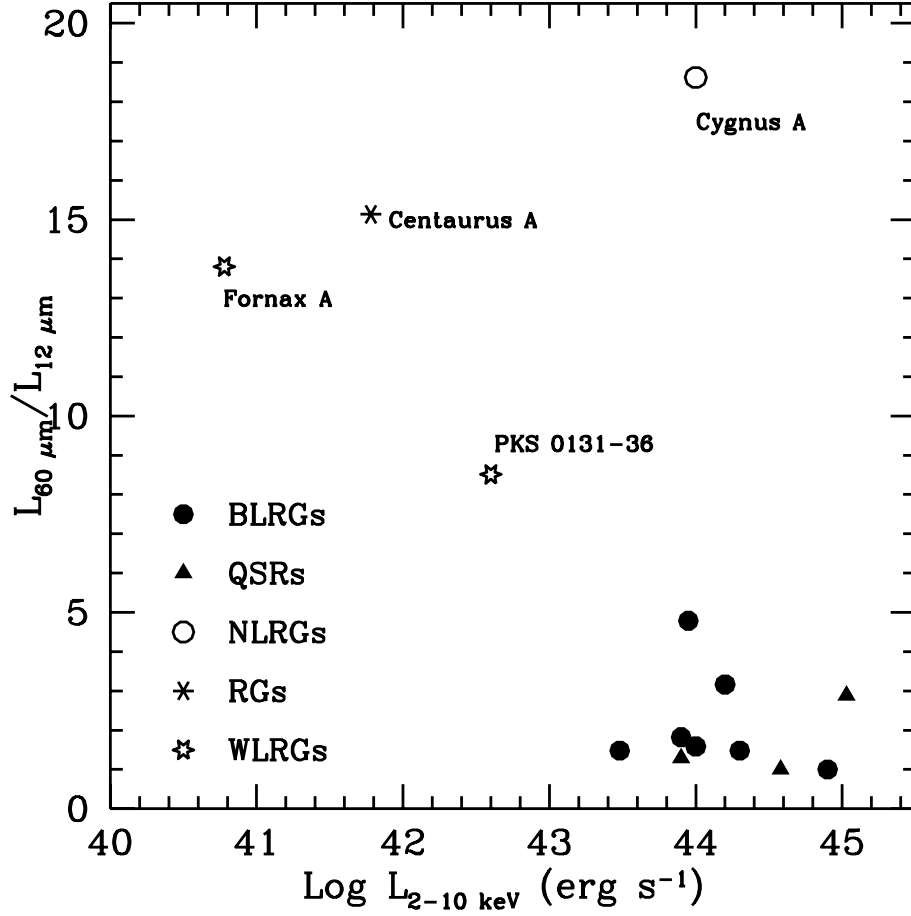


**Figure 5** – Plot of the 60-to-12  $\mu\text{m}$  FIR flux ratio versus the intrinsic 2–10 keV power-law luminosity for the sources in Table 1 with firm detections at all three wavelengths. Most BLRGs and QSRs have ratios consistent with a non-thermal FIR emission, while Centaurus A, Fornax A, and PKS 0131–36 have larger 60-to-12  $\mu\text{m}$  flux ratios, possibly related to an additional contribution from a starburst.

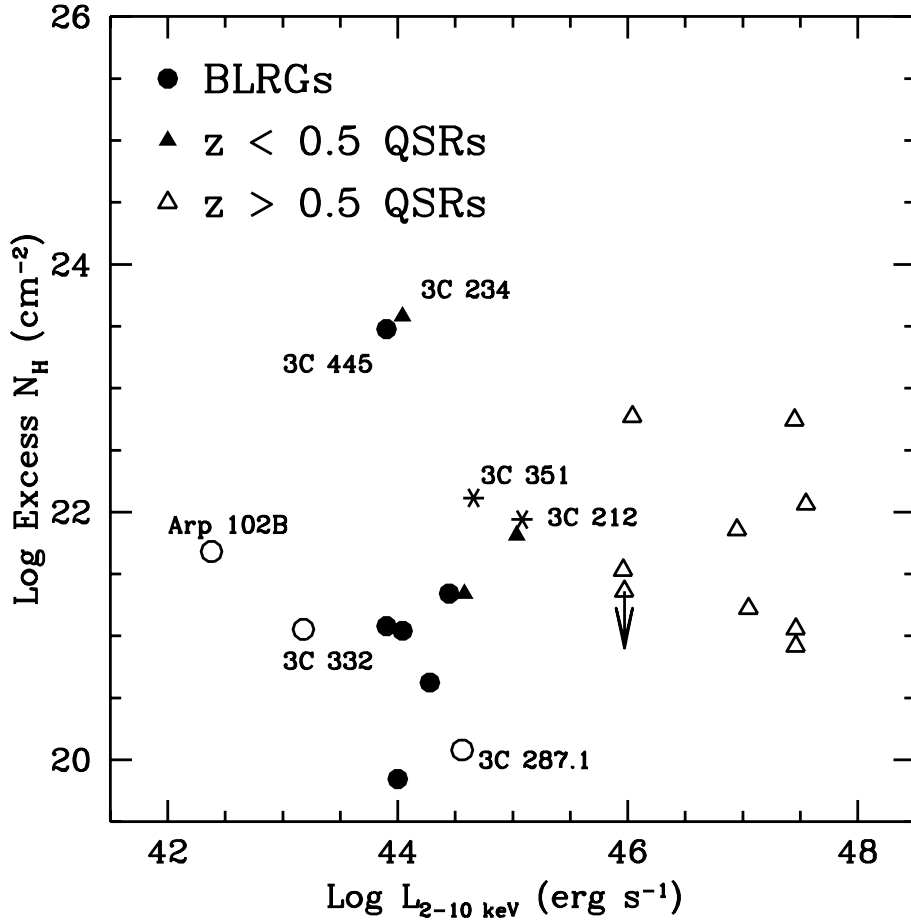


**Figure 6** – Plot of the intrinsic X-ray absorption column density versus intrinsic (absorption-corrected) nuclear X-ray luminosity for radio-loud AGN. The filled circles and triangles are the BLRGs and QSRs of the present study (data from Table 7). The open triangles are the high- $z$  radio-loud QSRs studied by Cappi et al. (1997) and Elvis et al. (1994) with *ROSAT* and *ASCA*. Also plotted are the QSRs 3C 351 and 3C 212, where detailed modelling of the *ROSAT* data indicates a highly-ionized absorber (Fiore et al. 1993; Mathur 1994). The open circles are the BLRGs Arp 102B, 3C 332, and 3C 287.1, where excess X-ray columns were measured with *ROSAT* (Crawford & Fabian 1995; Halpern 1997). Uncertainties on the fitted  $N_{\text{H}}$  are omitted for clarity of presentation; however, they are generally large ( $\sim 60\%$ ), especially for Arp 102B (80%), 3C 332 (70%), and 3C 287.1 (41%), due to the low signal-to-noise ratios of the *ROSAT* spectra. Radio-loud AGN exhibit large X-ray column densities over a wide range of X-ray nuclear luminosities; a large dispersion of columns is observed at lower luminosities, with 3C 445 and 3C 234 having the largest column densities.

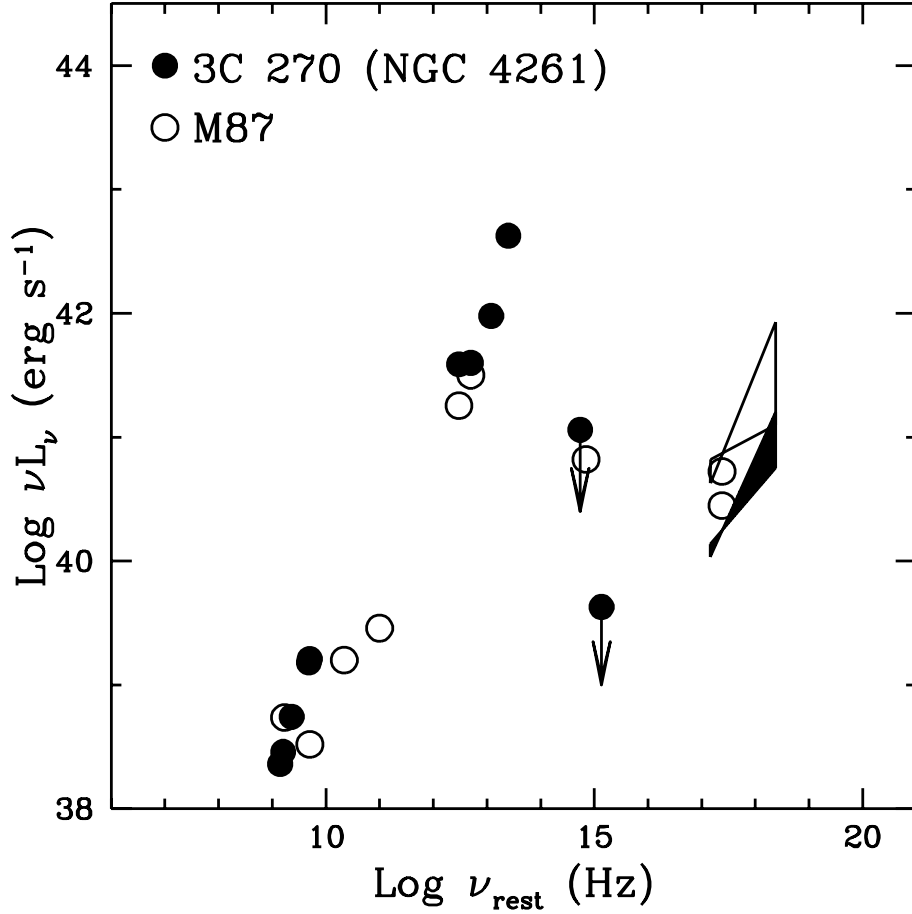


**Figure 7** – Spectral energy distribution of the nuclear emission of 3C 270 (hosted by the giant elliptical NGC 4261) from radio to X-rays (using data in Table 1, the *ASCA* data presented here, optical nuclear fluxes from Ferrarese et al. 1996, and the UV upper limit from Zirbel & Baum 1998). Also plotted for comparison is the spectral energy distribution of M87 (Reynolds et al. 1996; Allen et al. 1999), where an advection-dominated accretion flow (ADAF) is thought to be present. The data of 3C 270 imply a ratio of the total bolometric luminosity to the Eddington luminosity of  $L_{\text{Bol}}/L_{\text{Edd}} \lesssim 4 \times 10^{-4}$ , placing 3C 270 in the ADAF regime. Note the lack of a strong UV bump in 3C 270, which is typical of other low-power radio galaxies as well, and could explain the weak [O III] emission in these sources.

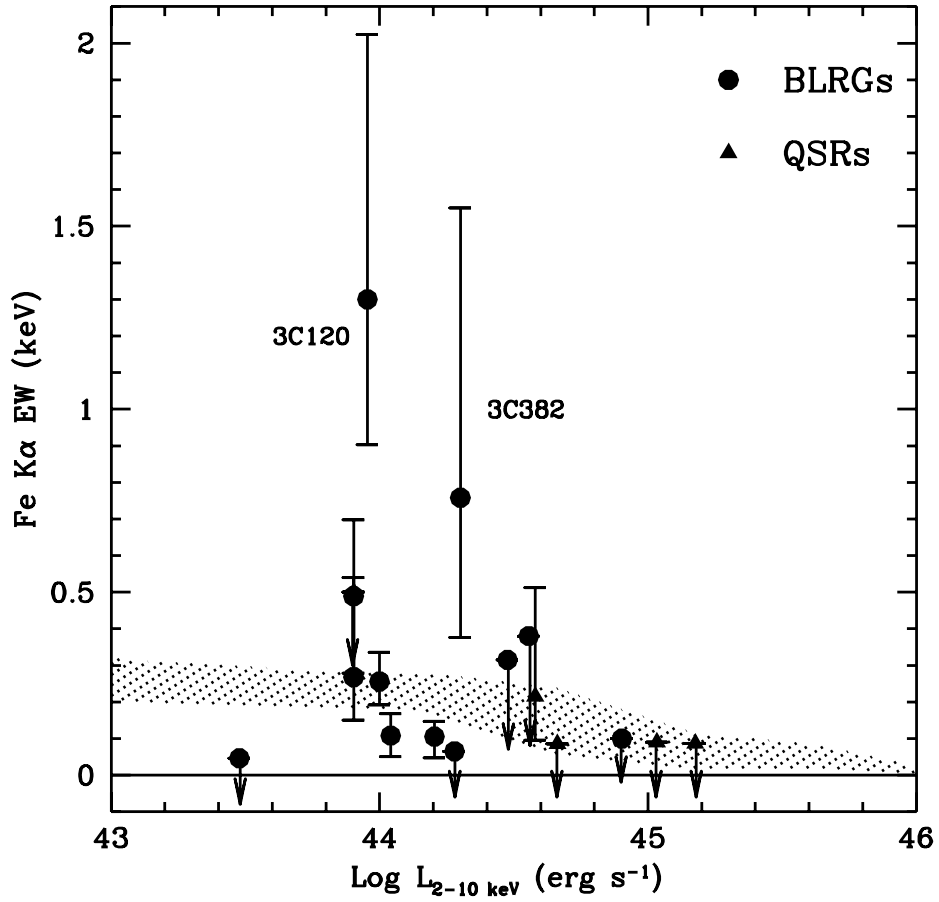


**Figure 8** – Plot of the intrinsic EW of the Fe K $\alpha$  line (or upper limit at 90% confidence) versus the absorption-corrected power law X-ray luminosity for the sub-classes of BLRGs and QSRs of our sample (updated from Eracleous & Halpern 1998). The shaded strip represents the X-ray Baldwin effect at  $1\sigma$  for radio-quiet sources (Nandra et al. 1997c). Radio-loud AGN have a larger dispersion of intrinsic EW for a given X-ray luminosity than radio-quiet sources.